Experimental and Theoretical Studies of Friction and Adhesion of Elastomeric Materials

Ahmad Rezaei Mojdehi

Dissertation submitted to the faculty of the Virginia Polytechnic Institute and State University in partial fulfillment of the requirements for the degree of

Doctor of Philosophy

In

Engineering Mechanics

David A. Dillard, Co-Chair

Douglas P. Holmes, Co-Chair

Timothy E. Long

Christopher B. Williams

Jonathan B. Boreyko

September 7, 2017

Blacksburg, VA

Keywords: Friction, Adhesion, Elastomeric Materials, Shear Lag Model, Pressure Sensitive Adhesives, Fracture Mechanics

Experimental and Theoretical Studies of Friction and Adhesion of Elastomeric Materials

Ahmad Rezaei Mojdehi

ABSTRACT

In this dissertation, four distinct but in some ways related topics, mostly related to experimental and theoretical investigations of friction and adhesion of elastomeric materials, are presented. First, an experimental and theoretical study of the interaction between elastic beams and granular media under compressive loading is performed. Buckling loads of beams with different dimensions and boundary conditions within granular media of different depths and grain sizes are measured, and theoretically approximated using the Ritz energy approach, based on the concept of beam on an elastic foundation. Several nondimensional parameters and a scaling law are derived to characterize different interaction regimes between the beams and granular support. The findings from this work is believed to be helpful for improved understanding of interactions between elastic beams and surrounding elastic foundation with applications to piles, oil pipelines, and robotic needle insertion into soft tissues. Second, the role of axial compliance on the friction of extensible strips is investigated. Significant changes were observed in the static and kinetic friction of strips, when the effective axial compliance was changed. The underlying causes of the changes in the frictional response are explained and quantitatively predicted using an extended shear lag model. We believe that this study provides insights into the effect of axial compliance on the frictional response of materials, paving the way for design and optimization of systems where the static and kinetic friction forces play an important role. Third, the effect of normal force and rate on the kinetic friction of two different elastomers, namely acrylic and silicone-based elastomers is evaluated. A custom-built pendulum test setup was used to perform the friction test in dynamic conditions. Two substantially different responses with respect to the change in normal force were observed and the role of different contributions to the frictional response of viscoelastic materials, *i.e.* bulk hysteresis friction, adhesion friction, and cohesion friction, are discussed. Different scenarios such as modifying the surface by using graphite powder, reducing test velocity, and also performing drop tests to characterize the surface hysteresis of the elastomers, were considered to further explore the origin of frictional responses of the elastomers. This study could improve insights gained from Dynamic Mechanical Analysis (DMA) data when obtaining and interpreting the effect of normal force on kinetic COF of elastomers with potential applications to

tires, shoes, etc. where friction plays an important role. Last, a generalized scaling law, based on the classical fracture mechanics approach, is developed to predict the bond strength of adhesive systems. The proposed scaling law, which depends on the rate of change of bond area with compliance, is in apparent discrepancy with the previously reported scaling relationship that depends on the ratio of area to compliance. This distinction can have a profound impact on the expected bond strength of systems, particularly when failure mechanism changes or the compliance of the load train is increased. Furthermore, the shear lag model is implemented to derive a closed-form relation for the system compliance and the conditions where the two models deviate from each other are discussed and demonstrated. The results obtained from this approach could lead to a better understanding of the relationship between the bond strength and the geometry and mechanical properties of adhesive systems, with applications to different types of adhesive joints such as bio-inspired adhesive, biomedical adhesive tapes, and structural adhesive joints.

Experimental and Theoretical Studies of Friction and Adhesion of Elastomeric Materials

Ahmad Rezaei Mojdehi

GENERAL AUDIENCE ABSTRACT

In this dissertation, four distinct but in some ways related topics, mostly related to experimental and theoretical investigations of friction and adhesion of elastomeric materials, are presented. The theoretical models are based on classic solutions for load transfer between two members through shearing an adhesive layer or frictional interface on extensible support layers. First, an experimental and theoretical study of buckling of elastic columns embedded in granular media is performed. In many engineering applications, it is desirable to insert and manipulate an elastic column like needle or drill rod within complex media, such as soft tissues or granular beds like sand and gravel. In these procedures the column is subjected to axial loading and it tends to buckle and lose stability due to a high length to thickness ratio. Burrowing a flexible structure through fragile media requires understanding the coupled interactions between a geometrically non-linear structure and its reconfigurable surroundings. Several nondimensional parameters and a scaling law are derived to characterize different interaction regimes between the columns and granular support in order to better understand the stability of elastic structures confined in a granular bed. Second, a comprehensive study that combines theory and experiments to investigate frictional responses of a system, i.e. static and kinetic friction, with change in system stiffness is presented. Friction plays an important role in many technologies such as tires, brakes, rubber seals, conveyer belts, and footwear. Understanding the role of system stiffness on the frictional properties of materials, from both experimental and theoretical points of view, has important implications for such technologies. Significant changes were observed in the static and kinetic friction of strips when the effective axial stiffness was changed. The underlying causes of the changes in the frictional response are explained and quantitatively predicted by a theoretical model. Furthermore, a permanent increase in kinetic friction of sufficiently soft extensible strip was found, with potential application to improved friction performance of materials where the kinetic friction plays a major role. Third, the effect of normal force and rate on the kinetic friction of two different elastomers, namely acrylic and silicone-based elastomers, is evaluated. A custom-built pendulum test setup was used to perform the friction test in dynamic conditions. Two substantially different responses with respect to the change in normal force were observed and the role of different frictional mechanisms is discussed. This study could improve insights gained from mechanical testing data

at different temperatures and speed when obtaining and interpreting the effect of normal force on kinetic COF of elastomers, with potential applications to tires, shoes, etc., where friction plays an important role. Last, a theoretical model, to predict the bond strength of adhesive systems, is developed. The proposed model, which depends on the rate of change of bond area with compliance, is in apparent discrepancy with the previously reported scaling relationship thatdepends on the ratio of area to compliance. This distinction can have a profound impact on the expected bond strength of systems, particularly when failure mechanism changes or the compliance of the load train is increased. The conditions where the two models deviate from each other are discussed and demonstrated. The developed model could help to better understand the role of system compliance on the bond strength of adhesive systems such as bio-inspired adhesive, biomedical adhesive, and structural adhesive, where the system stiffness changes significantly depending on the applications.

Dedicated to my wife Maryam and my children Meraj and Miad

Acknowledgements

I would like to express my sincere appreciation to my advisors, Dr. David A. Dillard and Dr. Douglas P. Holmes, for their valuable time, guidance, and support through my journey as a Ph.D. student at Virginia Tech. Without their advice, untiring help, and constructive criticism the completion of this journey would not have been possible. I want to thank Dr. Holmes for kindly introducing me to Dr. Dillard before leaving Virginia Tech, and thank Dr. Dillard for introducing me to the new world of polymers and giving me an opportunity to work in this field.

I would also like to thank my Ph.D. committee members Dr. Timothy E. Long, Dr. Christopher B. Williams, and Dr. Jonathan B. Boreyko for their insightful suggestions toward improving my research.

I am greatly thankful to the Department of Biomedical Engineering and Mechanics (BEAM) and Provost's Office and College of Engineering at Virginia Tech for supporting me during this journey, and the Macromolecules Innovation Institute (MII) at Virginia Tech for fostering interdisciplinary research in polymer and adhesion science. Special thanks to MII for supporting me to attend the Adhesion Society conferences, helping me to develop my technical communication skills as well as interacting with scientists in the adhesion science area.

I want to thank Mac McCord, Danny Reed, and Darrel Link for their help and guidance in using the department's equipment.

I would like to express my gratitude to my wife Maryam for the love and support over the past eight years, and thank my children Meraj and Miad for being patient while daddy was working to successfully accomplish this journey. I owe Maryam, Meraj and Miad an apology for the time I should have spent with them as family, but had to work far too often and too long. Lastly, I want to thank my parents for sending their love, and prayers thousands of miles away from home.

Table of contents

List of figures

List of tables

1 Introduction

This dissertation is prepared in manuscript-format, including four papers (two published, one in review, and one under preparation to be submitted in a peer-reviewed journal), appeared here as chapters II-V. The title of chapters/papers are: chapter II: Buckling of elastic beams embedded in granular media (published in the *Extreme Mechanics Letters*), chapter III: Friction of extensible strips: An extended shear lag model with experimental evaluation (published in *International Journal of Solids and Structures*), chapter IV: The effect of normal force and rate on kinetic coefficient of friction of elastomeric materials (under preparation), and chapter V: Revisiting the generalized scaling law for adhesion: role of compliance and extension to progressive failure (published in *Soft Matter*). Since the dissertation represents several distinct but in some ways related topics, the motivation and summary of each work will be presented separately in the introduction while each chapter will have its own introduction with detailed literature review.

Chapter II: Buckling of elastic beams embedded in granular media

- Mojdehi, Ahmad R., Behrouz Tavakol, Wesley Royston, David A. Dillard, and Douglas P. Holmes. "Buckling of elastic beams embedded in granular media." *Extreme Mechanics Letters* 9 (2016): 237-244.
- Top 5 most downloaded articles, *Extreme Mechanics Letters*, 2016

Slender rods and beams, commonly referred to as *elastica*, can be used to describe carbon nanotubes, fiber optic cables, spider silk, human hair, offshore piles, and well drilling tools. In many engineering applications, it is desirable to insert and manipulate an elastic beam within complex media, such as soft tissues or granular beds. For example, exploratory drilling in the depth of the earth may involve a drill rod interacting with a mixture of soil, rock, water, and oil. Moreover, needle insertion is an essential part of many clinical treatments and surgeries. The purpose of most of these applications is to reach a specific target by controlling the beam's tip path. This target can be a cancerous tumor in the brain or an oil field in the desert. In these procedures the beam is subjected to axial loading and it tends to buckle and lose stability due to a high slenderness ratio. Burrowing a flexible structure through fragile media requires understanding the coupled interactions between a geometrically non-linear structure and its reconfigurable surroundings. In the second chapter, an experimental and theoretical study of the buckling response of slender elastic beams within granular media is performed. Buckling loads of beams with

different flexural rigidity, length, and boundary conditions within granular media of different depths were determined. Simply supported and clamped boundary conditions were used at the embedded end of the beams. The stiffness of the effective support along the depth of the beam is found to vary linearly. The overburden mass of the top grains on the lower grains could result in an increase in the normal force and therefore an increase in internal friction forces between grains, leading to effectively increasing the stiffness of the media along the depth. The Ritz approximate method is implemented to model the buckling response of the beams based on the concept of an overhanging beam on elastic foundation, using a series of springs whose spring constants change linearly with respect to the depth of the grains. We found a good agreement between the experimental results and the theoretical model. There is a characteristic penetration ratio where the beams are not able to sense the boundary condition at the embedded end, resulting in a convergence of the buckling loads. This condition happens when the rigidity of the beam is lower than the effective stiffness of granular support, leading to the confinement of the lower portion of the beam inside the grains, and acting as a secondary boundary condition that is independent of the condition at the end of the beam. We derive a scaling law to characterize this characteristic penetration ratio in terms of a dimensionless stiffness parameter, allowing for the characterization of three distinct interactions between the beam and medium based on the ratio of effective stiffness of the granular support to the beam's effective stiffness. The findings from this work is believed to be helpful for better understanding of interactions between elastic beams and surrounding elastic foundation with applications to piles, oil pipelines, and robotic needle insertion into soft tissues.

Chapter III: Friction of extensible strips: An extended shear lag model with experimental evaluation

- Mojdehi, Ahmad R., Douglas P. Holmes, and David A. Dillard. "Friction of extensible strips: An extended shear lag model with experimental evaluation." *International Journal of Solids and Structures* 124 (2017): 125-134.

Friction is ubiquitous in daily life, allowing us to walk and drive a car, and plays an important role in many technologies such as tires, brakes, rubber seals, conveyer belts, and footwear. In recent years, soft and extensible materials have been used in state-of-the-art technologies such as wearable sensors and stretchable electronics, in which the materials can deform under relatively small amounts of load, owing to a high effective compliance resulting from either low modulus or

geometric design. Understanding the role of effective compliance on the frictional properties of materials, from both experimental and theoretical points of view, has important implications for such technologies. In the third chapter, a comprehensive study that combines theory and experiments to investigate how the frictional responses of a system, i.e. static and kinetic frictions, depend on the effective compliance of the system is presented. For this purpose, a translational actuator pulled a steel sled resting on top of an elastic strip across a glass substrate, while the strip was only bonded to the leading edge of the sled. The friction force and local deformation along the length of the strips were measured using a force sensor and a camera, respectively. By increasing the effective compliance of the strip, the static friction force was found to decrease dramatically, while the kinetic friction force increased significantly. For sufficiently soft strips, there was no observable static peak, whereas there was a slope change in the force-displacement curve at the point where progressive slippage initiated at the leading edge. A theoretical model, somewhat analogous to an extension of the classical shear lag model to incorporate elastic-plastic interlayers, is proposed to predict the friction response as a function of effective compliance. Three regions, based on the local deformation obtained from image analysis, are defined along the length of the extensible strip, namely no-slip, transition, and slip zones. Using longitudinal force equilibrium, the governing equations corresponding to each region are derived. The results obtained from the shear lag analysis are compared with experimental results and shown to be in good agreement. We believe that this study provides insights into the effect of axial compliance on the frictional response of materials, paving the way for design and optimization of systems where the static and kinetic friction forces play an important role.

Chapter IV: The effect of normal force and rate on kinetic coefficient of friction of elastomeric materials

Understanding the frictional response of materials is a major and a practical topic of interest in the field of mechanical engineering. The well-known empirical Coulomb's friction law, which suggests no normal load dependence for the coefficient of friction (COF), has been successfully applied to many physical systems including metals and polymers. However, in some situations, Coulomb's friction law does not hold, resulting in a dependence of the COF on the normal force. Several mechanisms contribute to the friction of viscoelastic materials, namely bulk viscoelastic dissipation, work of adhesion or surface energy, and work of adhesion hysteresis. The

corresponding friction force contributions are well known as *hysteresis friction*, *adhesion friction*, and *cohesion friction*, respectively. In the fourth chapter, the effect of normal force on the kinetic coefficient of friction of two different elastomers, namely acrylic and silicone-based elastomers, is investigated. The kinetic COF was quantified using an instrumented (with piezoelectric force sensors) pendulum setup to measure normal and friction forces exerted within the contact region between the elastomers and a macroscopically smooth poly(methyl methacrylate) (PMMA) substrate. Although both systems tended to obey Coulomb's frication law at higher loads, we found contradictory responses at very low normal forces: the COF of acrylic increased with increasing normal force, while that of the silicone decreased. The friction response of the silicone was consistent with the adhesion friction found in the literature, whereas the acrylic response was the opposite of trends found in the literature. To further explore the origin of these responses, we changed the surface response at the interfaces by using graphite powder, and also varied the sliding velocity at the contact interfaces. In addition, drop tests were implemented to characterize the surface hysteresis of the elastomers. We found that the acrylic response anomaly at very low normal forces likely originates from the rate dependent response of surface properties, giving rise to a hysteretic contribution even on a smooth substrate. The role of rate dependent cohesion hysteresis friction, arising from viscoelastic dissipation and low storage modulus of acrylic elastomer, on the frictional response at low normal forces is discussed. This study could improve insights gained from Dynamic Mechanical Analysis (DMA) data when obtaining and interpreting the effect of normal force on kinetic COF of elastomers with potential applications to tires, shoes, etc. where friction plays an important role.

Chapter V: Revisiting the generalized scaling law for adhesion: role of compliance and extension to progressive failure

- Mojdehi, Ahmad R., Douglas P. Holmes, and David A. Dillard. " Revisiting the generalized scaling law for adhesion: role of compliance and extension to progressive failure." *Soft Matter*, (2017), DOI: 10.1039/c7sm01098b.

Significant recent efforts have been devoted to understanding and mimicking adhesion mechanisms found in many organisms in nature, such as geckos and insects. Adhesion failure of bio-inspired adhesive systems has recently been studied, showing that bond strength scales with the square root of the ratio of contact area to the total system compliance ($\sqrt{A/C}$), and its validity

has been successfully demonstrated for a broad range of systems. This approach is purportedly a simplification of Griffith's classic approach for a set of applicable scenarios involving unstable or catastrophic failure of rate-independent systems. This simplified model, however, appears to differ from the classic fracture mechanics approach, where bond strength should scale with the reciprocal square root of the derivative of the system compliance with respect to the bond area ($\sqrt{\partial A/\partial C}$). This chapter addresses this apparent discrepancy by examining the roles of both load train and specimen compliances. A generalized scaling law, based on the classical fracture mechanics approach, is developed to predict the bond strength of adhesive systems. The proposed scaling relationship depends on the rate of change of bond area with compliance, rather than the ratio of area to compliance. This distinction can have a profound impact on the expected bond strength of systems, particularly when failure mechanism changes or the compliance of the load train is increased. Based on the classical fracture mechanics approach for rate-independent materials, the load train compliance should not affect the force capacity of the adhesive system, while when the area to compliance ratio is used as scaling parameter it directly influences the bond strength, making it necessary to distinguish compliance contributions. To verify the scaling, single lap shear tests were performed for a given pressure sensitive adhesive (PSA) tape specimens with different bond areas, number of backing layers, and load train compliance. The shear lag model was used to derive closed-form relationships for the system compliance and its derivative with respect to the bond area. Digital image correlation (DIC) technique is implemented to verify the non-uniform shear stress distribution obtained from shear lag model in a lap shear geometry. The conditions where the two models deviate from each other are discussed and demonstrated. We found three regions when comparing the $\sqrt{\partial A/\partial C}$ and $\sqrt{A/C}$ scaling parameters: 1) low values of scaling parameters where the two scaling parameters are identical. This region corresponds to the cases with relatively rigid backing where the shear stress is uniform and the failure is catastrophic. 2) Intermediate values of scaling parameters where the two scaling parameters slightly deviate from each other, corresponding to the cases with non-uniform shear stress distribution along the length and catastrophic failure. 3) Large values of scaling parameters where the deviation is significant between the two scaling parameters and is associated to the cases with non-uniform shear stress distribution along the length and progressive failure. The results obtained from this approach could lead to a better understanding of the relationship between the bond strength and the geometry, mechanical properties of adhesive systems.

2 Buckling of Elastic Beams Embedded in Granular Media

Ahmad R. Mojdehi[1], Behrouz Tavakol[1], Wesley Royston[1], David A. Dillard[1], and Douglas P. Holmes[2]

[1] Biomedical Engineering and Mechanics, Virginia Tech, Blacksburg, VA, 24061

[2] Mechanical Engineering, Boston University, Boston, MA, 02215

(Mojdehi, Ahmad R., Behrouz Tavakol, Wesley Royston, David A. Dillard, and Douglas P. Holmes. "Buckling of elastic beams embedded in granular media." *Extreme Mechanics Letters* 9 (2016): 237-244)

2.1 Introduction

Slender rods and beams, commonly referred to as *elastica*, can be used to describe carbon nanotubes, fiber optic cables, spider silk, and human hair. In many engineering applications, it is desirable to insert and manipulate an elastic beam within complex media, such as granular beds or soft tissues. Burrowing a flexible structure through fragile media requires understanding the coupled interactions between the geometrically nonlinear structure and its reconfigurable surroundings. The complex interplay between the elastic strip and its surroundings has been studied as the beam is lowered into a fluid [1], constrained along its edges [2], delaminated from a surface [3], embedded on an elastomeric matrix [4, 5], and compressed while resting on an elastic foundation [6-10] and floating on the surface of water [11]. The fundamental structural interactions of the constrained elastica have direct analogies to plant root growth [12-14], bending and buckling of oil pipelines [15, 16], and the creation of underground infrastructures using microtunneling and trenchless technology [17].

The interaction between a flexible beam and a granular medium can be modeled as a beam on an elastic foundation with a series of springs acting along the length of the beam [18]. Winkler's model has been widely used in problems involving soil--structure interactions when pile-supported structures *e.g.* bridges and piers, transfer load to the surrounding foundation *via* lateral, shear, and/or axial interaction. The buckling behavior of the pile was modeled by assuming that the soil subgrade modulus, which is the ratio of lateral soil reaction per unit length over its lateral deflection, is constant and linearly increasing with depth [19]. This analysis was later extended to a general power distribution of the soil subgrade modulus with respect to the depth to find the critical buckling load of partially embedded piles in soil [20]. The energy method was used to obtain the buckling load of the piles embedded in soil with different boundary conditions [21-23]. The effect of skin friction, the applied friction force per unit length from the soil to the sides of the

pile, on the buckling load of embedded piles was found to be insignificant, resulting to less than 10% variation in the buckling load [20, 24, 25]. This negligible friction effect could be the result of a small friction force along the length of the pile compared to the applied critical buckling load, and also small displacement in the vertical direction. Furthermore, an accurate measurement of the soil subgrade modulus through the depth is important for more realistic predictions of the piles' buckling load and lateral deflection. For example, a horizontal force can be applied on the top of a partially embedded rigid or flexible pile, allowing an estimate of the coefficient of subgrade reaction of the soil [26-30].

Several experimental, analytical, and numerical works have been performed regarding the burrowing of a flexible structure through complex media. For example, the concept of a beam on elastic foundation was used for real-time steering of a robotic flexible needle to avoid obstacles in soft tissue [31], for microneedle design [32], and to determine the buckling load of flexible needles in homogeneous and multi-layered tissue [33]. Plant root growth through granular media was investigated using photoelastic grains to evaluate the force chains in the system [34]. The Discrete Element Method (DEM) is developed for the force chain buckling of densely packed granular materials, and also simulation of keel penetration into viscoelastic granular media [35, 36]. The finite element method (FEM) is also widely used in simulations of flexible needle insertion into soft tissues, considering the needle-tissue interaction [37-40].

A granular system consists of a large number of particles/grains that are packed next to each other and are massive enough so that the Brownian motion is insufficient to change its volume fraction/packing density [41]. Therefore, an external force such as tapping [42], shearing [43], or both [44] is required to achieve different volume fractions. Several papers have investigated the penetration of a rigid intruder into granular materials. Schroter *et al.* [45] studied the phase transition in volume fraction of a granular system during penetration of a rigid rod. Stone *et al.* [46] evaluated the effect of container boundaries and local jamming on the force-displacement response of a rigid flat plate vertically penetrating into a dense granular medium. Toiya *et al.* [47] analyzed grain rearrangements due to penetration of a rigid rod (penetrometer) through a granular medium. However, the effect of the intruder's flexibility and boundary conditions on the response of granular media and their interaction are not completely understood. Before performing such a study, investigation of the buckling behavior of a flexible intruder, passively embedded within a granular medium, is of importance. Moreover, the lack of comprehensive studies that combine

experiments and theories to investigate how the buckling response depends on geometric, boundary, interaction, and material parameters, as well as validate existing theories, is obvious.

In this paper, an experimental and analytical study of the buckling behavior of an elastic slender beam into granular media is performed. The buckling loads of beam with different flexural rigidity (*EI*) and boundary conditions *e.g.* clamped-clamped (C-C) and clamped-pinned (C-P) are identified. Two media with different grain sizes, polydispersities, and depths are used to evaluate the buckling load of an elastic beam embedded in a medium. The lateral force-displacement response of the grains is measured by burrowing a rigid intruder into the medium laterally from the side. The stiffness of the effective support along the depth of the beam is found to vary linearly. Using the energy method and the concept of a beam on elastic foundation, the governing equations corresponding to the buckling behavior of an elastic beam embedded into granular media are developed. The effect of boundary conditions on the buckling load and the interaction between beam and its surrounding media are investigated. Our findings suggest that there is a characteristic penetration ratio at which the beam cannot sense the end boundary condition, resulting in a convergence of the buckling load for C-C and C-P cases. Moreover, the nondimensional stiffness parameter plays an important role in both the buckling load and the characteristic penetration ratio of the beam.

2.2 Experiments

The buckling experiment was performed using a setup shown in Figure 2-1b. An elastic beam (Polycarbonate, McMaster-Carr) of different lengths (60 mm, 70 mm, 80 mm, and 90 mm) and bending rigidities ($6.7\text{x}10^{-5}$ Nm^2 and $27.1\text{x}10^{-5}$ Nm^2) was clamped to a load cell with full range of 600g (OMEGA, LCAE-600G) loaded axially in a container with grains (glass beads from Glen Mills Inc. with a density of 3.75 g/cm^3) of two different sizes (average diameter of: 150±50 μm and 900±100 μm) and seven different penetration ratios (the ratio of grains' height to beam's length) between 0 and 0.85, by a translational actuator (PI, M-229.26S) at 0.1 mm/sec. The width of the container was slightly larger than that of the beam to prevent wall friction between the beam and container. Two different end boundary conditions, *i.e.* clamped-clamped (C-C) and clamped-pinned (C-P) were enforced. The axial load versus displacement curve of the beam was obtained and the buckling load was calculated from the plateau value of the curve. The final buckling load was obtained from averaging three separate buckling runs. Moreover, to measure the lateral

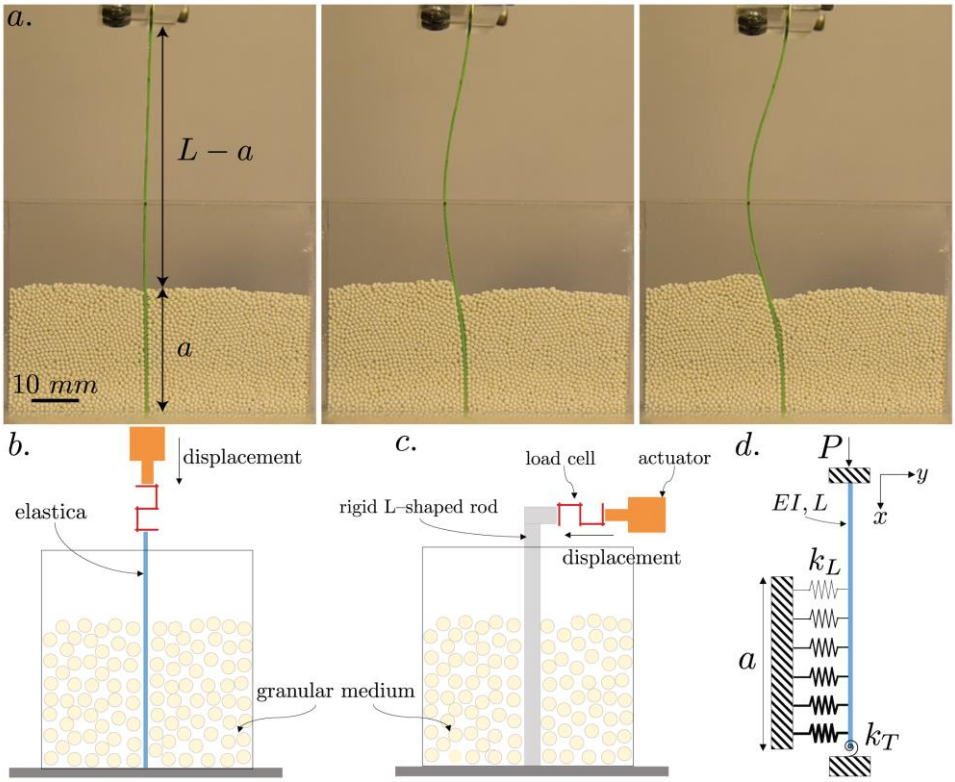

Figure 2-1. a) An elastic beam partially embedded within a granular medium. b) The experimental setup for the buckling experiment c) The experimental setup for the lateral force displacement experiment d) Winkler model used in the theoretical model

stiffness of granular support, the same load cell and actuator were used in a horizontal configuration, as shown in Figure 2-1c. A relatively rigid (with respect to the grains stiffness) L-shaped intruder (width 7 mm, thickness 3.2 mm, and height 90 mm), made of PMMA (McMaster-Carr) , clamped to the load cell, was directed into the grains (height: 70 mm) in the horizontal direction, laterally from the side. Containers with different lengths were examined to see the effect of side boundaries on the lateral force-displacement response of grains. It has been found that for container's length over grains' depth ratio of 1/3 or higher, this effect was negligible and the force-displacement response was independent of the side boundaries. The minimum container's length over grains' depth ratio, for both buckling and lateral force-displacement experiments, were chosen to be 0.8 and 0.4 respectively, higher than the limit at which the boundary effect is significant. For the buckling experiments the effective length of the container is half of the length of container, as the beam is placed at the middle. The lateral force-displacement of the grains was obtained and their effective stiffnesses were calculated and used in the theoretical model. Figure 2-2a and b show the lateral force-displacement response of the granular support with different grain sizes and

two representative axial force-displacement curves, respectively. We verified that the variation of the stiffness through the depth was linear by burrowing an intruder from the lateral side at different depth of the medium. Before each experiment, the container was tapped at least three times to let the grains settle down on their compact configuration. The volume fractions of the grains were kept nearly constant by weighing the grains and measuring the height corresponding to each penetration ratio.

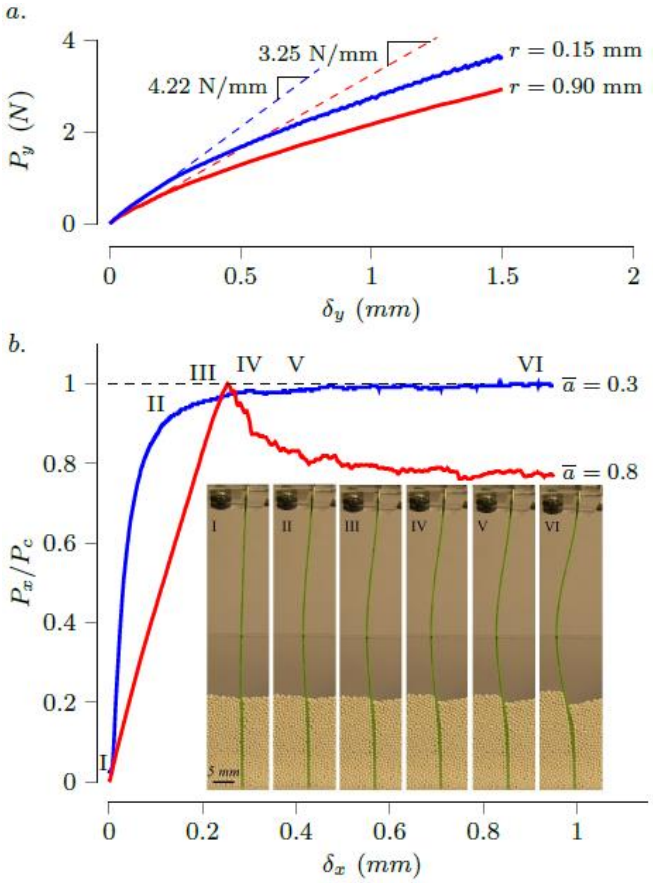

Figure 2-2. a) Lateral force-displacement response of grains with two different sizes and polydispersities. Initial slopes were used in the theoretical model to calculate the constant *c* of the effective stiffness of granular support. b) Axial force trace of the beams (*L=90*mm, $EI=6.7x10^{-5}$ Nm^2, blue line: penetration ratio=*0.3*, red line: penetration ratio=*0.8*). Inset: Sequences of grains and the beam deformation ($\bar{a}=0.8$) during buckling at different axial displacements (*0, 0.1, 0.2, 0.3, 0.4, 0.9 mm*).

2.3 Theoretical Model

An energy method is used to evaluate the buckling behavior of the 2D planar elastic beam embedded into a complex medium. The important parameters in this problem are the beam's length *L* and bending rigidity *B=EI*, where *E* is the elastic modulus and *I* is the second moment of area.

The proposed model will consider three types of behavior (1) no penetration, (2) full penetration, and (3) partial penetration. Buckling in the absence of supporting media is the classical example of Euler buckling, and the beam will be modeled with two boundary conditions, *i.e.* C-C and C-P, in which the first letter corresponds to the BC at the top and the second letter corresponds to the embedded end at the bottom of the beam. When the elastic beam is fully/partially penetrated, the surrounding media is treated as lateral springs of stiffness k_l distributed along the beam's length. Figure 2-1d shows the schematic of partial penetration case with corresponding parameters. The rotational spring constant (k_T) at the end is assumed to be zero for the C-P and infinity for the C-C case.

The governing equations that describe these three cases can be determined using an energy minimization approach. The total potential energy for the system is the sum of the strain energy of the beam $\mathcal{U}_b$, and the potential energies of the point load $\mathcal{V}_p$ and springs $\mathcal{V}_{sl}$ and $\mathcal{V}_{st}$, such that $\Pi = \mathcal{U}_b + \mathcal{V}_p + \mathcal{V}_{sl} + \mathcal{V}_{st}$. The total strain energy of the elastic beam is $\mathcal{U}_b = \frac{B}{2}\int_L w''^2 dx$, the potential energy of the point load is $\mathcal{V}_p = -\frac{P}{2}\int_L w'^2 dx$, the potential energy from the lateral springs of stiffnesses k_l is $\mathcal{V}_{sl} = \frac{1}{2}\int_a k_l w^2 dx$, and the potential energy from the rotational spring of stiffnesses k_T is $\mathcal{V}_{st} = \frac{1}{2}k_T w_L'^2$, where the prime symbol denotes a derivative with respect to x. As elastic buckling, not post-buckling, is of interest in this work, the beam strain energy is based on small strains assumption without considering any nonlinearity in the geometry and materials. The stiffness of granular support is assumed to vary linearly with respect to the depth ($k_l = c(x-L+a)$), where c is the stiffness constant of the grains with units of N/m^3. The relevant parameters are nondimensionalized in the following manner, $\bar{x} = x/L$, $\bar{w} = w/L$, $\bar{a} = a/L$, $\alpha = PL^2/EI$, $\eta = cL^5/EI$. Energy minimization leads to the following equilibrium equations,

$$\bar{w}'''' + \alpha\bar{w}'' + \eta(\bar{x} + \bar{a} - 1)\bar{w} = 0 \qquad (2.1)$$

which simplifies to the familiar form for the buckling of an Euler column when there is no penetration, *i.e.* $\eta=0$, and full penetration when $\bar{a}=1$. This equation cannot be solved analytically, and the Ritz approximate method is used to obtain buckling loads with the appropriate boundary condition, *i.e.* C-C or C-P. A polynomial shape function is used to approximate the deflection field along the length of the beam, *i.e.* $\bar{w} = \sum_{i=1}^{n} C_i(1-\bar{x})\bar{x}^{i+1}$, where it automatically satisfies the

essential boundary conditions for C-P case. A convergence analysis was performed and the polynomial shape function order was chosen to be nine, beyond which there was no significant change in the buckling load for higher order shape functions.

The final solution is obtained by substituting the shape function into equation (2.1) and minimizing the total strain energy with respect to constants C_i, *i.e.* $\partial\Pi/\partial C_i = 0$. The stiffness coefficient of the lateral springs, c, depends on the properties of grain such as roughness, homogeneity, and volume fraction, and will be deduced from the experiments.

2.4 Results and Discussion

We performed the lateral force-displacement experiments at different grain depths and found a linear variation in the stiffness of granular support as a function of depth, which is consistent with results obtained from literature [26]. It was shown that the packing density of the lower grains is increased due to the weight of upper grains, which results in effectively increasing the stiffness of the media as a function of depth [26]. However, the overburden mass of the top grains on the lower grains could result in an increase in the normal force and therefore an increase in internal friction forces between grains, leading to effectively increasing the stiffness of the media along the depth. Therefore, by writing a force balance between the total force obtained from the lateral force-displacement response and the reaction force from springs with a linear variation of stiffness with respect to the depth, the constant c of the springs is calculated as $\int_L c(x - L + a)dx = k_l$, where k_l is the initial slope of the lateral force-displacement curve shown in Figure 2-2a and a=L for the lateral force-displacement experiment shown in Figure 2-1, resulting in $c = 2k_l/L^2$ used in the theoretical model.

The lateral force-displacement response of the grains with two different sizes and polydispersities are depicted in Figure 2-2a, which shows that the stiffness support with smaller grains is slightly higher than that of the bigger grains. However, no relation was found between the size and volume fraction/resistant force of spherical particles in the literature [46, 48]. Although, there is a direct relation between the polydispersity and the volume fraction[49], showing that by increasing the polydispersity, the volume fraction of the grains increases resulting in more packed grains and therefore more resistance to the external forces. We tried to keep the volume fractions constant by weighing the grains and measuring the height associated with each penetration ratio, but since the ratio of container length to grains' height was high (within the range of 0.8-5), this measurement

was not sensitive enough to keep the volume fractions constant, as a very small change in the volume fraction results to a dramatic change in the resistance force of the grains [45]. Hence, as the polydispersity of the smaller grains is higher than the bigger grains (33% vs 11%), the increase in stiffness could be associated with the difference in the polydispersities, and not the size of the grains. Since we are dealing with linear elastic buckling at small strains, the initial slope of the force-displacement curves was chosen as the stiffness of the grains. However, there is a change (decrease) in the slope of force-displacement curves at higher displacement values that may originate from the slippage of the grains on each other, leading to a decrease in the resistance of the grains due to a transition from static to kinetic friction. The interactions between the postbuckling beam and the reconfigurable surrounding media will be investigated in a subsequent work.

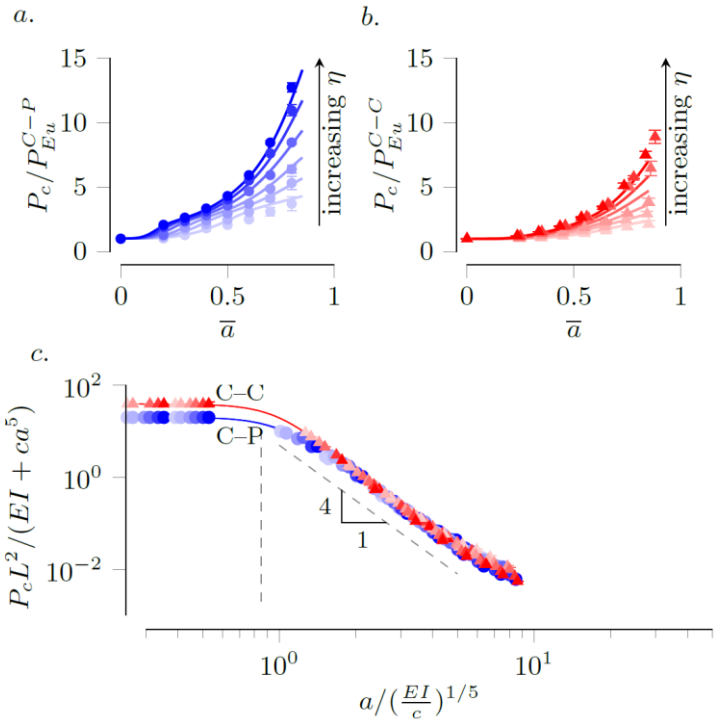

Figure 2-3. Nondimensional buckling loads vs nondimensional penetration depths for different values of η. Excellent agreement is found between experimental results (markers) and the theoretical predictions (solid lines) a) C-P boundary condition, b) C-C boundary condition, c) collapsed curves using new nondimensional parameters.

Figure 2-2b presents representative axial force versus displacement curves together with the sequence of grain and beam deformation during buckling. It can be seen that the force increases with displacement monotonically, resulting in a plateau in the force-displacement response. The

buckling load was chosen to be the plateau value of the force-displacement response. However this response was not identical for all cases. For example, for the higher penetration ratio, there was a peak and then a drop and plateau in the force-displacement curve that was most likely due to postbuckling and local yielding of the grains. In those cases, the peak values were chosen as the buckling load of the beams (as shown in Figure 2-2b).

Figure 2-3a and 3b show a comparison of results obtained from the model with those of experiments for C-P and C-C boundary conditions, respectively. In these figures, the nondimensional buckling load is plotted versus nondimensional penetration ratio, $\bar{a}$. Each line corresponds to a different η value that depends on the beam length (L), bending rigidity (EI), and lateral stiffness constant of the media (c). Physically, the η can be defined as the ratio of the granular support effective stiffness to the beam's effective stiffness. The experimental and analytical nondimensional buckling loads are calculated by dividing the corresponding buckling loads by experimental and analytical Euler buckling load, respectively.

By increasing η, the nondimensional buckling load increases as a function of penetration ratio $\bar{a}$. There is good agreement between the results obtained from experiments and predictions from the theoretical model. The effect of support is more significant for C-P compared to the C-C boundary condition, as the ratio of the buckling load to the Euler buckling load is higher for the C-P case compared to the C-C case. This could result from different deformation profiles (mode shapes) in these two boundary conditions, where in the C-P condition, more grains interaction forces are involved at buckling whereas there are less beam--grains interactions in the C-C, based on the mode shapes of the beam. The onset of an increase in the buckling load as a function of penetration ratio, that is where the effect of grains on buckling load becomes important, for the C-C and C-P boundary conditions are about 0.29 and 0.15 (10% increase in predicted buckling load, average of 12 different η), respectively, confirming the effect of mode shapes on the buckling loads of the beam.

To rationalize these results, we consider a mechanical analog of this problem where an overhanging beam on an elastic foundation only exerts a reaction force where it contacts the beam, *i.e.* $EIw'''' + Pw'' + c(x)w = 0$, where $c(x) = cx$ when $x<a$, and $c(x) = 0$ when $x>a$. From dimensional analysis with the appropriate characteristic length scales, a dimensionless form of the applied load emerges as $\alpha_N = PL^2/(EI + ca^5)$. This is analogous to treating the resistance of the

beam and granular medium as springs acting in parallel with an equivalent bending rigidity of $EI+ca^5$, where EI and ca^5 are the effective bending rigidity of the beam and support medium, respectively. There is also a characteristic length scale, similar to the one in the beam on elastic foundation [50], but with linear variation of the stiffness, $L_c = (EI/c)^{1/5}$. When we plot the new nondimensional buckling load parameter, α_N, as a function of characteristic penetration ratio, $\bar{a}_N = a/L_c$=, all the data for different values of η collapse onto one curve (Figure 2-3c). It is clear that there is a change in the slope of two curves for C-C and C-P BC at about $\bar{a}_N$*=0.85* which is close to the reported limit for short beams on a uniform elastic foundation [50]. Below $\bar{a}_N$*=0.85* the embedded length of the beam is relatively rigid, resulting in a buckling load close to the Euler case, and above $\bar{a}_N$*=0.85*, the bending deformation of the embedded beam becomes important, leading to more interaction with surrounding media and deviation from the Euler buckling load. There is a small gap between the C-C and C-P boundary conditions in the *x*-axis at low values of $\bar{a}_N$, where the deviation from Euler buckling load begins. This gap is due to the different mode shapes corresponding to each boundary condition, resulting in fewer beam-grain interactions in the C-C case compared to the C-P case, which causes the curve for the C-C case to decrease at a slightly higher $\bar{a}_N$ value. Moreover, the vertical shift between two boundary conditions is due to the fact that the dimensionless Euler buckling load parameter (when *a=0*) for the C-C and C-P cases are different, namely $4\pi^2$ and $2\pi^2$, respectively. The slope of the change in nondimensional buckling load, α_N, with respect to $\bar{a}_N$ is found to be *-4*. While the mentioned dimensionless parameters collapse the data, we do not as yet have a sense of the physical nature of this power law.

Furthermore, by increasing the penetration ratio, there is a characteristic point at which the beam cannot sense the BCs at the end, resulting in the convergence of the buckling loads for C-C and C-P boundary conditions. We call the minimum penetration ratio at which the C-P and C-C buckling loads converge, characteristic penetration ratio, $\bar{a}_{c1} = a_{c1}/L$. This condition happens for the more flexible beams, where the rigidity of the beam is lower than the effective stiffness of granular support, leading to the confinement of the lower portion of the beam inside the grains and acting as a secondary boundary condition that is the same for C-C and C-P conditions. This is analogous

to a long beam on an elastic foundation, where the counter effect of the ends boundary conditions on each other is negligible [50].

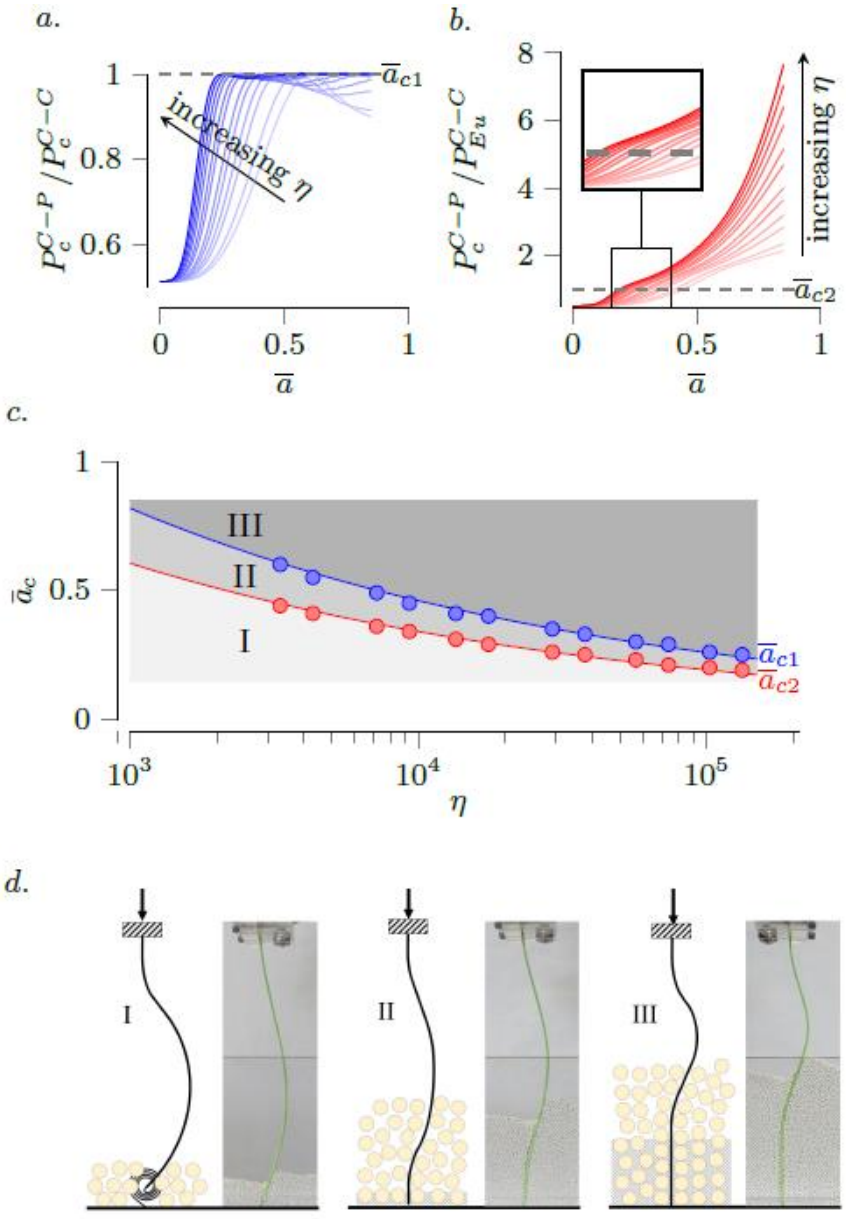

Figure 2-4. a) Predicted C-P buckling load over predicted C-C buckling load versus penetration ratio $\bar{a}$, b) Predicted C-P buckling load over Euler C-C buckling load versus penetration ratio $\bar{a}$, c) characteristic penetration ratio as a function of η in semilog (x) scale. Markers are obtained from the intersection of dashed line and the curves in (a) and (b). Solid lines are the fitted curves obtained from the scaling law in equation (1.2), d) different mode shapes/end BC corresponding to different regions in (c).

To illustrate this buckling load convergence, we plot the theoretical buckling load of the C-P beam relative to the C-C beam in Figure 2-4a as a function of penetration depth $\bar{a}$ for various values of η. For lower values of η, there is a deviation from the converged buckling load beyond the characteristic penetration ratio, suggesting that the stiffness of the medium is not high enough relative to the stiffness of the beam. An alternative metric is found by comparing the buckling load of C-P case to the classical C-C Euler buckling load, where we can find the characteristic penetration ratio $\bar{a}_{c2} = a_{c2}/L$ at which the buckling load of C-P case and Euler buckling load for C-C BC are the same (Figure 2-4b). For the penetration ratios lower than $\bar{a}_{c2}$, the support at the end of C-P beam can be modeled with a rotational spring at the end.

Finally, the characteristic penetration ratios, $\bar{a}_{c1}$ and $\bar{a}_{c2}$, are plotted as a function of η in a semilog scale in Figure 2-4c. We rationaize this results by considering the definition of nondimensional stiffness parameter, $\eta = cL^4/\frac{EI}{L}$, which is the ratio of the medium's effective stiffness to the beam's effective stiffness. The parameter η can be rewritten such that the rigidity from the granular medium is in terms of the length of the beam in contact with the grains, such that $\eta_c = ca_c^4/\frac{EI}{L}$, where a_c is the characteristic grain height at which the effective stiffness of granular support is dominated by the effective stiffness of the beam $\bar{a}_{c1}$ or one where the C-P buckling load is lower than Euler C-C buckling load ($\bar{a}_{c2}$). This leads to a simple scaling,

$$\bar{a}_c = \left(\frac{\eta_c}{\eta}\right)^{1/4} \tag{2.2}$$

Here, $\bar{a}_c$ can be replaced by either $\bar{a}_{c1}$ or $\bar{a}_{c2}$ for the two above mentioned cases. Furthermore, we identify three regions in Figure 2-4c where the interaction of medium with beam can be modeled differently. The first region is where the effective stiffness of granular support is low compared to the beam's effective stiffness and it can be modeled by a rotational spring at the end of the beam (Figure 2-4d(I)). The second region corresponds to the intermediate effective stiffness ratio where the end BC is clamped and the surrounding medium is modeled by lateral springs (Figure 2-4d(II)). Finally, in the third region where the effective stiffness ratio is very high, the beam cannot sense the end boundary conditions, resulting in effectively moving the end clamped BC to a higher height (Figure 2-4d(III)).

2.5 Conclusion

In conclusion, we have investigated the buckling response of elastic slender beams embedded in granular media, using both experiment and theory. Different beams with different bending rigidities, lengths, and boundary conditions are embedded in two different granular media with different grain sizes and polydispersities. The buckling load is obtained as a function of penetration ratio (the ratio of the grains' height over beam's length), where zero penetration ratio corresponds to Euler buckling and the penetration ratio equal to unity is associated with the beam fully embedded in the medium. The energy method is used to predict the buckling load using a series of springs along the length of the beam based on a beam on elastic foundation concept. The effective stiffness of the medium are measured from the slope of the force-displacement response of the grains by burrowing a rigid beam horizontally from the side. The stiffness of the granular support increases linearly with respect to the depth. We found that the beam--grains interaction is more significant in C-P boundary condition compared to the C-C case. The buckling load had a rise (10% increase) at lower penetration ratio for the C-P case compared to the C-C one, namely 0.15 for the former and 0.29 for the latter. This difference is thought to emerge from different mode shapes and deformation profiles along the length of the beam for C-C and C-P BCs, resulting in different interactions between the beam and surrounding medium. Moreover, buckling loads of C-P and C-C BCs converge at a characteristic penetration ratio, where the stiffness of granular support is considerably higher than the rigidity of the beam, resulting in confinement of the lower portion of the beam that prevents the beam from sensing its embedded end boundary condition. We find a scaling law relationship between the characteristic penetration ratio and the nondimensional stiffness parameter, allowing characterization of three distinct regions where the interaction of the beam and surrounding medium is different depending on the ratio of the granular support effective stiffness over beam's effective stiffness. Overall, we identify two dimensionless parameters that provide insight to the buckling of flexible structures into complex and fragile media. The reduced buckling load, ($PL^2/(EI+ca^5)$) describes the structure's stability when partially embedded in a medium with a variable stiffness. The characteristic penetration ratio, $\bar{a}_c$, dictates different beam-grain interaction regimes, ultimately influencing the effect of the boundary condition at the embedded end of the beam.

Acknowledgments

The authors would like to thank the Provost's Office and College of Engineering for partial support of ARM and the Biomedical Engineering and Mechanics (BEAM) Department for use of equipment. DPH acknowledges financial support from the NSF CAREER CMMI--1454153.

References

[1] Wang, C.Y., *Buckling and Postbuckling of a Long, Hanging Column Lowered into a Fluid.* International Journal of Solids and Structures, 1992. **29**(2): p. 243.

[2] Domokos, G., P. Holmes, and B. Royce, *Constrained Euler Buckling.* J. Nonlinear Sci., 1997. **7**: p. 281.

[3] Wagner, T.J.W. and D. Vella, *The }Sticky Elastica}: delamination blisters beyond small deformations.* Soft Matter, 2013. **9**(4): p. 1025.

[4] Su, T., et al., *Buckling of an elastic rod embedded on an elastomeric matrix: planar vs. non-planar configurations.* Soft matter, 2014. **10**(33): p. 6294-6302.

[5] Miller, J.T., et al., *Buckling of a thin elastic rod inside a horizontal cylindrical constraint.* Extreme Mechanics Letters, 2015. **3**: p. 36-44.

[6] Nicolau, A.M. and J.V. Huddleston, *The Compressible Elastica on an Elastic Foundation.* Journal of Applied Mechanics, 1982. **49**: p. 577.

[7] Brangwynne, C.P., et al., *Microtubules can bear enhanced compressive loads in living cells because of lateral reinforcement.* The Journal of cell biology, 2006. **173**(5): p. 733-741.

[8] Plaut, R.H. and L.N. Virgin, *Vibrations and large postbuckling deflections of optimal pinned columns with elastic foundations.* Structural and Multidisciplinary Optimization, 2010. **40**(1-6): p. 157-164.

[9] O'Keeffe, S.G., et al., *Growth-induced axial buckling of a slender elastic filament embedded in an isotropic elastic matrix.* International Journal of Non-Linear Mechanics, 2013. **56**: p. 94-104.

[10] Shan, W.L., et al., *Attenuated short wavelength buckling and force propagation in a biopolymer-reinforced rod.* Soft Matter, 2013. **9**(1): p. 194-199.

[11] Audoly, B., *Localized buckling of a floating elastica.* Physical Review E, 2011. **84**(1): p. 011605.

[12] Wendell, D.M., et al., *Experimental Investigation of Plant Root Growth Through Granular Substrates.* Experimental Mechanics, 2011. **52**(7): p. 945-949.

[13] Kolb, E., C. Hartmann, and P. Genet, *Radial force development during root growth measured by photoelasticity.* Plant and Soil, 2012. **360**(1-2): p. 19-35.

[14] Silverberg, J.L., et al., *3D imaging and mechanical modeling of helical buckling in Medicago truncatula plant roots.* Proceedings of the National Academy of Sciences, 2012. **109**(42): p. 16794-16799.

[15] Santillan, S.T., L.N. Virgin, and R.H. Plaut, *Static and Dynamic Behavior of Highly Deformed Risers and Pipelines.* Journal of Offshore Mechanics and Arctic Engineering, 2010. **132**(2): p. 021401.

[16] Santillan, S.T. and L.N. Virgin, *Ocean Engineering.* Ocean Engineering, 2011. **38**(13): p. 1397-1402.

[17] Kramer, S.R., W.J. McDonald, and J.C. Thomson, *An Introduction to Trenchless Technology*. 1992, London: Chapman and Hall.

[18] Winkler, E., *Die Lehre von Elastizitat und Festigkeit*. 1867: Prague.

[19] Davisson, M.T. and K.E. Robinson. *Bending and buckling of partially embedded piles*. in *Soil Mech \& Fdn Eng Conf Proc/Canada/*. 1900.

[20] Gabr, M.A., J.J. Wang, and M. Zhao, *Buckling of piles with general power distribution of lateral subgrade reaction.* Journal of geotechnical and geoenvironmental engineering, 1997. **123**(2): p. 123-130.

[21] Prakash, S., *Buckling loads of fully embedded vertical piles.* Computers and Geotechnics, 1987. **4**(2): p. 61-83.

[22] Reddy, A.S. and A.J. Valsangkar, *Buckling of fully and partially embedded piles.* Journal of the Soil Mechanics and Foundations Division, 1970. **96**(6): p. 1951-1965.

[23] Budkowska, B.B. and C. Szymczak, *Partially embedded piles subjected to critical buckling load—sensitivity analysis.* Computers \& structures, 1996. **61**(1): p. 193-196.

[24] Heelis, M.E., R.P. West, and others, *The stability of uniform-friction piles inhomogeneous and non-homogeneous elastic foundations.* International journal of solids and structures, 1999. **36**(22): p. 3277-3292.

[25] Heelis, M.E., Pavlovi\'c, M. N., and R.P. West, *The analytical prediction of the buckling loads of fully and partially embedded piles.* Geotechnique, 2004. **54**(6): p. 363-373.

[26] Terzaghi, K., *Evalution of conefficients of subgrade reaction.* Geotechnique, 1955. **5**(4): p. 297-326.

[27] Prasad, Y.V.S.N. and T.R. Chari, *Lateral capacity of model rigid piles in cohesionless soils.* Soils and Foundations , 1999. **39**(2): p. 21-29.

[28] Guo, W.D., *Laterally loaded rigid piles in cohesionless soil.* Canadian Geotechnical Journal, 2008. **45**(5): p. 676-697.

[29] Reese, L.C., W.R. Cox, and B.R. Grubbs, *Lateral load tests of instrumented piles in sand at Mustang Island.* A report to shell development company, Houston (TX), 1967.

[30] Kobayashi, N., et al., *Estimation of horizontal subgrade reaction coefficient by inverse analysis.* Computers and Geotechnics, 2008. **35**(4): p. 616-626.

[31] Glozman, D. and M. Shoham, *Image-guided robotic flexible needle steering.* Robotics, IEEE Transactions on, 2007. **23**(3): p. 459-467.

[32] Ramasubramanian, M.K., O.M. Barham, and V. Swaminathan, *Mechanics of a mosquito bite with applications to microneedle design.* Bioinspiration \& biomimetics, 2008. **3**(4): p. 046001.

[33] He, X., Y. Chen, and L. Tang. *Modeling of flexible needle for haptic insertion simulation*. in *Virtual Environments, Human-Computer Interfaces and Measurement Systems, 2008. VECIMS 2008. IEEE Conference on*. 2008.

[34] Wendell, D.M., et al., *Experimental investigation of plant root growth through granular substrates.* Experimental mechanics, 2012. **52**(7): p. 945-949.

[35] Tordesillas, A., *Force chain buckling, unjamming transitions and shear banding in dense granular assemblies.* Philosophical Magazine, 2007. **87**(32): p. 4987-5016.

[36] Balevi\vc, ius, Robertas, D\vz, iugys, Algis, and Ka\vc, ianauskas, Rimantas, *Discrete element method and its application to the analysis of penetration into granular media.* Journal of Civil Engineering and Management, 2004. **10**(1): p. 3-14.

[37] Westwood, J. and others, *Simulating needle insertion and radioactive seed implantation for prostate brachytherapy.* Medicine Meets Virtual Reality 11: NextMed: Health Horizon, 2003. **94**: p. 19.

[38] Goksel, O., et al., *3D needle-tissue interaction simulation for prostate brachytherapy*, in *Medical Image Computing and Computer-Assisted Intervention--MICCAI 2005*. 2005, Springer. p. 827-834.

[39] Chentanez, N., et al., *Interactive simulation of surgical needle insertion and steering*. Vol. 28. 2009: ACM.

[40] DiMaio, S.P. and S.E. Salcudean, *Needle insertion modeling and simulation.* Robotics and Automation, IEEE Transactions on, 2003. **19**(5): p. 864-875.

[41] Schr\"o, t., Matthias, D.I. Goldman, and H.L. Swinney, *Stationary state volume fluctuations in a granular medium.* Physical Review E, 2005. **71**(3): p. 030301.

[42] Nowak, E.R., et al., *Density fluctuations in vibrated granular materials.* Physical Review E, 1998. **57**(2): p. 1971.

[43] Tsai, J.-C., G.A. Voth, and J.P. Gollub, *Internal granular dynamics, shear-induced crystallization, and compaction steps.* Physical review letters, 2003. **91**(6): p. 064301.

[44] Daniels, K.E. and R.P. Behringer, *Hysteresis and competition between disorder and crystallization in sheared and vibrated granular flow.* Physical review letters, 2005. **94**(16): p. 168001.

[45] Schr\"o, t., Matthias, et al., *Phase transition in a static granular system.* EPL (Europhysics Letters), 2007. **78**(4): p. 44004.

[46] Stone, M.B., et al., *Local jamming via penetration of a granular medium.* Physical Review E, 2004. **70**(4): p. 041301.

[47] Toiya, M., J. Hettinga, and W. Losert, *3D imaging of particle motion during penetrometer testing.* Granular Matter, 2007. **9**(5): p. 323-329.

[48] Albert, R., et al., *Slow drag in a granular medium.* Physical review letters, 1999. **82**(1): p. 205.

[49] Voivret, C., et al., *Space-filling properties of polydisperse granular media.* Physical Review E, 2007. **76**(2): p. 021301.

[50] Hetenyi, M., *Beams on elastic foundation: theory with applications in the fields of civil and mechanical engineering*. 1971: University of Michigan.

3 Friction of Extensible Strips: An Extended Shear Lag Model with Experimental Evaluation

Ahmad R. Mojdehi[1], Douglas P. Holmes[2], David A. Dillard[1]

[1]Department of Biomedical Engineering and Mechanics, Virginia Tech, Blacksburg, VA 24061, USA

[2]Department of Mechanical Engineering, Boston University, Boston, MA, 02215, USA

(Mojdehi, Ahmad R., Douglas P. Holmes, and David A. Dillard. "Friction of extensible strips: An extended shear lag model with experimental evaluation." *International Journal of Solids and Structures* 124 (2017): 125-134.)

3.1 Introduction

Friction is ubiquitous in daily life, playing an important and often essential role in many natural processes as well as engineered technologies such as tires, brakes, rubber seals, conveyer belts, and footwear. The coefficient of friction (COF) of a pair of materials has often been considered as a constant, according to Coulomb's friction law. However, more detailed studies have shown that the COF of a pair of materials depends on roughness [1-3], normal load [4-8], sliding velocity, and temperature [9-12]. Recently, soft and extensible materials have been used in state-of-the-art technologies such as wearable sensors [13-16] and stretchable electronics [17-21], in which the materials can deform under relatively small amounts of load, owing to a high effective compliance resulting from either low modulus or geometric design. Understanding the role of effective axial compliance on the frictional properties of materials, from both experimental and theoretical points of view, has important implications for such technologies. This paper presents a comprehensive study that combines theory and experiments to investigate how the frictional responses of a system, *i.e.* static and kinetic frictions, depend on the effective axial compliance, and is believed to have numerous practical applications.

Friction between an extensible strip and a substrate has some analogy with a lap shear adhesive joint, where in the former, the axial load is transferred between the strip and substrate via frictional stresses and between the two adherends by shear stresses in the adhesive layer for the latter. The shear lag model introduced by Volkersen [22] and its various refinements have been widely used in the analysis and design of adhesive joints. In the shear lag model, adherend extensibility can significantly affect the resulting shear stress distribution in an adhesive layer. This model has been

extended for analysis of elastic-plastic adhesives [23], fiber-matrix interactions in composite materials [24], and interfacial friction stress at a frictionally bonded fiber-matrix interface in single fiber push-out tests [25]. Several papers report investigations of the role of effective axial compliance, *i.e.* effective compliance in the direction of applied load, on the shear adhesion of extensible materials. For example, Bartlett *et al.* [26] investigated the effect of backing compliance on the shear adhesion strength of fabric-backed elastomers, and proposed a scaling relationship between adhesive force capacity, projected area of contact, and effective axial compliance of the fabric-backed elastomer in shear loading. They showed that by decreasing the compliance of the backing fabric, the shear adhesion strength of the elastomer increases, obeying scaling laws valid over a broad range of systems. In another paper, Bartlett *et al.* [27] derived a relationship for the compliance of the elastomeric adhesive system, considering multiple deformation modes such as bending, shear deformation, and tensile elongation, combining them through superposition. However, since the shear lag model was not considered in the tensile mode compliance, a uniform distribution of shear stress at the elastomer to substrate interface along the length of the sample was assumed. This assumption may be problematic, especially for the adhesive strips longer than the characteristic shear lag length. More recently, Ponce *et al.* [28] studied the effect of axial compliance and bond area on the shear adhesion strength of elastomeric strips. They found that by increasing the length of strip adhered to the substrate, there is a transition from catastrophic debonding, where the scaling law derived by Bartlett *et al.* [26] is applicable, to a regime dominated by friction, resulting in steady detachment in which the above mentioned scaling law is no longer applicable. They observed the transition to occur at a length equal to twice the characteristic shear lag length.

Friction of elastomeric materials, as a sub-category of soft materials, has been widely studied for decades because of their many desirable attributes and extensive engineering uses [4-12]. Generally, the friction force required to slide a viscoelastic material across a surface is expressed as the summation of adhesion friction and hysteresis friction [9, 29, 30]. The former is more dominant on smooth substrates and is directly related to the contact area, while the latter is more significant on rough surfaces, giving rise to bulk viscoelastic energy dissipation within the material [9, 12]. Several papers have theoretically modeled frictional behavior of polymers using a correlation between viscoelastic properties, adhesion, and friction [31-33]. However, the role of effective axial compliance on the frictional response of elastomeric materials is not well

understood. Lorenz and Persson investigated the effect of system compliance on the static friction of solids, showing that in a sufficiently soft solid the static friction can be reduced to the kinetic friction due to the occurrence of sequential interfacial slip [34]. Studies on the transition from static to kinetic friction and stick-slip behavior also showed local slippage, called "precursors", well before the onset of global sliding, depending on the geometry and compliance of the system and loading conditions [35-39]. Thornton *et al.* [40] included radial compliance based on elastomer shear in their theoretical model to calculate the interfacial stress for elastomeric disks in compression, predicting slippage of the disk at radiuses greater than a critical radius. The effect of axial compliance on the performance of rubber belt drives has been studied, showing a slippage zone on the driving pulley due to stretching of the belt resulting from tension [41-43].

In this paper, we studied the role of effective axial compliance on the friction of extensible strips, from both experimental and theoretical points of view. The changes in the static and kinetic friction forces with respect to the effective axial compliance are investigated and compared with control friction response, which is defined as the friction response of an axially rigid strip against the substrate of interest. We found three regions, *i.e.* no-slip, transition, and slip zones along the length of strips. Based on the experimental results, a theoretical model, adopted from the elastic-plastic extension of the classical shear lag model, is proposed to predict the friction response as a function of effective axial compliance. Using longitudinal force equilibrium, the governing equations corresponding to the different regions, *e.g.* no-slip, transition, and slip, along the length of the strip are derived. Force-displacement response of strips with different compliances are predicted using the theoretical model developed. The results obtained from the extension of shear lag analysis are compared with experimental results obtained herein and shown to be in good agreement.

3.2 Experiments

In order to measure the friction of extensible strips, a dead weight (sled) is used to apply normal load on the top of the strip. This does induce a secondary frictional interface between upper surface of the strip and the sled, a complication that is also addressed in the model, making it general enough to apply to cases with or without a sled. The friction-displacement measurements were performed using a custom-built friction setup (Figure 3-1a): a translational actuator (PI,M-229.26S, Karlsruhe, Germany) pulled a steel sled (mass 190 g, length 100 mm, and width 10 mm), the rounded nose of which secured the end of the strip, across a glass substrate. The control friction

response between the bottom surface of the strip and substrate was obtained by adhering the strip's top surface (using Gorilla Super Glue, The Gorilla Glue Company, Cincinnati, Ohio, US) to the sled and pulling it across the substrate (Figure 3-1b), whereas the control friction response between the top surface of the strip and the sled was determined by pulling the sled on top of the strip while the strip's bottom surface was bonded (using Gorilla Super Glue, The Gorilla Glue Company, Cincinnati, Ohio, US) to the substrate. For the friction-displacement response of the extensible strips, the strip was only bonded to the front edge of the sled, thereby permitting slippage and relative motion between sample and sled as the strip stretched. Two different materials, *e.g.* elastomer-coated fabric strips (Jo-Ann Fabric and Crafts, product number: 13421664) and braided elastic bands (Jo-Ann Fabric and Crafts, product number: 07705148a) were used in order to have different frictional interfaces and also sufficient extensibility. Due to anisotropy of the fabric, two different backing compliances were obtained by cutting the strips from the elastomer-coated fabric in the machine direction and perpendicular to the machine direction. Moreover, the effective axial compliance (i.e. *L/EA* that will be discussed in the Theoretical section) was varied by changing the length of the strips; four strip lengths were chosen between 40 mm and 100 mm. The total friction force was measured using a load cell with a full range of 5.9N (OMEGA, LCAE-600G, Stamford, CT, USA). The load train compliance (i.e. load cell, connection wire, and clamp) was obtained (0.1 mm/N) by clamping the sled on the substrate and measuring the force-displacement response of the system. All the experimental results were corrected based on the obtained load train compliance. For the case of symmetric friction on both sides of the strip, adhesive tapes (3M, Scotch-600, St. Paul, MN, USA) were applied on the steel sled and glass substrate. The same method was used to measure the control friction response of these pairs of materials. The effective axial compliance of the strips was measured by conducting uniaxial tensile tests on strips of the materials, using the same actuator and load cell. A camera (Nikon D7000), viewing from the side, was used to capture the localized displacements (as functions of time) of several points marked along the length of the samples and relative motion of the sled with respect to the strip. The displacements of marked points were measured by tracking the positions of color markers in each frame with respect to the background (reference) frame. Then the positions, in terms of pixel unit, were converted to the millimeter unit using a calibration factor obtained from measuring the

number of pixel per unit millimeter. The experiments were conducted at a displacement rate of 2.5 mm/sec, and the results represent the means of triplicate experiments.

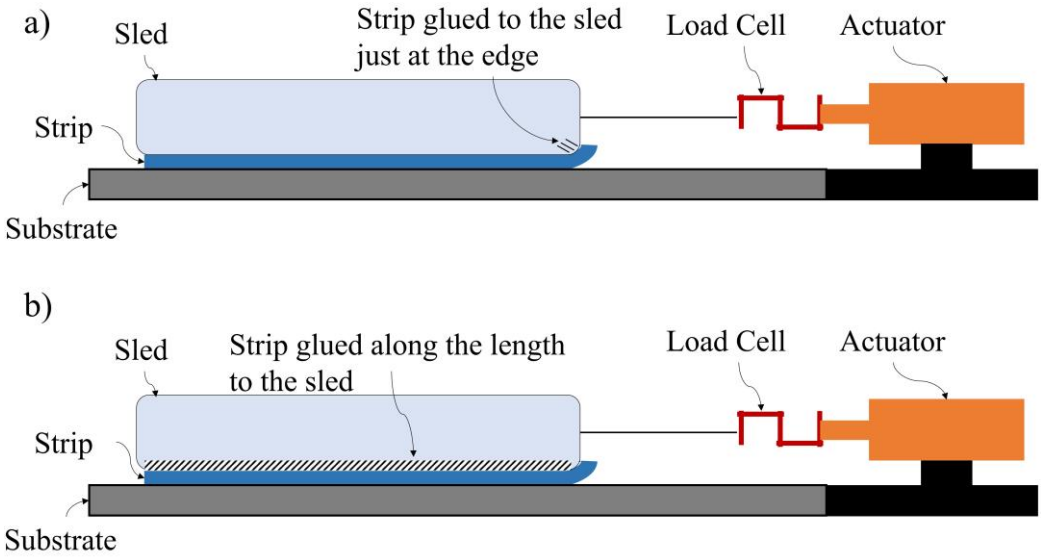

Figure 3-1. Schematic of experimental setup a) Friction experiment of extensible strips, and b) Control friction experiment

3.3 Theoretical model

A shear lag model is used as the basis to predict the effect of axial compliance on the friction of extensible strips. The goal is to develop a simple theoretical model to obtain better insights into the effects of system compliance on the friction response of extensible strips. The model's development was inspired by Hart-Smith's [23] extension of Volkersen's elastic shear lag model [22] for adhesively bonded lap joints to include adhesive plasticity. The friction response of the extensible strip is analogous to the rigid-perfectly plastic response of adhesives in lap joint shear loading. In particular, the stresses up to the static friction stress are analogous to the rigid adhesive response, while the kinetic friction stress is analogous to yielding and plastic shear stress in the adhesive layer. However, in the friction stress versus displacement response of most materials, there is a drop from static peak to the kinetic friction that is considered as a transition region, whereas in the adhesive layer with perfectly plastic response there is a plateau after yielding in the shear stress-strain curve (see Figure 3-2). It is worth noting that in classic friction (*e.g.* metals) the transition distance is very small (on the order of microns), exhibiting a nominally multi-valued

function (abrupt drop) in the transition displacement from static to kinetic friction when the displacement scale is in the order of millimeter [44].

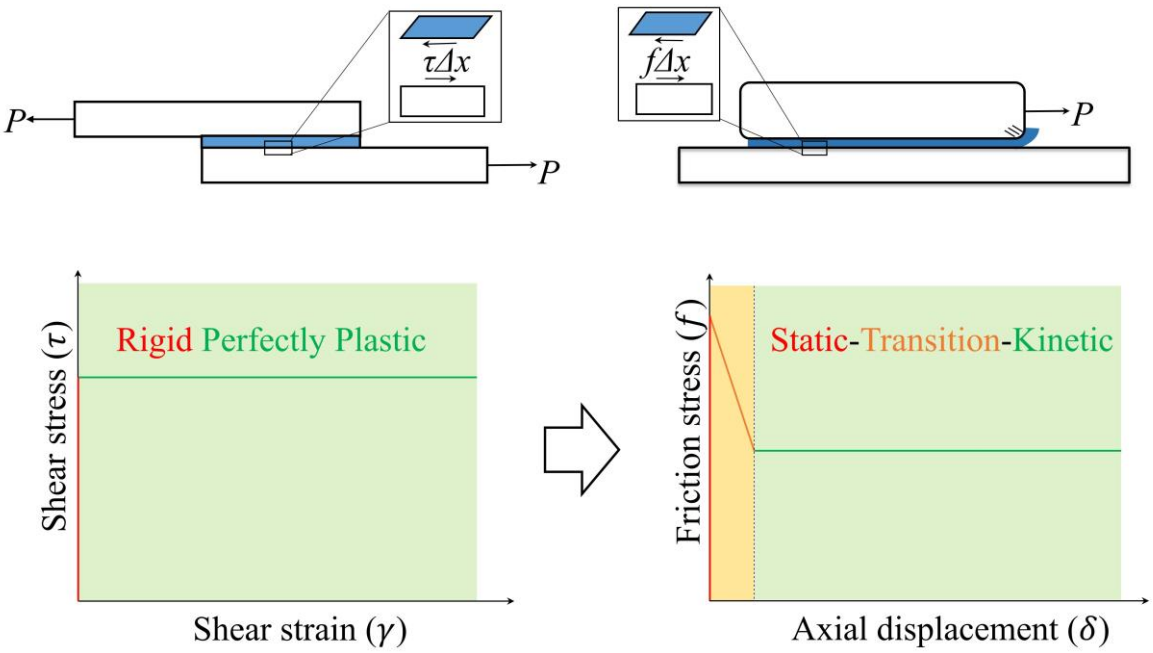

Figure 3-2. Analogy between Hart-Smith's rigid-perfectly plastic stress-strain behavior of an adhesive layer in a lap joint (left) and the friction stress versus displacement response of an extensible elastomer-coated fabric sliding on a substrate (right). Rigid response is analogous to static friction response, perfectly plastic stress is analogous to kinetic friction stress, and the drop from static to kinetic friction is defined as a transition region.

Figure 3-3a shows the geometry and free body diagram of a differential element of an extensible strip in contact with a substrate on the bottom and a sled on the top. Using longitudinal force equilibrium of the differential element dx and the stress-strain relation of the strip, the governing differential equation can be written as:

$$\frac{d^2\delta}{dx^2} + \frac{f_T(\delta) - f_B(\delta)}{Et} = 0 \tag{3.1}$$

where δ is the displacement of the strip with respect to substrate, Et is the axial stiffness of the strip (effective strip modulus times its thickness), and f_B, and f_T are the control friction stresses on the bottom and top interfaces, respectively, assuming unit width, (alternatively one may think of these as the force per unit length). We define f_B and f_T for a general case as:

$$f_B(\delta) = \begin{cases} f_{Bs} - (f_{Bs} - f_{Bk})\delta/D_B & 0 \le \delta \le D_B \\ f_{Bk} & \delta \ge D_B \end{cases} \quad (3.2)$$

$$f_T(\delta) = \begin{cases} f_{Ts} - (f_{Ts} - f_{Tk})\delta/D_T & 0 \le \delta \le D_T \\ f_{Tk} & \delta \ge D_T \end{cases} \quad (3.3)$$

Figure 3-3b and 3c depict the f_T and f_B for an elastomer-coated fabric strip with fabric-steel interface on the top (Figure 3-3b) and elastomer-glass interface on the bottom (Figure 3-3c). The corresponding constants for f_B and f_T in equations 0 and 0 can be obtained from measured curves for f_B and f_T as shown in Figure 3-3b and 3c, respectively. D_T and D_B are the limit displacements for the onset of slippage in the control friction response of the top and bottom interfaces, respectively. The finite slope observed in the transition from static to kinetic friction may originate from the shear compliance of the strips and load train compliance leading to a finite slope in transition from no-slip to slip conditions. Moreover, the ringing oscillation observed in Figure 3-3c gives rise to the effect of shear and load train compliances on the transition slope from static to kinetic friction as the wavelength of oscillation and therefore the transition slope would depend

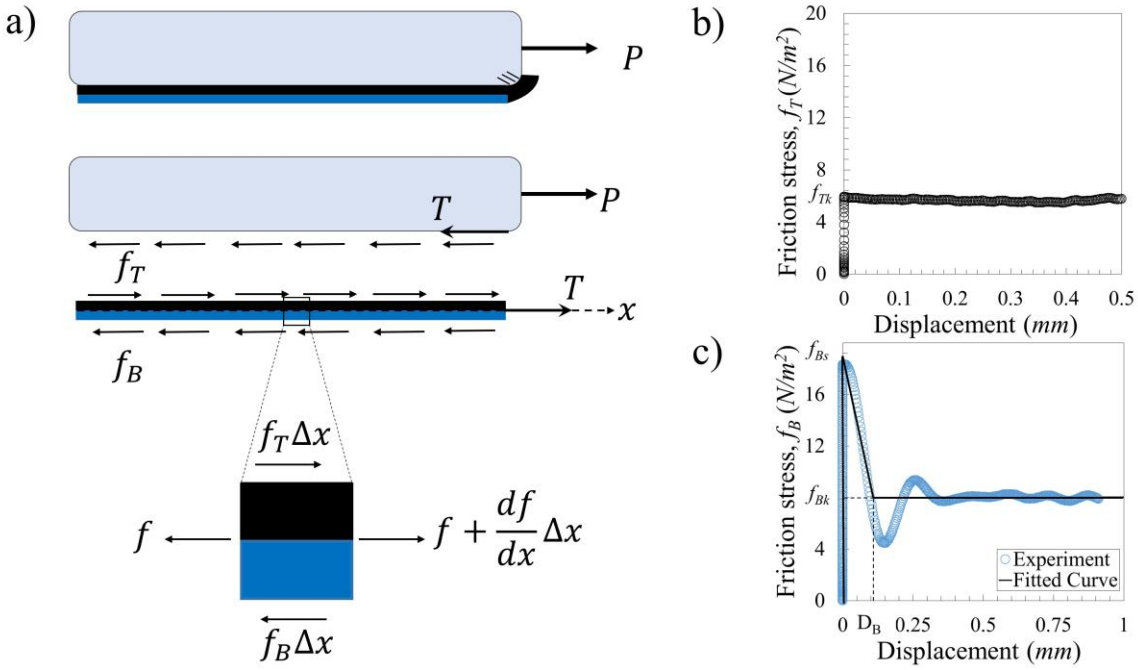

Figure 3-3. a) Free body diagram and a differential element of strip in contact with a sled and a substrate in plane stress condition. P is the external load applied to the sled, T is the internal load in the strip at $x=L$, f_T is the friction stress on the top of the strip, and f_B is the friction stress on the bottom of the strip, b) control friction stress between the sled and top surface of the elastomer-coated strip (fabric-steel interface), and c) control friction stress between the substrate and bottom surface of the elastomer-coated strip (elastomer-glass interface).

directly on the shear compliance of the bonded strip and load train compliance. Similar response was found in a model simulation performed in the literature to investigate the effect of contact compliance on the transition from static to kinetic friction [36] .

For an extensible strip, based on the control response and effective axial compliance of the strip, we can define three regions (no-slip, transition, and slip zones) with respect to the substrate and sled interface along the length of strip. These regions originate from the displacement gradient along the length of the strip by stretching due to the applied load within the strip. The size of transition region depends on several factors such as axial and shear compliance of the strip, load train compliance, and contact pressure distribution along the length of strip. For a general case where there is a transition region in both f_B and f_T, we will have a combination of six regions (no-slip, transition, and slippage for top and bottom interfaces) along the length of the strip. Figure 3-4 demonstrates a schematic image of the mentioned regions along the length of the strip. Depending on the relative magnitude of the friction forces on the top and bottom interfaces, and axial compliance of the strip, slippage on the strip's top surface may occur first or together with slippage along the bottom of the strip. By substituting equations (3.2) and (3.3) into equation (3.1), the corresponding differential equations for displacement of each region can be obtained. Finally, by using the general solution for the obtained differential equations, and satisfying the boundary and compatibility conditions below, based on equilibrium, constitutive, and continuity of displacements and stresses equations, the displacement and friction force can be numerically determined.

Equilibrium equation:

$$\int_0^L (f_B(\delta) - f_T(\delta))dx = T \tag{3.4a}$$

$$\int_0^L f_T(\delta)dx + T = P \tag{3.4b}$$

Constitutive equation:

$$\frac{d\delta}{dx} = \frac{T}{Et} \qquad at \quad x = L \tag{3.5}$$

Continuity equations:

$$\delta_{Bn} = \delta_{Bt} = 0 \qquad at \qquad x = L_{Bn} \tag{3.6a}$$

$$\delta_{Bt} = \delta_{Bs} = D_B \qquad at \qquad x = L_{Bn} + L_{Bt} \tag{3.6b}$$

$$\frac{d\delta_{Bt}}{dx} = \frac{d\delta_{Bs}}{dx} \qquad at \qquad x = L_{Bn} + L_{Bt} \tag{3.7}$$

$$\delta_{Tn} = \delta_{Tt} = 0 \quad at \qquad x = L_{Ts} + L_{Tt} \tag{3.8a}$$

$$\delta_{Tt} = \delta_{Ts} = \delta(L) - D_T \quad at \qquad x = L_{Ts} \tag{3.8b}$$

$$\frac{d\delta_{Ts}}{dx} = \frac{d\delta_{Ts}}{dx} \qquad at \qquad x = L_{Ts} \tag{3.9}$$

Subscripts *B*, *T*, *n*, *t*, and *s* correspond to the bottom interface, top interface, no-slip zone, transition zone, and slip zone, respectively.

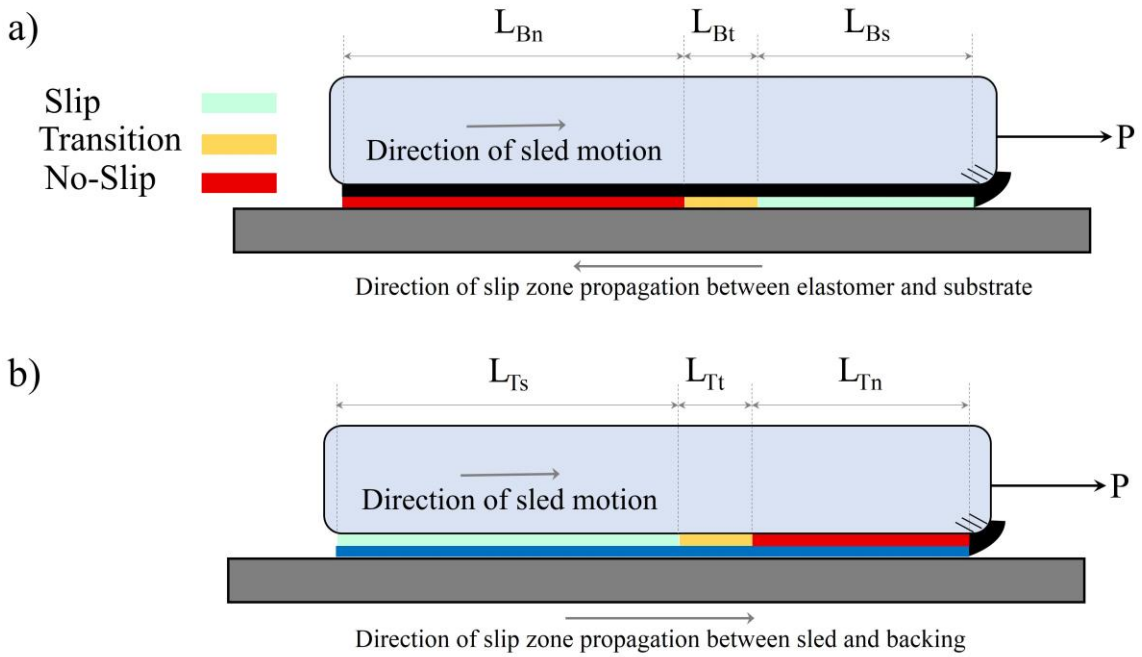

Figure 3-4. Schematic of different regions, direction of sled motion, and direction of slip zone propagation a) between bottom interface, and b) between top interface, along the length of the extensible strip.

Although friction at both top and bottom interfaces are considered in the analysis above, one can easily consider the case of a strip without a sled, which has applications to adhesive systems [26], by assuming the friction at the top (f_T) is zero.

3.4 Results and Discussion

First, the local deformation of marked points along the length of the strip was captured by a video camera and analyzed using image processing. Figure 3-5 shows the position and displacement of eight points equally spaced along the length of an elastomer-coated fabric as a function of sled displacement, as well as image sequences of development of three regions along the length of strip. The displacement of each point with respect to the substrate was obtained from image analysis of the friction experiment. The first point was at the leading edge, and the eight points were equally spaced 10 mm apart, as indicated in the inset in Figure 3-5a. The first point moved almost simultaneously with the sled, while the others were delayed until the slip zone reached each successive point, as shown in Figure 3-5a. The onset of total slippage occurred when the last point started to move, *i.e.* the moment at which point-8 (located at the end of strip) had a rise in displacement as a function of sled displacement, and occurred after 3mm of sled displacement, indicating 3mm stretching of the strip before total slippage. The progressive development of the slippage zone between elastomer and substrate along the length is also obvious in the displacements of the points from the beginning to the end of the sample. Furthermore, there is a change in the slope of the curves, which was determined from the intersection of least-square fits

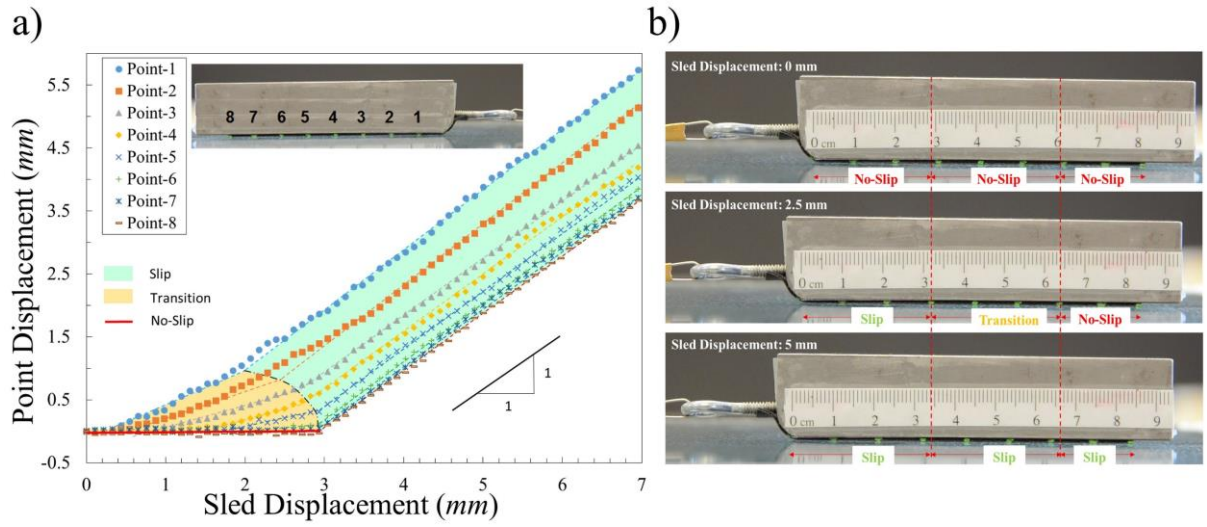

Figure 3-5. a) Displacement of different points along the length of strip. The least-square fits (dash lines) confirm the formation of transition and slip zones. Solid red line, yellow area, and green area correspond to the no slip region, transition region, and slip region, respectively. The black dash-dot line refers to the border between transition and slip regions, and b) Image sequence of development of the three regions along the length of the strip at three sled displacement values, namely 0, 2.5, and 5 mm.

of the two regions for each point. This change in slope corresponds to the transition region between no-slip and slippage zones, as indicated in Figure 3-5a. The sequence of development of the three regions along the length of the strip, showing different regions at three sled displacement values, are presented in Figure 3-5b.

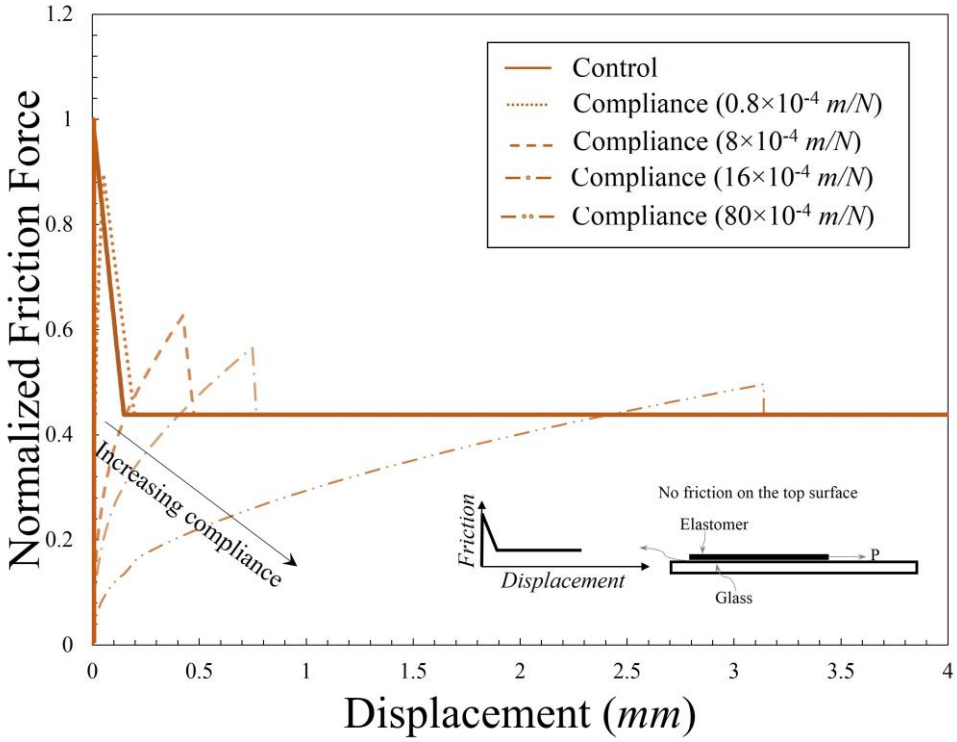

Figure 3-6. Normalized force versus displacement curve obtained from theoretical model for the case with no friction on the top interface for different values of compliance. The friction force is normalized by the peak in control friction force.

In presenting theoretical results, we start with the simplest case involving no sled, *i.e.* frictional forces exist only at the bottom interface where the strip is in contact with the substrate (f_T=0). This corresponds to the case where friction arises due to the weight of strip itself, which is conceptually easier to consider but more difficult to implement experimentally. Moreover, it has some application to the adhesives (e.g. pressure sensitive adhesives) where the adhesive's modulus is sufficiently low so that no normal load is needed to establish the friction/adhesion force. Figure 3-6 illustrates the force-displacement response obtained from the shear lag model for an extensible strip sliding on a glass substrate. The same control friction between the elastomer and glass for the elastomer-coated fabric shown in Figure 3-3c was used in this model. By increasing the effective axial compliance of the strip, the peak corresponding to the static friction force decreases

dramatically, transitioning into a slope change rather than a peak for the onset of slippage at the leading edge of the strip. After the onset of the slippage, the slip zone propagates along the length of the strip leading to stretching and therefore storing the elastic energy in the strip that results in an increase in the kinetic friction force. However, the kinetic friction would go back to the control kinetic friction after slippage of the entire strip as the internal force vanishes due to no progressive stretching.

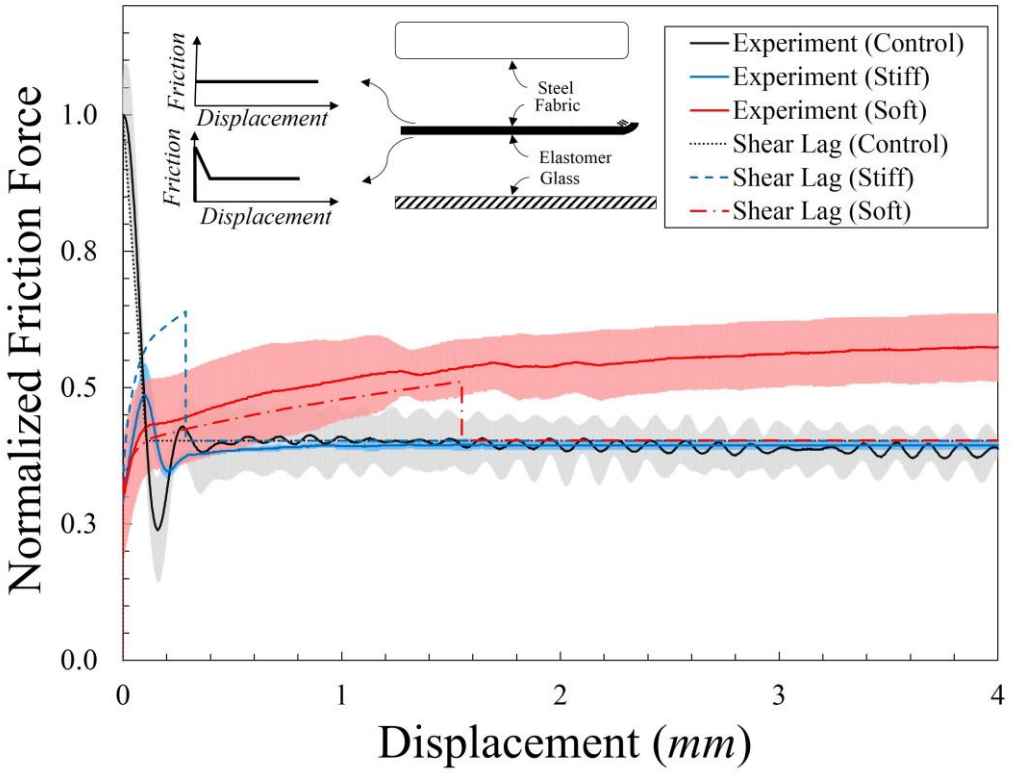

Figure 3-7. Normalized friction force versus sled displacement curve of elastomer-coated fabric strips with three different backing compliances. Solid lines are the average values of three replicate experiments. Dashed lines are predictions from the theoretical model. Widths of shaded areas correspond to +/- one standard deviation of triplicate experiments. The friction force is normalized by the peak in control friction force.

Returning to the inclusion of a rigid sled and the additional interface, Figure 3-7 presents the experimental force-displacement response of elastomer-coated fabric strips with three different backing compliances, along with comparisons with the theoretical model predictions, which in this case, includes effects of two friction interfaces (upper and lower surfaces of the strips). The stiff strip was obtained by cutting the elastomer-coated fabric in the machine direction, while the soft strip was perpendicular to the machine direction. Similar trends as for the previous case, with no

friction on the strip's top surface, were observed here for both experimental and theoretical results. The stiffer strip had the higher static friction peak, whereas the more compliant strip exhibited no static friction peak. The static and kinetic friction force predictions are higher compared to the first case, as here there are now two friction interfaces resulting in a higher frictional energy dissipation in the system. However, after slippage of the entire strip, the theoretical model predicts the kinetic friction should drop to the control kinetic friction for both cases (with and without upper frictional interface).

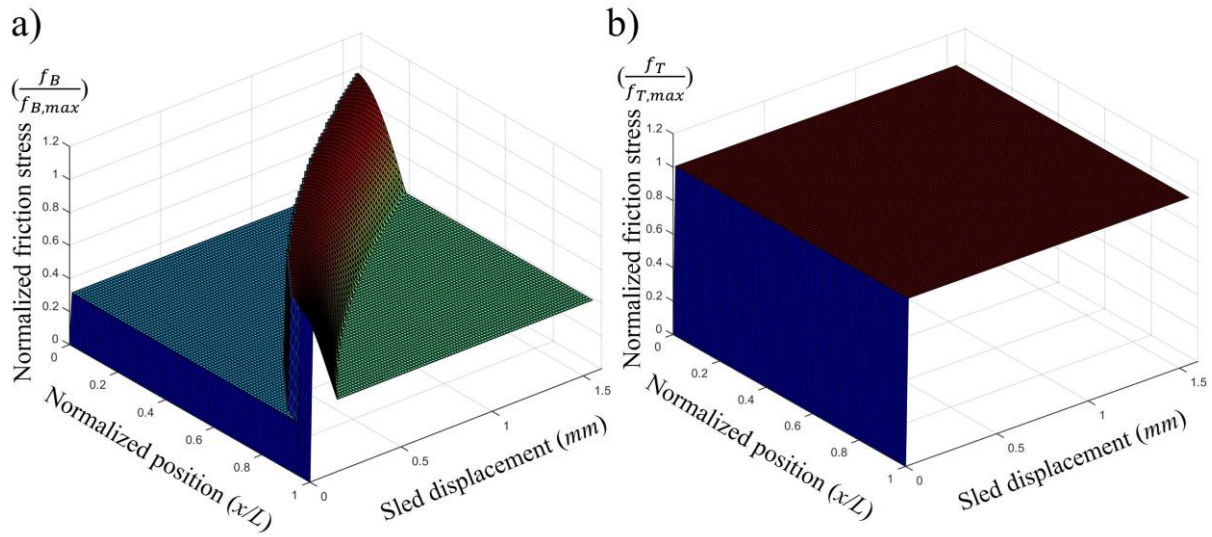

Figure 3-8. Normalized friction stress as function of normalized position and sled displacement on a) bottom interface, and b) top interface. The friction stress is normalized by the peak in control friction stress corresponding to each interface. The position is normalized by the length of the strip.

The trend found for the static friction here is consistent with that found in the literature for the effect of elasticity on the static friction of sliding system [34] and shear force capacity of elastomer adhesion [26, 27]. In our friction experiments, the elastomer with the more flexible backing experienced a larger range of deformation from the leading edge to the end, resulting in a combination of static and kinetic friction along the length of the strip and softening the static peak of the entire strip due to an averaging of the local static and kinetic friction forces. On the other hand, in the stiffer backing case, there was no noticeable change in the deformation along the length due to the stiffness of the backing, which enabled nominally all the contact points to move together, resulting in either static or kinetic friction along the length of the sample. This resulted in a sharp peak in static friction and a rather sharp drop to kinetic friction after slippage. However,

for any system with finite stiffness we should expect some order of deformation, although the deformation and its effect on the friction may not be noticeable, depending on the resolution of the experimental setup. The shear lag model was able to predict this behavior fairly well. The model predicted the initiation of slippage, where there is a slope change in the curve, as well as the displacement at which the slippage of the entire strip occurred.

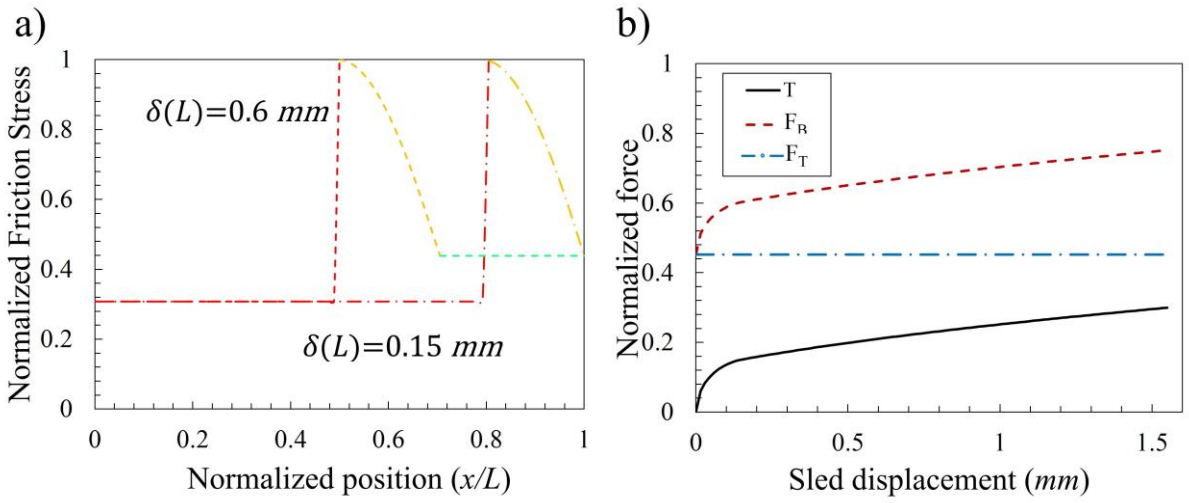

Figure 3-9. a) Friction stress distribution along the length of elastomer-coated strip for two sled displacements, including one region (no-slip) for the load before initiation of the slip and three regions (no-slip, transition, and slip) for the load after slip initiation, and b) normalized friction force on the top (F_T) and bottom (F_B) interfaces and the internal force (T) in the soft extensible strip at $x=L$ with respect to the sled displacement. The friction stress is normalized by the peak in control friction stress. The forces are normalized by the peak in control friction force.

In order to show how the friction stress on the top and bottom interfaces change along the length of the strip when the sled is pulled, we plotted the theoretical normalized friction stress on two interfaces in three dimensional figures with respect to the sled displacement and the normalized position along the length of the strip (see Figure 3-8a and Figure 3-8b). By increasing the sled displacement the slippage on the top interface propagates first (since $f_{Ts} < f_{Bs}$ for the elastomer-coated fabric strip) following to the propagation of transient (downward slope in the Figure 3-8a) and slip (right flat surface in the Figure 3-8a) regions along the bottom interface. The slip regions increase in size while the no-slip region size decreases up to the slippage of entire strip on the bottom interface. Since there was no transition region on the top interface's control response, there would be only slip region on the top interface after sled displacement.

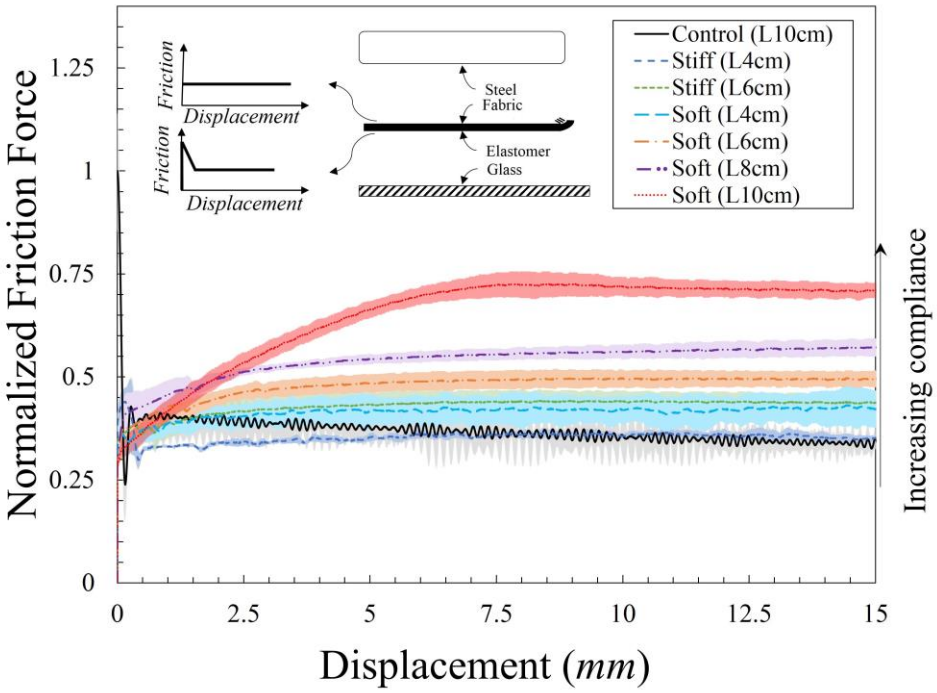

Figure 3-10. Force versus displacement curve of elastomer-coated fabric strips with different effective compliances by changing the length. Solid lines are the average values of three replicate experiments. Widths of shaded areas correspond to +/- one standard deviation of triplicate experiments. The friction force is normalized by the peak in control friction force.

Figure 3-9a shows friction stress distribution along the lower interface of the elastomer-coated strip obtained from Figure 3-8a for two representative sled displacement values: when there is only no-slip and transition regions along the length of the strip ($\delta_{sled} = 0.15\,mm$) and also when a combination of three regions exist at the bottom interface ($\delta_{sled} = 0.6\,mm$). In $\delta_{sled} = 0.6\,mm$ curve, the plateau value on the right corresponds to the slip zone, the rise from plateau to the max force is associated with the transition region, and the drop from max load to a secondary plateau is related to the no-slip zone where the friction stress level corresponds to the stress reaction on the top interface for the system to be in equilibrium. This curve is similar to the shear stress distribution in a single lap adhesive joint, considering rigid-perfectly plastic constitutive model for the adhesive. However, there is no rise in the shear stress distribution of the adhesive layer due to the transition as seen in the friction stress distribution of the elastomer-coated strip. Moreover, the changes in the internal force at the point where the strip is bonded to the sled (T) and friction forces on the top (F_T) and bottom (F_B) interfaces (obtained from integration of the friction stress along the length of the strip) are plotted as a function of sled displacement in Figure 3-9b. As shown in

equations (3.4a) and (3.4b), the external force measured at the sled leading edge (P) is equal to the summation of F_T and T, or equivalently F_B.

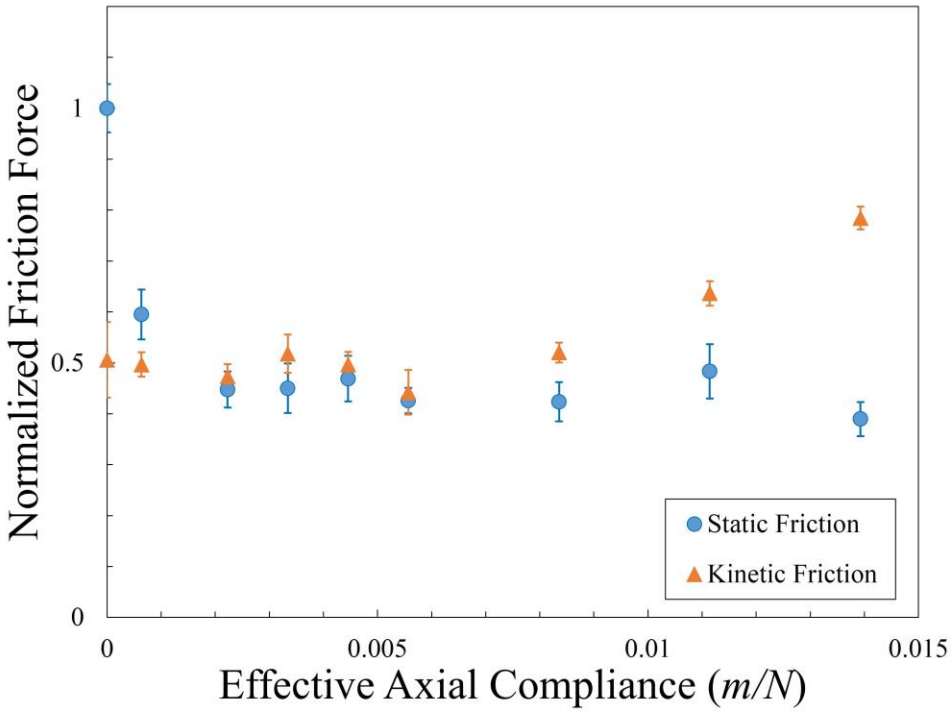

Figure 3-11. Normalized static and kinetic friction forces versus effective axial compliance for elastomer-coated fabric strips. The effective axial compliance was changed by changing the length and fabric backing orientation. Error bars indicate +/- one standard deviation of triplicate experiments. The friction force is normalized by the peak in control friction force for the respective length.

The effective axial compliance of a given strip material can be varied by changing the length of the strips (*i.e.* changing *L* in *L/EA*); results are illustrated in Figure 3-10. Again, similar trends are observed as seen with different backing compliances, as increasing the length increased the effective compliance of the strips. Although the contact area would change upon changing the length of the strip, making it difficult to compare the friction response of strips with different lengths, the friction force for each specific length is normalized by the corresponding peak associated with the control friction response of the strip with that length. Moreover, the overturning moment, applied to the sled due to the vertical eccentricity between the point where the external load is applied and the substrate on the bottom, would disrupt the uniform normal load distribution on the strip. The overturning moment, referred to as "friction-induced torque" in the literature, was found to have a major effect on the normal pressure distribution depending on the geometry of the

sample [45, 46]. In addition, the thickness of the strip would change due to the Poisson's effect disrupting the uniform normal load distribution on the strip. Therefore, because of the mentioned complications, *i.e.* change in contact area, friction-induced torque, and Poisson's effect, the theoretical model is not compared with the experimental results for the cases where the length was changed.

Figure 3-11 summarizes the change in static and kinetic friction forces with effective axial compliance of the strips for elastomer-coated fabrics arising from different lengths and backing orientations. The decrease in static friction peak and increase in kinetic friction plateau force with increasing effective axial compliance are seen in this figure. A plateau in the static friction force is observed at high compliance, while a plateau in kinetic friction force is suggested at low values of compliance. The plateau in kinetic friction at low values of compliance is due to the lower extensibility of the strips, leading the kinetic friction to approach the control response for the strip adhered along the full length of the sled. For the compliant strips, since there was no distinct peak corresponding to the static friction as shown in Figure 3-7 and Figure 3-10, the static friction was obtained from the point where slippage initiates. The lowest force at which this change could happen would be the force corresponding to the control kinetic friction that limit the decrease in static friction with compliance of the strip, resulting in a plateau in static friction at higher values of compliance. The mentioned justification for the plateaus of static and kinetic friction forces with compliance is supported by Figure 3-11, where both plateaus occurred at almost the same value of friction force, *i.e.* the control kinetic friction.

However, the kinetic friction force did not drop to the control friction force for the softest elastomer-coated fabric after slippage of the entire sample, resulting in a permanent increase in the kinetic friction force. This condition could result from stick-slip behavior along the length of the strip that is reminiscent of Schallamach waves [47-51], resulting in an oscillatory slippage on the top interface. This condition leads to the contribution of the top interface's friction force to the total friction force even after slippage of the entire sample, resulting in a permanent increase in the kinetic friction force of the extensible strips. The stick-slip response requires the static friction force to be higher than the kinetic friction force, and it is also very sensitive to the compliance of the system [52].

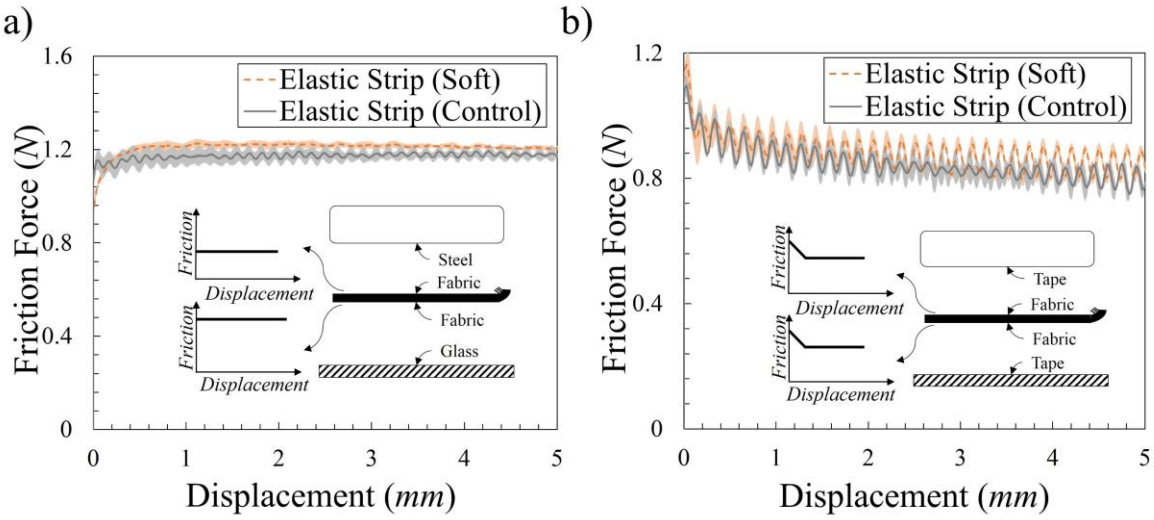

Figure 3-12. Force versus displacement curve of braided elastic strips a) in contact with steel on the top and glass on the bottom, and b) in contact with tape on the top and bottom.

To verify this assumption of an increase in kinetic friction, we performed the same experiment with braided elastic strips, where the control static and kinetic frictions are almost identical. Figure 3-12a shows the control friction response of the braided elastic strip and the response for flexible case in contact with steel on the top and glass on the bottom. It is clear that although the static friction softened for the soft strip compared to the control response, the kinetic friction force is almost the same for two cases, showing the possibility of stick-slip response in the soft elastomer-coated fabric strips that resulted in an increase in the kinetic friction force.

Furthermore, a symmetric case where the friction at the top and bottom interfaces were nominally identical was examined. For this purpose, we used the braided elastic strip where the top and bottom materials are the same (fabric). Adhesive tapes are bonded to the sled and the substrate to have fabric-tape interface on the both top and bottom interfaces of the strip (symmetric friction). As expected from the symmetry and the equilibrium condition on the strip, friction on the top and bottom interfaces are nominally identical, and there should be no relative motion between the sled and the strip, resulting in movement of the sled and strip together. This circumstance is analogous to the control friction response (*e.g.* sled glued to the entire length of the strip) where there is no relative motion between sled and the strip. Therefore, the friction response of soft strips would be nominally identical to the control friction response of the strips, as shown in Figure 3-12b.

In addition, although the complex dynamic response of the system including the effects of sled mass, system compliance, and two frictional interfaces on the top and bottom requires a comprehensive analysis of the system's dynamics, we simply implemented a mass-spring model using the sled mass and system compliance to interpret the oscillations found in the control and extensible strips and their effects on the increase in kinetic friction of extensible strips. A long wavelength oscillation is seen in the displacement of the points on elastomer-coated fabric strip close to the leading edge of the sled in the slip zone in Figure 3-5a. A Fast Fourier Transform (FFT) analysis is performed to quantify the frequency of the oscillation, showing a distinct peak at 1.25 Hz. This frequency is more than an order of magnitude smaller than the frequency of oscillation found in the kinetic plateau of the control friction response of elastomer-coated fabric strip (17.5 Hz), as seen in Figure 3-7. The decrease in stick-slip frequency could be attributed to the increase in compliance from the control friction response where the shear and load train compliances are dominant to the extensible strip where the axial compliance is dominant (for the soft elastomer-coated fabric the ratio of effective axial compliance to shear compliance calculated to be 70). Considering the inverse square root relationship between frequency and compliance, and also damping effects from viscoelasticity and friction, this reduction in the frequency of stick-slip seems reasonable. In addition, the magnitude of the peak in FFT analysis reduces as the point is farther from the leading edge showing that the oscillation mostly corresponds to the sled since the strip is bonded to the leading edge of the sled. Therefore, the oscillatory response of the sled gives rise to the contribution of the top interface's friction force to the total friction force even after slippage of the entire sample, resulting in a permanent increase in the kinetic friction force of the extensible strips.

A temporary increase in the kinetic friction force in the more flexible strip can possibly be justified by the stored elastic energy due to the extension of the strip along the slip and transition regions, considering the no-slip region at the interface between the elastomer and substrate as a boundary condition gripping the end of the strip. This condition is analogous to pulling a spring (with a spring constant equal to the stiffness of a strip and a length equal to slip plus transition region in size) in a displacement-control condition. By propagating the slip and transition regions along the length of the strip, the mentioned spring constant decreases gradually due to the increasing length of the slip and transition regions, resulting in a decrease and finally a plateau in the force-displacement curve. Although the elastic stretching of the strip is maintained after slippage of the

entire sample, as seen in Figure 3-5a, showing that the stored elastic energy did not release, but in some replicate experiments a small drop in the friction force found right at the slippage of the entire strip. For the case of the braided elastic strip, as there is no distinct no-slip region along the length of the strip, (*i.e.* there is no distinct static peak in the control friction response), the strip does not have any support (*i.e.* no-slip region) at the end, leading to the slippage of the entire sample together. However, there would be a small amount of extension in the strip due to a balance between distributed friction stress along the length of the strip and the applied external load, resulting in a softening of static to kinetic friction transition and also a small increase in the kinetic friction plateau, as shown in Figure 3-12a. Overall, it seems that the stick-slip behavior on the bottom interface resulting in an oscillatory slippage on the top interface would be, more likely, the main mechanism for the permanent increase in the kinetic friction force of soft extensible strips after the slippage of the entire sample. This mechanism could be used in the systems where the kinetic friction plays an important role. For example, a multi-layer system may be implemented in the car brake such that the kinetic friction increases during braking resulting in a shorter braking distance. However, a more in-depth study of the permanent increase in the kinetic friction is necessary, which is beyond the scope of the present work.

3.5 Conclusion

The role of effective axial compliance on the frictional response of extensible strips was investigated, both experimentally and theoretically. A translational actuator pulled a steel sled, the rounded nose of which secured the end of the strip, across a glass substrate. We found that the effective axial compliance of the strip has a profound effect on the static and kinetic friction of extensible strips. In particular, by increasing the effective axial compliance of a strip, the peak corresponding to the static friction force decreased dramatically, which was consistent with the literature data for adhesion of elastomer-coated fabrics. For sufficiently compliant strips, there was no observable static friction peak, while the kinetic friction force increased significantly. A possible mechanism for the permanent increase in the kinetic friction could be the stick-slip behavior on the bottom interface giving rise to the oscillatory slippage on the top interface, thereby resulting in an additional frictional interface playing a role even after slippage of the entire strip. Several strip-substrate interface contact materials were used to evaluate the effect of different control friction responses on the friction of extensible strips. The local displacements of the several points along the strip's length were analyzed using image processing and the development of a

local slippage zone at the interface with the substrate was observed. Furthermore, a new extension of the classical shear lag model is proposed to predict the effect of compliance on the friction force of extensible strips. Three regions are defined along the length of elastomer, namely no-slip, transition, and slip zones. The results obtained from the shear lag analysis are compared with experimental results and shown to be in good agreement. Interestingly, the analysis resembles that obtained when shear lag theory is applied to lap shear joints experiencing adhesive layer plasticity at the end. The results obtained from this study could give more insight for design and optimization of systems where the static and kinetic friction forces play an important role, such as tires, footwear, and wearable sensors, by tuning the compliance of the system and therefore the static and kinetic friction forces, depending on the application and significance of each friction force.

Acknowledgments

The authors gratefully acknowledge Prof. Timothy E. Long from the Department of Chemistry and Prof. Christopher B. Williams from the Department of Mechanical Engineering and their research groups at Virginia Tech for helpful discussions. We would also like to thank the Provost's Office and College of Engineering for partial support of AM, the Biomedical Engineering and Mechanics (BEAM) Department for use of equipment, and the Macromolecules and Interfaces Institute at Virginia Tech for fostering interdisciplinary research in polymer and adhesion science. D.P.H acknowledges financial support from the NSF CAREER CMMI-1454153.

References

[1] Dai, Z., S.N. Gorb, and U. Schwarz, *Roughness-dependent friction force of the tarsal claw system in the beetle Pachnoda marginata (Coleoptera, Scarabaeidae).* Journal of Experimental Biology, 2002. **205**(16): p. 2479-2488.

[2] Tambe, N.S. and B. Bhushan, *Scale dependence of micro/nano-friction and adhesion of MEMS/NEMS materials, coatings and lubricants.* Nanotechnology, 2004. **15**(11): p. 1561.

[3] Ford, I., *Roughness effect on friction for multi-asperity contact between surfaces.* Journal of Physics D: Applied Physics, 1993. **26**(12): p. 2219.

[4] Schallamach, A., *The load dependence of rubber friction.* Proceedings of the Physical Society. Section B, 1952. **65**(9): p. 657.

[5] Smith, R.H., *Analyzing friction in the design of rubber products and their paired surfaces*. 2008: CRC press.

[6] Nguyen, D.T., et al., *Non–Amontons-Coulomb local friction law of randomly rough contact interfaces with rubber.* EPL (Europhysics Letters), 2014. **104**(6): p. 64001.

[7] Maegawa, S., F. Itoigawa, and T. Nakamura, *Effect of normal load on friction coefficient for sliding contact between rough rubber surface and rigid smooth plane.* Tribology International, 2015. **92**: p. 335-343.

[8] Carbone, G. and F. Bottiglione, *Asperity contact theories: Do they predict linearity between contact area and load?* Journal of the Mechanics and Physics of Solids, 2008. **56**(8): p. 2555-2572.

[9] Grosch, K. *The relation between the friction and visco-elastic properties of rubber*. in *Proceedings of the Royal Society of London A: Mathematical, Physical and Engineering Sciences*. 1963. The Royal Society.

[10] Persson, B., *Sliding friction: physical principles and applications*. 2013: Springer Science & Business Media.

[11] Le Gal, A., X. Yang, and M. Klüppel, *Evaluation of sliding friction and contact mechanics of elastomers based on dynamic-mechanical analysis.* The Journal of chemical physics, 2005. **123**(1): p. 014704.

[12] Moore, D.F., *The friction and lubrication of elastomers*. Vol. 9. 1972: Pergamon.

[13] Yamada, T., et al., *A stretchable carbon nanotube strain sensor for human-motion detection.* Nature nanotechnology, 2011. **6**(5): p. 296-301.

[14] Yao, S. and Y. Zhu, *Wearable multifunctional sensors using printed stretchable conductors made of silver nanowires.* Nanoscale, 2014. **6**(4): p. 2345-2352.

[15] Kramer, R.K., C. Majidi, and R.J. Wood. *Wearable tactile keypad with stretchable artificial skin*. in *Robotics and Automation (ICRA), 2011 IEEE International Conference on*. 2011. IEEE.

[16] Pantelopoulos, A. and N.G. Bourbakis, *A survey on wearable sensor-based systems for health monitoring and prognosis.* IEEE Transactions on Systems, Man, and Cybernetics, Part C (Applications and Reviews), 2010. **40**(1): p. 1-12.

[17] Rogers, J.A., T. Someya, and Y. Huang, *Materials and mechanics for stretchable electronics.* Science, 2010. **327**(5973): p. 1603-1607.

[18] Kim, D.-H., et al., *Flexible and stretchable electronics for biointegrated devices.* Annual review of biomedical engineering, 2012. **14**: p. 113-128.

[19] Wagner, S. and S. Bauer, *Materials for stretchable electronics.* Mrs Bulletin, 2012. **37**(03): p. 207-213.

[20] Li, T., et al., *Compliant thin film patterns of stiff materials as platforms for stretchable electronics.* Journal of materials research, 2005. **20**(12): p. 3274-3277.

[21] Khang, D.Y., J.A. Rogers, and H.H. Lee, *Mechanical buckling: mechanics, metrology, and stretchable electronics.* Advanced Functional Materials, 2009. **19**(10): p. 1526-1536.

[22] Volkersen, O., *Die Nietkraft Verteilung in zugbeanspruchten Nietverbindungen mit konstanten Laschenquerschnitten.* Luftfahrtforschung, 1938. **15**: p. 41-47.

[23] Hart-Smith, L., *Adhesive-bonded double-lap joints*. 1973: National Aeronautics and Space Administration.

[24] Cox, H., *The elasticity and strength of paper and other fibrous materials.* British journal of applied physics, 1952. **3**(3): p. 72.

[25] Shetty, D.K., *Shear-lag analysis of fiber push-out (indentation) tests for estimating interfacial friction stress in ceramic-matrix composites.* J. Am. Ceram. Soc, 1988. **71**(2): p. C107-C109.

[26] Bartlett, M.D., et al., *Looking Beyond Fibrillar Features to Scale Gecko-Like Adhesion.* Advanced Materials, 2012. **24**(8): p. 1078-1083.

[27] Bartlett, M.D., A.B. Croll, and A.J. Crosby, *Designing Bio-Inspired Adhesives for Shear Loading: From Simple Structures to Complex Patterns.* Advanced Functional Materials, 2012. **22**(23): p. 4985-4992.

[28] Ponce, S., J. Bico, and B. Roman, *Effect of friction on the peeling test at zero-degrees.* Soft matter, 2015. **11**(48): p. 9281-9290.

[29] Bowden, F.P. and D. Tabor, *The friction and lubrication of solids*. Vol. 1. 2001: Oxford university press.

[30] Kendall, K., *Rolling friction and adhesion between smooth solids.* Wear, 1975. **33**(2): p. 351-358.

[31] Persson, B.N., *Sliding friction: physical principles and applications*. Vol. 1. 2000: Springer Science & Business Media.

[32] Lorenz, B., et al., *Rubber friction: comparison of theory with experiment.* The European Physical Journal E, 2011. **34**(12): p. 1-11.

[33] Le Gal, A. and M. Klüppel, *Investigation and modelling of rubber stationary friction on rough surfaces.* Journal of Physics: Condensed Matter, 2008. **20**(1): p. 015007.

[34] Lorenz, B. and B. Persson, *On the origin of why static or breakloose friction is larger than kinetic friction, and how to reduce it: the role of aging, elasticity and sequential interfacial slip.* Journal of Physics: Condensed Matter, 2012. **24**(22): p. 225008.

[35] Taloni, A., et al., *Scalar model for frictional precursors dynamics.* Scientific reports, 2015. **5**.

[36] Nakano, K. and S. Maegawa, *Stick-slip in sliding systems with tangential contact compliance.* Tribology International, 2009. **42**(11): p. 1771-1780.

[37] Rubinstein, S., G. Cohen, and J. Fineberg, *Dynamics of precursors to frictional sliding.* Physical review letters, 2007. **98**(22): p. 226103.

[38] Rubinstein, S.M., G. Cohen, and J. Fineberg, *Detachment fronts and the onset of dynamic friction.* Nature, 2004. **430**(7003): p. 1005-1009.

[39] Trømborg, J., et al., *Transition from static to kinetic friction: insights from a 2D model.* Physical review letters, 2011. **107**(7): p. 074301.

[40] Thornton, J., et al., *Analysis of interfacial stresses for elastomeric disks in compression.* Polymer Engineering & Science, 1988. **28**(10): p. 655-659.

[41] Rubin, M., *An exact solution for steady motion of an extensible belt in multipulley belt drive systems.* Journal of Mechanical Design, 2000. **122**(3): p. 311-316.

[42] Bechtel, S., et al., *The stretching and slipping of belts and fibers on pulleys.* Journal of Applied mechanics, 2000. **67**(1): p. 197-206.

[43] Firbank, T., *Mechanics of the belt drive.* International Journal of Mechanical Sciences, 1970. **12**(12): p. 1053-1063.

[44] Rabinowicz, E., *The nature of the static and kinetic coefficients of friction.* Journal of applied physics, 1951. **22**(11): p. 1373-1379.

[45] Scheibert, J. and D.K. Dysthe, *Role of friction-induced torque in stick-slip motion.* EPL (Europhysics Letters), 2010. **92**(5): p. 54001.

[46] Maegawa, S., F. Itoigawa, and T. Nakamura, *A role of friction-induced torque in sliding friction of rubber materials.* Tribology International, 2016. **93**: p. 182-189.

[47] Barquins, M., *Sliding friction of rubber and Schallamach waves—a review.* Materials science and engineering, 1985. **73**: p. 45-63.

[48] Rand, C.J. and A.J. Crosby, *Insight into the periodicity of Schallamach waves in soft material friction.* Applied physics letters, 2006. **89**(26): p. 261907.

[49] Schallamach, A., *How does rubber slide?* Wear, 1971. **17**(4): p. 301-312.

[50] Viswanathan, K., A. Mahato, and S. Chandrasekar, *Nucleation and propagation of solitary Schallamach waves.* Physical Review E, 2015. **91**(1): p. 012408.

[51] Viswanathan, K., N.K. Sundaram, and S. Chandrasekar, *Stick-slip at soft adhesive interfaces mediated by slow frictional waves.* Soft matter, 2016.

[52] Berman, A.D., W.A. Ducker, and J.N. Israelachvili, *Origin and characterization of different stick-slip friction mechanisms.* Langmuir, 1996. **12**(19): p. 4559-4563.

4 The Effect of Normal Force and Rate on Kinetic Coefficient of Friction of Elastomeric Materials

Ahmad R. Mojdehi[1], Douglas P. Holmes[2], Christopher B. Williams[3], Timothy E. Long[4], David A. Dillard[1]

[1]Department of Biomedical Engineering and Mechanics, Virginia Tech, Blacksburg, VA 24061

[2]Department of Mechanical Engineering, Boston University, Boston, MA 02215

[3]Department of Mechanical Engineering, Virginia Tech, Blacksburg, VA 24061

[4]Department of Chemistry, Virginia Tech., Blacksburg, VA 24061

4.1 Introduction

Understanding the frictional response of materials is a topic of significant fundamental and practical interest in the field of mechanical engineering. The well-known empirical Coulomb's friction law, which suggests no normal load dependence for the coefficient of friction (COF), has been successfully applied to many physical systems including metals, polymers, and elastomers [1-5]. However, in some cases such as with soft materials, the idealized Coulomb's friction law does not hold due to a dependence of the COF on the normal force [5-8]. Furthermore, friction in soft viscoelastic materials has been widely expressed as a summation of friction due to work of adhesion (*adhesion friction*), bulk viscoelastic dissipation (*VE hysteresis friction*) that is significantly affected by contact rate (e.g. sliding velocity) and temperature [9-14], and substrate material and roughness [15-17], and cohesive loss friction due to wear (*cohesion friction*). A few studies also investigated the effect of work of adhesion hysteresis (*adhesion hysteresis*) on friction, observing a correlation between the adhesion hysteresis and friction [18-23]. The adhesion hysteresis is analogous to the difference in advancing and receding contact angles when a liquid droplet is placed on a tilted substrate. Cohesion friction is typically assumed to be negligible compared to the other contributions on the friction of elastomeric materials [6, 24]. However, *cohesion hysteresis* analogous to that of adhesion hysteresis could perhaps arise from viscoelastic dissipation due to cohesive failure of viscoelastic materials.

Several experimental setups have been developed to characterize frictional response of elastomers using different configurations such as sled [25], pendulum [26], and pin-on-disk [27]. At high velocities, there exist some limitations for devices that have continuous contact with the elastomer over a relatively long period of time (e.g. pin-on-disk), such as wear and frictional heating that

may affect the frictional response of the elastomers [28, 29]. Alternatively, higher velocity friction response may be simulated by reducing the temperature of the environment and applying the time-temperature superposition principle (TTSP) to reduce frictional heating issues on elastomers using common high speed friction test setups such as pin-on-disk. However, changing the environment's temperature would change the temperature of both bulk and surface domains, while in real applications elastomers may experience different contact frequencies exerted by surface asperities at the interface and bulk regions, depending on the nature of substrate's asperities and depth-dependent viscoelastic dissipation. Applying the TTSP technique could be challenging for the case of thermo-rheologically complex materials, where the shift factors would be a function of frequency in addition to temperature. Moreover, experimental observations of sliding elastomeric materials over a smooth substrate show progressive waves of detachment and reattachment known as *Schallamach waves* [30], that depend on the test rate and normal force [31-33], making it necessary to perform the friction test under the conditions that resemble those found in real applications.

It has been widely accepted that adhesion friction, *i.e.* friction involving macroscopically smooth substrates, can be written as a product of a constant, normal load-independent shear stress, and the real area of contact [3, 7, 34]. Therefore, the load dependence of adhesion friction is dictated by that of the resulting real contact area. In recent decades, several studies have been conducted investigating the change in real area of contact with respect to normal force. Hertzian elastic contact theory is used to derive a relationship between the contact area and normal force for a single asperity, revealing a nonlinear dependence of contact area with respect to the normal force [35]. However, for multi-asperity contact, a linear relationship was found between the contact area and the normal force using the Greenwood-Williams theory [36] and other approaches [37, 38]. A linear relationship between real contact area and normal force results in a constant (Coulomb) COF, and while a nonlinear relationship causes an increasing COF for decreasing normal load, assuming constant shear stress. Furthermore, in most friction test results obtained by sliding rubber on macroscopically smooth surfaces, *i.e.* adhesion friction, the COF was found to increase with decreased loading [6, 39, 40]. On the other hand, the COF obtained from VE hysteresis friction, which is originated from bulk energy dissipation of viscoelastic materials, is shown to decrease with decreasing normal force [6, 8, 41]. However, to the authors' knowledge, the effect of adhesion/cohesion hysteresis on the COF with respect to the normal force is not reported in the

literature. Figure 4-1and Table 4-1 demonstrate and summarize these three major contributions in the friction of viscoelastic materials, *i.e.* VE hysteresis friction, adhesion friction, and adhesion hysteresis friction, together with physical examples of each and the reported trends with respect to the normal force.

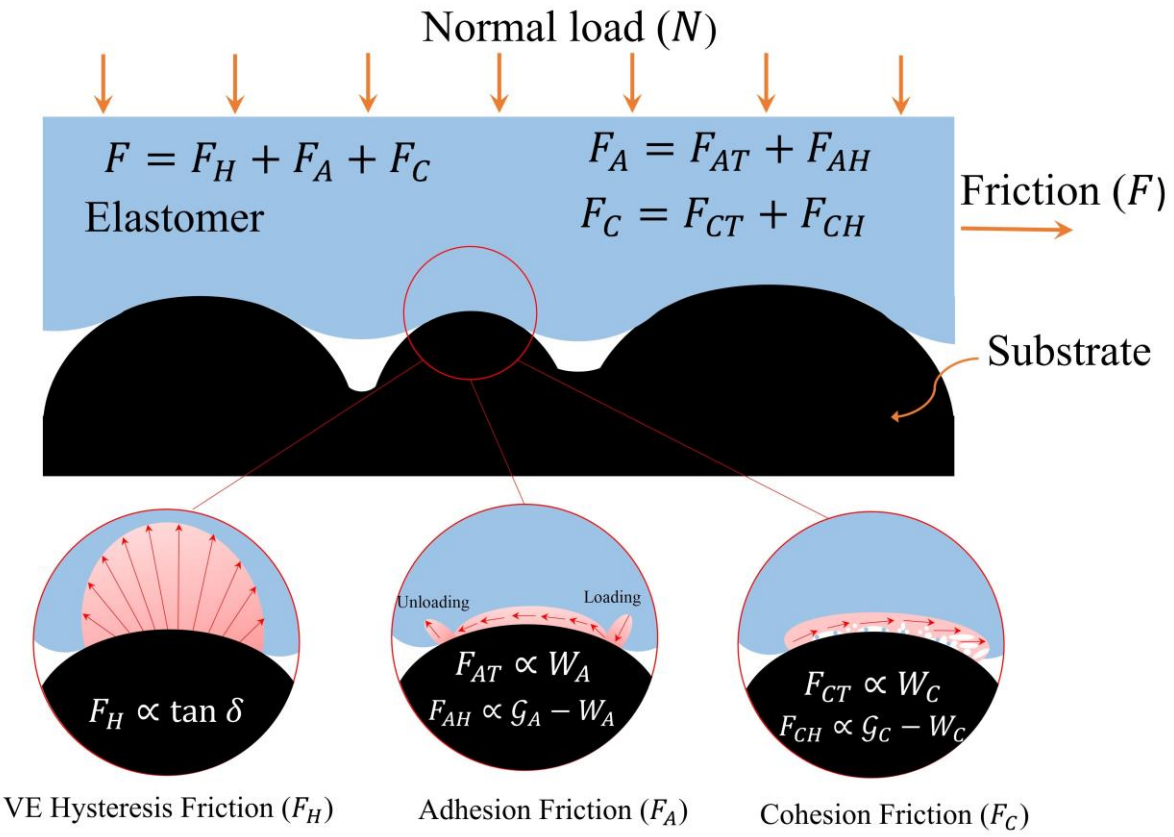

Figure 4-1. Schematic illustration of three different contributions, *i.e.* VE hysteresis friction, adhesion friction, and cohesion friction, to the frictional response of viscoelastic materials. The VE hysteresis friction is related to the bulk viscoelastic energy dissipation (e.g. the loss tangent, tan δ=E''(ω)/E'(ω)), adhesion friction is related to the thermodynamic work of adhesion (W_A) and adhesion hysteresis friction is due to loading and unloading, cohesion friction is related to the cohesive failure (wear) and thermodynamic work of cohesion (W_C) of the elastomer and also cohesion hysteresis resulting from viscoelastic energy dissipation. $\mathcal{G}_A and\ \mathcal{G}_C$ are strain energy release rate associated to the adhesive failure and cohesive failure, respectively.

Table 4-1. Different contributions to the friction of viscoelastic materials and the corresponding physics, examples, and trends with respect to the normal load

Name	Physics	Examples/Analogies	COF vs Normal Load
VE Hysteresis Friction	Bulk viscoelastic dissipation	Rolling cylinder, Sliding on rough substrates	COF decreases for decreasing normal load [6, 8, 41]
Adhesion Friction	Work of adhesion	Sliding on macroscopically smooth substrates, Adhesive failure	COF increases for decreasing normal load [6, 39, 40]
	Work of adhesion hysteresis		Unknown
Cohesion Friction	Work of cohesion	Wear, Cohesive failure	Constant
	Work of cohesion hysteresis		Unknown

In this paper, the effects of rate and normal force on the kinetic COF of elastomeric materials are investigated. Two different elastomers, namely silicone and acrylic-based elastomers, with significantly different viscoelastic properties, *e.g.* glass transition temperatures (T_g) and rubbery moduli, are examined. The two elastomers had comparable kinetic COF at low speeds, while at high speeds and light normal force, the frictional response of the acrylic elastomer was found to be significantly lower compared to the silicone elastomer. Therefore, a custom-built, instrumented pendulum setup is implemented to characterize the frictional response of these elastomers under such conditions. The COF is quantified by measuring normal and friction forces between elastomers and a macroscopically smooth poly(methyl methacrylate) (PMMA) substrate. Although both systems tended to obey Coulomb's friction law at higher loads, we found opposite responses at very low normal forces. The COF of the acrylic decreased with decreasing normal force, while that of the silicone increased. To further explore the origin of the anomalous acrylic response, the effects of rate and surface properties were examined by performing experiments at a

lower velocity and with graphite powder present on the interface. Furthermore, drop tests using different size steel balls and/or substrates at different temperatures were performed to correlate the surface hysteresis to the frictional response of the elastomers. The effects of surface hysteresis, T_g, and modulus on the frictional behavior of elastomers are discussed.

4.2 Theoretical Model

As mentioned before, the friction in soft viscoelastic materials has been widely expressed as $F = F_H + F_A + F_C$, where $F_H$is viscoelastic hysteresis friction, F_A is adhesion friction, and F_C is cohesion loss friction [6, 24]. The adhesion and cohesion friction forces could each have two contributions, one from thermodynamic work of adhesion/cohesion (F_{AT} and F_{CT}) and the other one from rate-dependent hysteresis due to loading-unloading (F_{AH} and F_{CH}), resulting in $F_A = F_{AT} + F_{AH}$ and $F_C = F_{CT} + F_{CH}$. In the following, we will discuss how each contribution changes with normal force.

Viscoelastic hysteresis friction: The viscoelastic hysteresis friction originates from bulk viscoelastic dissipation and is typically dominant on rough surfaces, where numerous asperities cause repeated loading and unloading at depths commensurate with asperity dimensions. The hysteresis friction force obtained from rolling a sphere on a flat rubber was theoretically predicted and experimentally validated to scale with normal force as $F_H \propto N^{4/3}$ for linear elastic materials based on the Hertz contact model [8]. Furthermore, energy dissipation in viscoelastic materials scales with the square of the stress/strain resulting to the viscoelastic hysteresis friction force to scale with the square of normal force ($F_H \propto N^2$), and therefore the hysteresis COF of the form $\mu_H \propto N$ [28].

Adhesion friction: Adhesion friction is related to the van der Waals interaction between the two surfaces as reflected by the thermodynamic work of adhesion and, for viscoelastic materials, there could be a hysteresis term associated to the adhesion friction due to loading-unloading condition ($F_A = F_{AT} + F_{AH}$), where F_{AT} is related to the thermodynamics work of adhesion for forming the bond and F_{AH} is related to viscoelastic adhesion hysteresis. This is analogous to, but can access energy dissipation mechanisms well beyond traditional advancing and receding angle hysteresis. Adhesion friction is typically dominant on smooth surfaces and the bonding term is typically modeled as $F_{AT} = \tau\, A_{real}$, where τ is a constant shear stress and A_{real} is the real area of contact. Based on Hertzian contact model, $A_{real} \propto N^{2/3}$ resulting in a COF of the form $\mu_{AT} \propto N^{-1/3}$ [7].

It is worth noting that the above relationships are also implemented in the friction of metals, where contact area is assumed to be proportional to the normal load, *i.e,* $A_{real} \propto N$, during plastic deformation of asperities for perfectly plastic behavior, giving rise to the constant Coulomb COF for metallic materials [42]. We propose a theoretical model for the adhesion hysteresis friction for viscoelastic material based on the energy dissipation during the loading and unloading condition in the form of $\mathcal{G} - W_A = W_A\phi(a_T V)$, where $\mathcal{G}$ is the strain energy release rate corresponding to unloading (debonding), W_A is the thermodynamic work of adhesion associated with the loading condition, and ϕ is a dimensionless viscoelastic dissipation function that depends on the viscoelastic properties of the materials, the crack velocity *V* and temperature T; a_T is the Williams-Landel-Ferry (WLF) shift factor [43-45]. From the JKR approach we can come up with a relationship between the work of adhesion and the normal load N as, $W_A = (\frac{4\,E^* a^3}{3R} - N)^2 / 8\pi E^* a^3$, where a is radius of contact, R is radius of the sphere in contact with the substrate, E^* is given by $1/E^* = (1-\nu_1^2)/E_1 + (1-\nu_2^2)/E_2$; ν and E being the Poisson's ratio and elastic modulus, respectively.

Multiplying the adhesion hysteresis term $(\mathcal{G} - W_A)$ by the contact area (πa^2) results in the adhesion hysteresis energy dissipation per loading-unloading cycle as $(\mathcal{G} - W_A)\pi a^2 = \frac{\left(\frac{4\,E^* a^3}{3R} - N\right)^2}{8E^* a}\phi(a_T V)$.

Now, assuming the micro-asperities on the substrate's surface have an average spacing d, the friction force due to adhesion hysteresis energy dissipation can be written as $F_{AH} = \frac{(\mathcal{G}-W_A)\pi a^2}{d} = \frac{\left(\frac{4\,E^* a^3}{3R} - N\right)^2}{8E^* a d}\phi(a_T V)$. Accordingly, the adhesion hysteresis friction scales with the normal force as $F_{AH} \propto N^2$, leading to a COF of the form $\mu_{AH} \propto N$. Therefore, the total adhesion friction can be written as $\mu_A = \mu_{AT} + \mu_{AH}$ where $\mu_A \propto N^{-1/3} + N$.

Cohesion friction: The cohesion loss friction, F_C, is related to material wear, and similar to adhesion friction outlined above, can be written in terms of thermodynamic work of cohesion (F_{CT}) and the contribution from viscoelastic hysteresis (F_{CH}), where $F_C = F_{CT} + F_{CH}$. The thermodynamic cohesion friction is typically very small compared to the other contributions in the total friction force (between 1-2% of the total friction force) and typically obeys Coulomb's friction law resulting in a constant COF, $F_{CT} \propto N$ and $\mu_{CT} \sim const$, albeit quite small [24, 46].

However, the cohesion hysteresis friction (F_{CH}) can be significant due to viscoelastic dissipation for elastomeric materials. The same theoretical basis for adhesion hysteresis friction discussed above can be implemented for the cohesion hysteresis friction if the work of adhesion (W_A) replacing with work of cohesion (W_C) for contact between two identical materials, resulting in a COF of the form $\mu_{CH} \propto N$ and therefore $\mu_C \propto N$, assuming μ_{CT} is small.

4.3 Experiments

Friction test: A standard Izod pendulum setup (Testing Machines Inc., NY, USA) was modified to perform the dynamic friction tests, as illustrated in Figure 4-2a. The elastomers (silicone and acrylic-based elastomers, 35mm x 22mm rectangular strips, backed with a fabric with total thicknesses of 1mm (acrylic) and 0.75mm (silicone) supplied by a sponsor and were intended for a specific application) were bonded to a mount on the arm of the pendulum (length: 406mm, mass: 230g, center of mass: 279mm from the hinge). The custom-designed lightweight mount (made by extrusion based 3D printer) was hinged to the arm such that the normal force on the elastomer is transmitted directly to the piezoelectric force sensor (44.5 N 208C01, PCB Piezoelectronics Inc., NY, USA) on the top of the mount (see Figure 4-2b). A small bump was made on the mount at the contact point with the force sensor to apply the normal force at the center of the force sensor. The substrate material (clear PMMA sheets as received from McMaster-Carr) was in contact with a similar force sensor on the front side to measure the friction force, as shown in Figure 4-2b. The PMMA substrate was maintained in contact with the force sensor using tape, to minimize the effect of friction between the substrate and the pendulum base. The piezoelectric force sensors were connected to a signal conditioner (482C15, PCB Piezoelectronics Inc., NY, USA), which amplified the signals and passed them to a data acquisition (DAQ) card (9205, National Instruments, TX, USA). The data was then monitored and analyzed using LabVIEW^{TM} (National Instruments, TX, USA) software. The normal force was adjusted by inserting steel shims underneath the substrate. In order to modify the surface of elastomers, graphite powder (MZ-5, AGS Company, MI, USA) was applied to completely cover the surface of elastomers, and the excess powder was removed by a razor blade. The substrate was cleaned with isopropyl alcohol before each test, while the elastomers were cleaned with water and soap to avoid alcohol effects on elastomers. The results represent the means of triplicate experiments. The maximum velocity permitted by this setup was

3 m/s. To be able to reach very low velocities, a translational actuator (PI, M-229.26S, Karlsruhe, Germany) was attached to the pendulum arm to pull it across the substrate at 5 mm/min(See Figure 4-2c). Figure 4-2d shows representative normal and friction force traces for acrylic.

Drop test: Figure 4-3 shows a schematic of the drop test implemented in this study. The experiment was inspired by the pioneering works performed by Grosch [47] to separate the

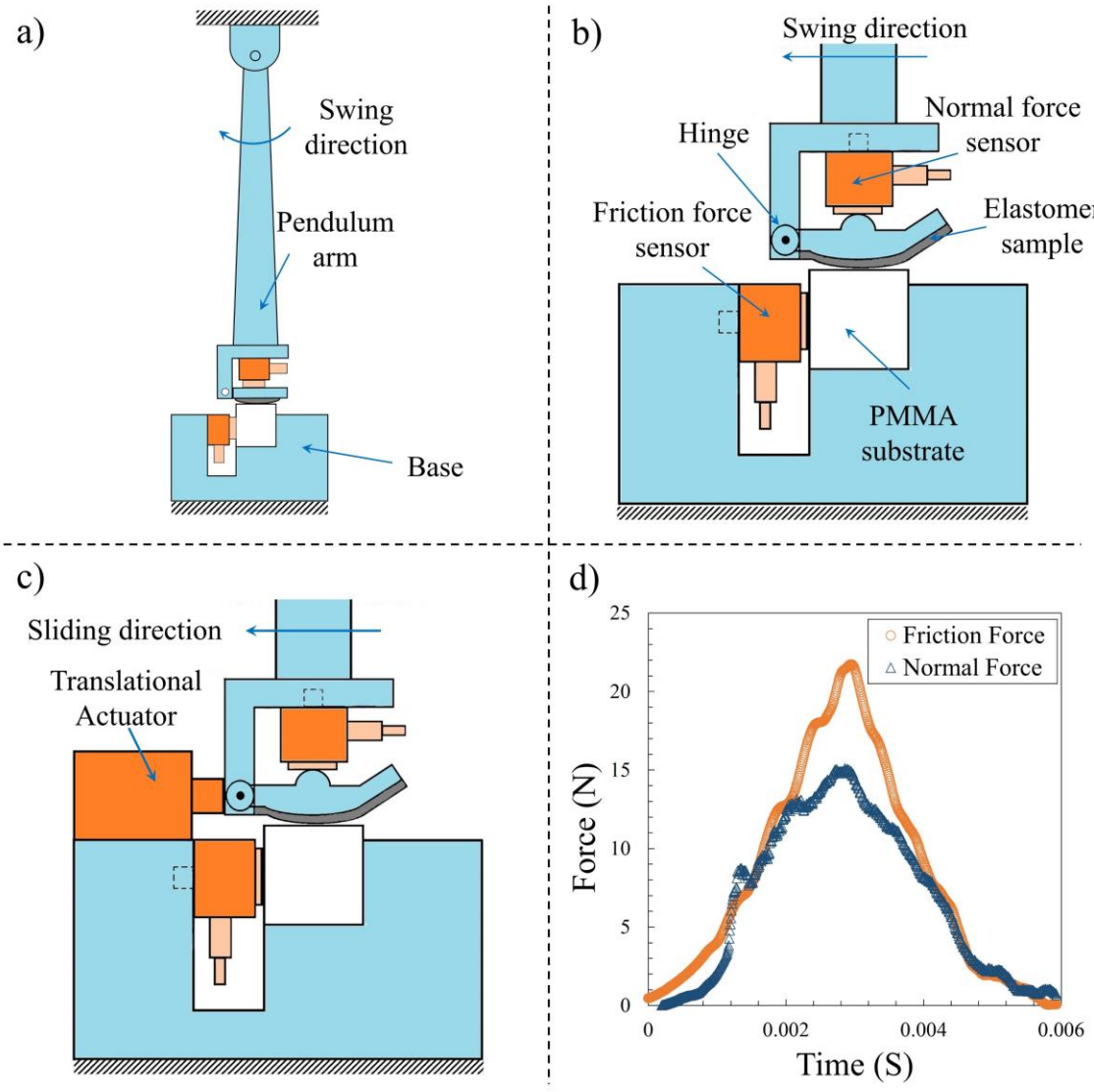

Figure 4-2. a) Instrumented pendulum setup for measuring dynamic coefficient of friction. b) Zoomed view of the setup showing the normal and friction force sensors and the mechanism used to avoid shear force on the force. c) Translational actuator attached to the pendulum setup for measuring coefficient of friction at low velocities. d) Representative normal and friction force traces for acrylic elastomer.

adhesion and hysteresis friction forces of polymers, using a powder on the polymer surface and pendulum tack measurement device developed by Gent [48]. In order to measure the adhesion hysteresis of elastomers, steel spherical balls of different sizes (4.7, 6.4, 11.2, 14.3 mm diameter) were dropped from a height of H=635mm on elastomer samples that were bonded to PMMA substrates (11.5mm thick). The elastomers and substrates were cut in circular shapes (35mm diameter) and bonded to

each other using an adhesive (Gorilla Super Glue, Cincinnati, Ohio, US). The substrates were bonded to glass plates using a dissipative double-sided adhesive tapes (3M VHB tapes, St. Paul, MN, USA) to prevent vibrations during contact. The graphite powder was applied to the elastomer surface using the same procedure as discussed for the friction test. Furthermore, the elastomers temperature was increased from room temperature (25^{o}C) to two higher temperatures (50^{o}C and 75^{o}C) by keeping the base assembly in the oven until the mounted specimens equilibrated with the oven temperature. The elastomer was immediately placed in an open-ended glass cylinder and a glass plate was placed on the top of the cylinder to prevent significant change in the elastomer's

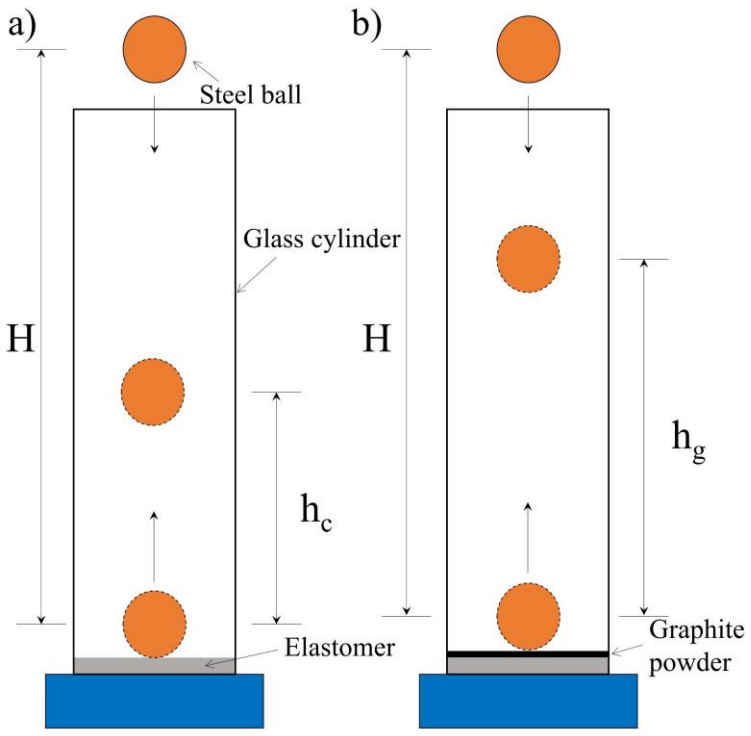

Figure 4-3. Drop test of a spherical ball on a) Cleaned elastomer b) Elastomer powdered with graphite, and the corresponding initial and rebound heights.

temperature after removing from the oven, and the drop test was performed as quickly as possible afterwards. The surface temperature was measured using an infrared thermometer (Extech Instruments 42510A, FLIR Systems Inc., USA) for a few cases and the temperature decrease was about 10% ^{o}C of the oven temperature. The rebound height was measured using a high-speed camera (FASTCAM APX RS, Photron, San Diego, CL, USA) and the difference between the rebound heights for the cleaned (h_c) and powdered elastomers (h_g) was used as a measure of surface adhesion hysteresis.

Dynamic Mechanical Analysis (DMA): A TA Instruments Q800 DMA instrument was used to perform dynamic mechanical analysis on bulk polymer samples of the silicone and acrylic-based elastomers (without fabric backing) used in the study. A tensile clamp fixture was used to perform the experiment in tension mode. First, the transducer was calibrated after installing the tensile fixture and then the sample was attached to a clamp. For the temperature sweep experiments, the frequency was set to 1 Hz, whereas for the frequency sweep experiments the frequency was swept from 1 to 100 Hz, while the temperature was increased from -79^{o}C to 52^{o}C for the acrylic and from -150^{o}C to 52^{o}C for the silicone, with a step size of 3^{o}C with 5 min equilibrium time. The master curves were developed by horizontally shifting the data by distances corresponding to shift factors, based on a reference temperature of 22^{o}C, following the concept of TTSP [49].

4.4 Results and Discussion

The average (time average during contact time) of normal and friction forces were used to calculate the COF obtained from the pendulum setup (see Supporting Information for further details about the other metrics for the COF). Figure 4-4 depicts the variation of kinetic COF with respect to the normal force for the cleaned and powdered silicone and acrylic elastomers. Since the substrate used here was macroscopically smooth (PMMA sheets as received), we would expect the VE hysteresis friction (F_H) be small and will assume negligible in the frictional response of the elastomers in this study. The frictional response of cleaned silicone is similar to the adhesion friction associated to the thermodynamic work of adhesion on macroscopically smooth substrates reported in the literature, *i.e.* increase in COF with decrease in normal force [5, 6, 39, 40, 50, 51]. Furthermore, as there was no visible evidence regarding cohesive failure of the silicone, we would expect the cohesion friction would not be applicable for the case of silicone. However, the response of cleaned acrylic at low normal forces was in contrast to what was expected based on the adhesion

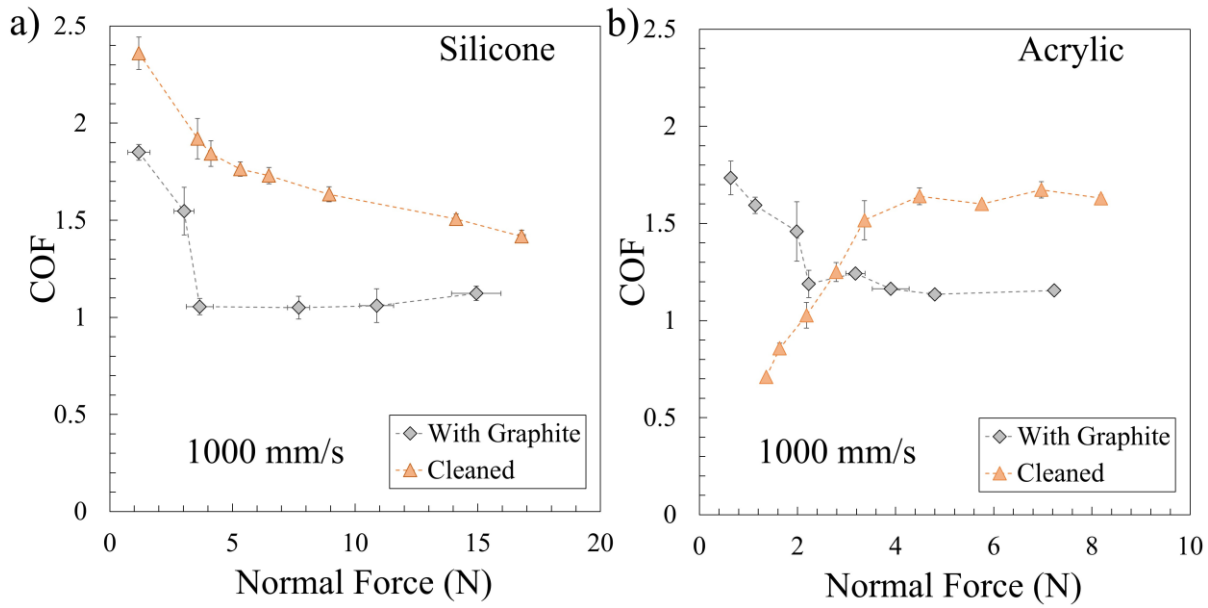

Figure 4-4. Coefficient of friction of a) Silicone elastomer, b) Acrylic elastomer, with and without graphite powder. The apparently anomalous trend for cleaned acrylic is observed in (b). Error bars represent ±1 standard deviation for triplicate runs.

friction on macroscopically smooth surfaces. As shown in Figure 4-4, the COF for cleaned acrylic was lower at low normal forces, and then reached a plateau at higher values of *N*. We also observed residue of acrylic on the substrate after friction tests on cleaned acrylic, giving rise to the cohesive failure of the acrylic, rather than interfacial failure like that of silicone. In addition, there is a threshold normal force in which the COF plateaus (~2.2 N for acrylic with graphite, ~4.4 N for cleaned acrylic, and ~3.5 N for silicone with graphite), which is possibly where the real contact area approaches the projected contact area, resulting in Coulomb's friction (constant COF). However, the threshold value could also be related to material properties such as yield stress if normal stresses, instead of normal forces, were used as the abscissa, though the contact area was not controlled to calculate the normal stress. The corresponding threshold normal forces were lower for the acrylic compared to the silicone, as the acrylic was softer than the silicone, perhaps resulting in saturating the contact area at a lower normal force. For the same reason, the range of normal forces covered for the silicone and acrylic were different in order to capture the transition in the COF from low to high normal forces.

Several experiments were performed to explore the origin of the acrylic response at very low normal forces. First, we checked if the response arises from surface or bulk properties of the elastomer. For this purpose, the experiment was conducted in the presence of graphite powder on the surface. Figure 4-4 also shows the response of the silicone and acrylic when dusted with graphite powdered on surfaces as a function of normal force. The response in the presence of graphite powder was similar for both the silicone and acrylic, and is consistent with adhesion friction, showing that in the very low normal force regime, the response is dominated by surface properties, as graphite contaminant changed the interface between the elastomer and substrate without affecting bulk hysteretic behavior. Furthermore, the presence of graphite powder dusting between the acrylic elastomer and substrate prevented the bonding formation between the two materials and therefore eliminated cohesive failure in the acrylic. Interestingly, the COF in the very low normal force regime with graphite as a surface modifier (which is very common as a lubricant for lowering the COF) was higher than that of the corresponding cleaned acrylic surface. The increase in the COF with decreasing normal load with the presence of graphite could also be justified by the well-known Stribeck curve [52] in the hydrodynamic lubrication regime where roughness of the substrate is negligible compared to the thickness of the lubricant, resulting in the COF dominated by shearing of the lubricant [53]. The hydrodynamic lubrication regime

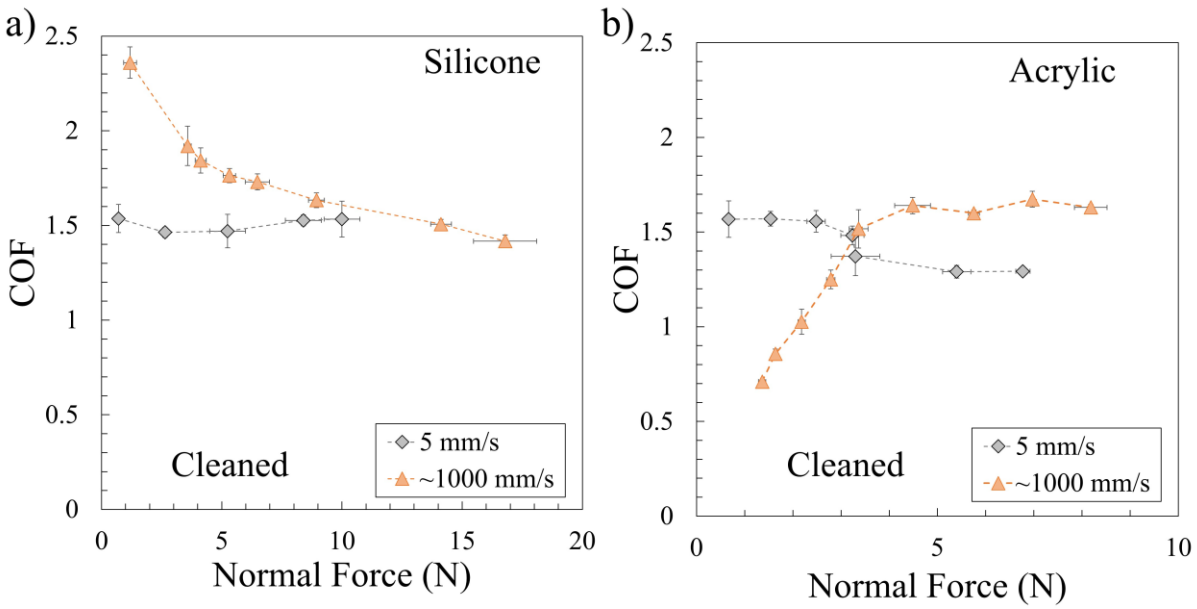

Figure 4-5. Coefficient of friction of a) Silicone elastomer, b) Acrylic elastomer, at two different velocities

corresponds to large values of Hersey number ($\eta v/N$), where η is viscosity of the lubricant, v is sliding velocity, and N is normal load, in which the COF increases with Hersey number. Therefore, in the low normal load regime and at high velocity, *i.e.* high Hersey number, the response of elastomers with graphite present is consistent with the hydrodynamic lubrication regime in the Stribeck curve, which was found to be also applicable to solid lubricants such as graphite [54].

Furthermore, in order to examine if the response of acrylic is affected by adhesion/cohesion hysteresis friction due to viscoelastic dissipation, the rate dependence of the response was evaluated by reducing the contact velocity by about three orders of magnitude. Figure 4-5 demonstrates the response of the silicone and acrylic materials at two different rates for different values of normal forces, revealing the rate dependent response of the acrylic at low values of normal forces, resulting in a change in the trend of COF with respect to the normal force. Although the COF was lower at low velocity compared to the high velocity for the silicone, the overall trend did not change substantially. Comparing the two experiments (i.e. changing the surface and rate) suggests the frictional response of the acrylic at low normal forces possibly originates from rate-dependent cohesion hysteresis response.

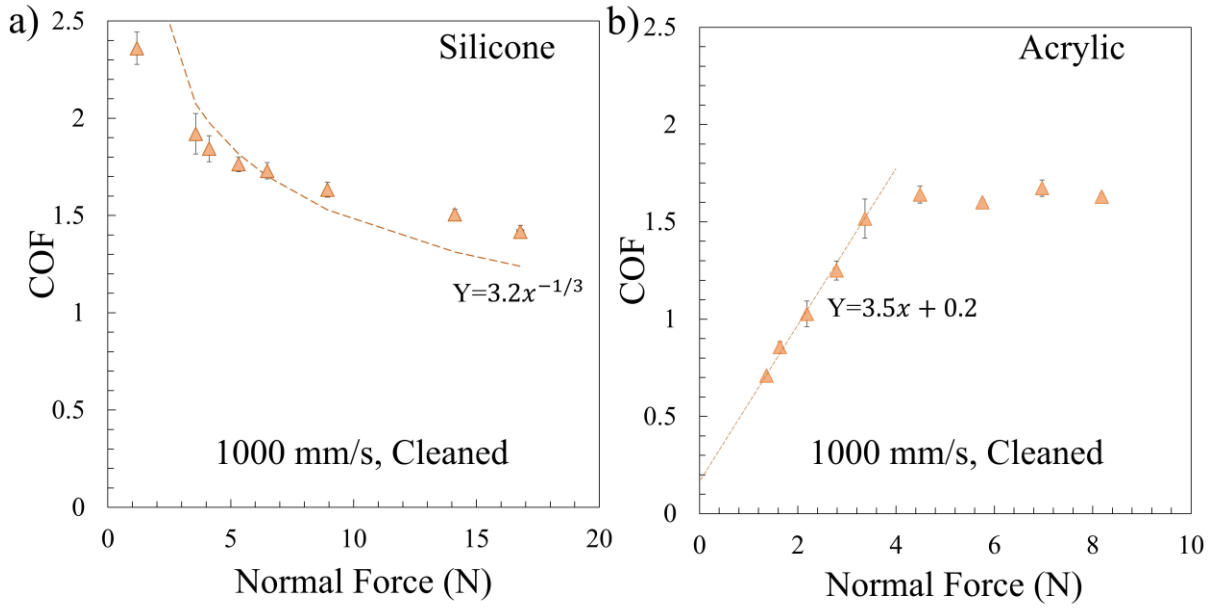

Figure 4-6. Comparison of experimental and theoretical COF versus normal force a) Silicone elastomer and b) Acrylic elastomer for cleaned elastomers at test speed of 1000 mm/s. Markers correspond to the experimental data and dashed lines correspond to the theoretical modeling.

Figure 4-6 demonstrates a comparison of the theoretical models for the COF versus normal force for the cleaned silicone and acrylic elastomers (at 1000 mm/s) with the experimental data, showing good agreement with the adhesion friction model for the silicone and the proposed cohesive hysteresis friction model for the acrylic. Smith proposed the concept of load-independent micro-hysteresis friction force, resulting from sufficiently high surface energy of the rubber, leading to self-adherence between rubber and the microtexture on the macroscopically smooth substrate [6, 40]. He related the experimentally observed constant y-axis intercept value found in the friction force versus normal force curve to the surface micro-hysteresis friction concept, assuming a linear relationship between the friction and normal forces, *i.e.* Coulomb friction. In his report, he analyzed 39 different friction test results obtained by other researchers for sliding rubber on macroscopically smooth substrates, showing an increase in the COF with a decrease in normal force [6]. However, the effect of rate on the suggested surface micro-hysteresis friction mechanism

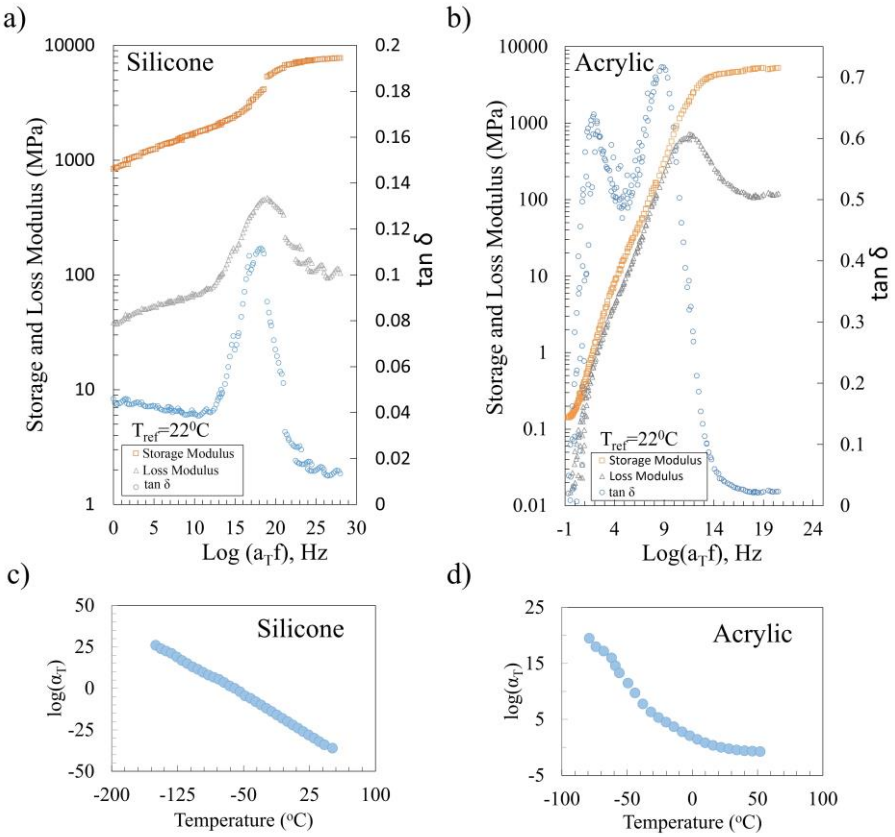

Figure 4-7. Storage modulus, loss modulus, and tan δ versus shifted frequency master curves for a) Silicone elastomer b) Acrylic elastomer on log-log scale. Log of shift factor vs. temperature plots for c) Silicone elastomer and d) Acrylic elastomer

was not investigated. Moreover, the y-intercept for the friction versus normal forces curve of the acrylic obtained here would be negative, showing that a simple constant micro-hysteresis friction model, by assuming a linear relationship between the friction and normal forces, would be problematic when the experiment rate changes.

In order to find possible correlation between the viscoelastic rate-dependent response of the elastomers and the COF, DMA tests were performed to capture the dynamic mechanical properties of the elastomers such as storage modulus, loss modulus, and tan δ. The DMA results of the acrylic and silicone elastomers provided rubbery storage moduli (E') of about 0.2 and 1 MPa, respectively, differing by about 2/3 (see Supporting Information for more details). This shows that the acrylic elastomer is close to the Dahlquist criterion for the storage modulus of pressure sensitive adhesives, exhibiting tack at room temperature, which is apparent when touching the acrylic elastomer. Because of the low modulus of the acrylic, the polymer chains can conform to smaller surface asperities (*e.g.* in the order of micro/nanometer for macroscopically smooth surfaces) compared to the stiffer elastomers (*e.g.* silicone), forming a stronger adhesion bond. During debonding perhaps as the bond strength is stronger than the strength of the material itself for acrylic, the polymer chains break leading to the cohesive failure. Moreover, as shown in the master curves (Figure 4-7), the tan δ peak for the acrylic at reference temperature (T=22^{o}C) occurs at a frequency significantly lower than that of silicone (acrylic had two tan δ peaks 10^2 Hz and 10^9 Hz, the peak for silicone was 10^{18} Hz), resulting in higher sensitivity of the acrylic friction response to the change in the contact velocity in the range of velocities studied in this work (with contact velocity (v) on the order of 1 m/s and contact length (d) on the order of cm, resulting in a contact frequency (v/d) of the order of 10^2 Hz).

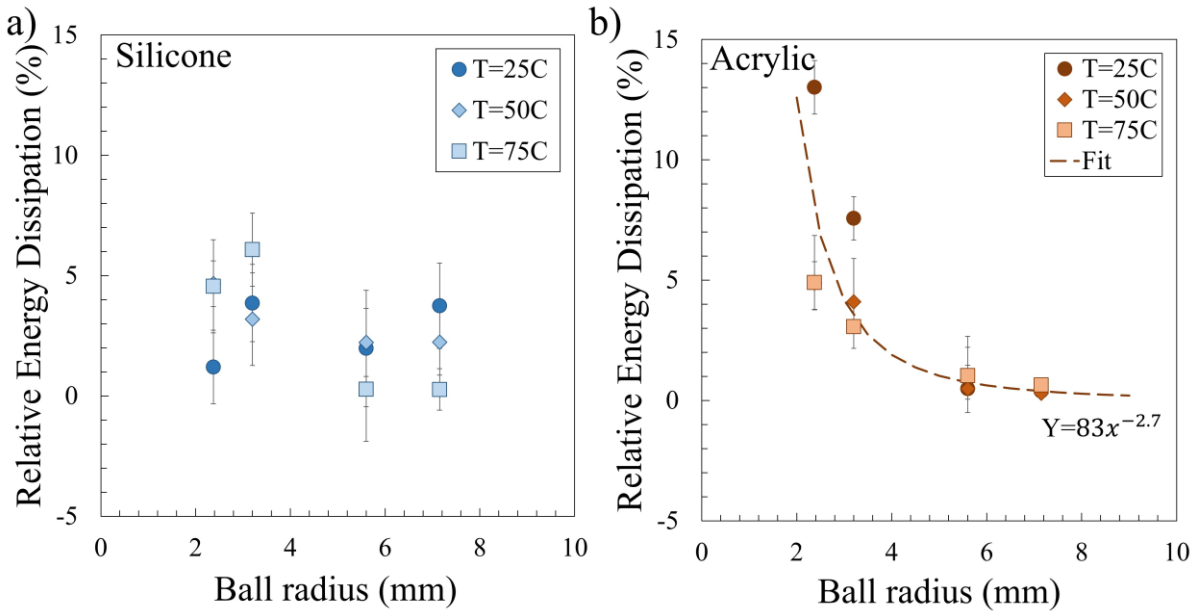

Figure 4-8. Relative energy dissipation due to adhesion hysteresis for a) Silicone elastomer and b) Acrylic elastomer, for four different size of steel balls and three temperatures. The dashed line corresponds to the power-law fit to the data for acrylic.

To support the hypothesis for the friction response of acrylic, we performed drop tests on the elastomer samples at different temperatures using different sizes of steel balls to measure the surface hysteresis of both elastomers. The balls were dropped from a height of 635 mm while the rebound heights were measured for the cleaned and graphite powdered elastomers at three different temperatures. Figure 4-8 exhibits the contribution of surface hysteresis to the total energy dissipation normalized by weight of the balls ($(h_g - h_c) \times 100/H$ as shown in Figure 4-3) as a function of ball's weight at three different temperatures for both silicone and acrylic. There were no significant rebound height differences among the different ball sizes and temperatures for the silicone. However, the relative energy dissipation from surface hysteresis of the acrylic increased by decreasing the size/weight of the balls and temperature, showing that the surface hysteresis was more dominant at lower normal forces and higher contact rate, based on TTSP concept. In order to compare results from the drop tests with those of friction, the absolute energy dissipation should be plotted as a function of weight, though this conversion results in very large standard deviation for the data shown on Figure 4-8, where we fitted a power-law curve on the data for the acrylic, leading to an exponent of -2.7. Since the weight of the balls scales with the radius to the third power (R^3), using the exponent obtained from the power-law fit, the absolute energy dissipation

would scale with $R^{0.3}$, i.e. decrease in energy dissipation by decreasing the size/weight of the ball, which is consistent with the results of friction test. Furthermore, normal force was shown to affect the adhesion hysteresis of a glassy polymer, e.g. polystyrene, using a surface forces apparatus, suggesting that decreasing or increasing the normal load can shift the peak corresponding to the adhesion hysteresis to below or above T_g, respectively [55]. Overall, based on the results obtained from the pendulum friction tests and supported by the drop tests, the acrylic response is believed to originate from cohesion hysteresis, where the low storage modulus and the dissipative viscoelastic response play an important role in the friction response. In addition, considering the three additive terms in the friction of viscoelastic materials, i.e. VE hysteresis friction, adhesion friction, and cohesion friction, the response of acrylic could be justified if we assume the cohesive hysteresis contribution is dominant compared to the other terms. The VE hysteresis friction can be considered negligible for the two elastomers as the friction test is performed on a macroscopically smooth substrate. Since we observed cohesive failure for the case of acrylic, the adhesion friction is not applicable to this case assuming no interfacial failure. Therefore, the cohesion friction is assumed to be the dominant term for the acrylic, and as the thermodynamic cohesion COF does not depend on the normal load and is typically small compared to the other terms [24], the major contribution to the acrylic COF, at low normal forces and high rates regime, would most likely be cohesion hysteresis, as supported by the proposed theoretical scaling with normal force and also consistent with the results of drop test. However, for the case of silicone, as there was no visual evidence suggesting cohesive failure, it is assumed that the frictional response of silicone is dominated by adhesion friction. The adhesion hysteresis friction is shown to be negligible for the silicone based on the drop test results and the silicone is less dissipative compared to the acrylic based on the DMA results. Therefore, the thermodynamic adhesion friction likely dominates for the case of silicone, supported by the theoretical scaling law based on the adhesion friction model. The results obtained from this study could give more insight for design and manufacturing of systems where the friction plays an important role, such as tires, footwear, sporting goods, and brakes, by taking into account the effects of normal force, rate, and adhesion hysteresis on the frictional response of the systems.

4.5 Conclusions

In conclusion, we studied the kinetic COF of silicone and acrylic-based elastomers, investigating the effects of normal force and rate on the frictional response on a macroscopically smooth

substrate. A pendulum setup was instrumented using piezoelectric force sensors to measure the friction and normal forces. Very different responses were found for the two elastomers, in that for decreasing normal forces, an increase in COF was observed for the silicone and a decrease in COF was seen for the acrylic. The frictional response of the silicone was consistent with that of adhesion friction reported in the literature for the friction of rubber on smooth substrates, while the acrylic response was in contrast to the literature data. To further explore the origin of acrylic response, experiments were performed at a lower velocity, and also with graphite powder present on the interface, to examine rate dependence and surface effects and to determine underlying causes. We found that the acrylic response anomaly at very low normal forces likely originates from a rate dependent response of surface properties, giving rise to a hysteretic contribution even on a smooth substrate. To further support the hypothesis, drop tests were performed to measure the adhesion hysteresis of the elastomers. We found that the surface hysteresis for the acrylic was more dominant for smaller balls (i.e. low normal forces) compared to the bigger ones (higher normal forces). The storage modulus and tan δ peak are believed to play an important role in the frictional response of both elastomers. This study could improve insights gained from DMA data and adhesion hysteresis experiments, when obtaining and interpreting the effect of normal force on kinetic COF of elastomers.

Supporting Information

Figure 4-9 depicts the storage and loss moduli, and tan δ curves obtained from DMA temperature sweep experiments at 1 Hz. The glass transition temperatures (T_g) of silicone and acrylic samples were -108^{o}C and -43^{o}C, respectively, as determined from the peak in tan δ.

Since the path of pendulum arm was circular, the normal force was not constant during the contact, increasing then decreasing as the pendulum passed through the bottom of the arc. The data obtained from this setup allows three metrics to be used to calculate the COF, *i.e.* by using average values of the normal and friction forces, maximum values of the normal and friction forces, and dial indicator measuring energy dissipation on the pendulum setup as a measures of friction force together with the normal force from force sensor. The DAQ card limited the maximum sampling rate of the data to 250,000 samples per second. We evaluated the sensitivity of each measure of COF to the sampling rate to select the best measure. As expected, the average and dial metrics had

the lowest variability with respect to the sampling rate. We chose the average measure in the rest of this study to evaluate the effect of other parameters on the kinetic COF of elastomers.

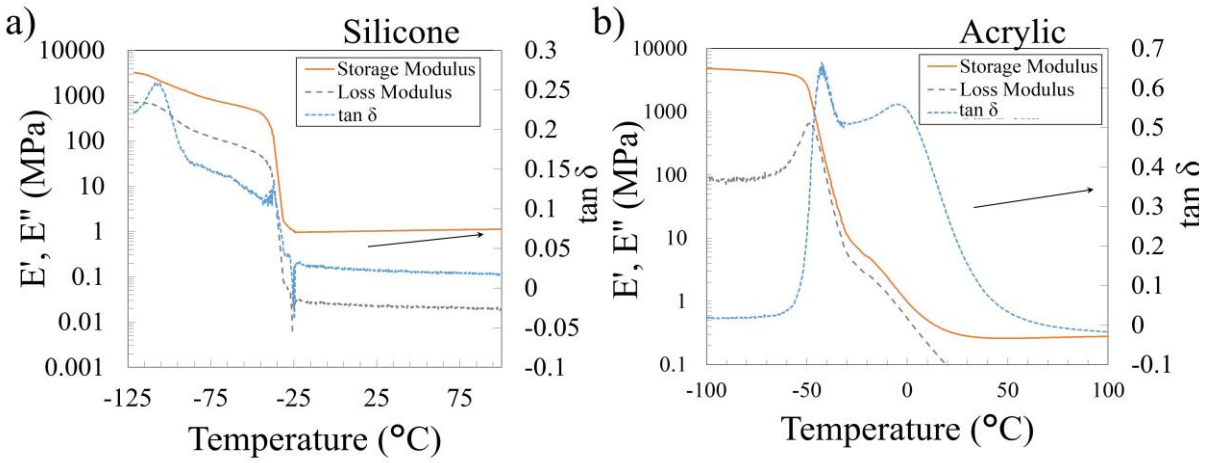

Figure 4-9. Storage modulus, loss modulus, and tan δ versus temperature for a) Silicone elastomer and b) Acrylic elastomer

An optical system was implemented to observe the contact area consisting of a light emitting diode (LED) light source, the Dove prism made of PMMA, and a high-speed camera (FASTCAM APX RS, Photron). The incident angle of the light beam to the contact surface was set to 60^o, larger than the critical angle necessary for the total reflection at the interface between PMMA and air (42^o), resulting in a different light intensity between the contact and the non-contact regions [56-59]. Because of some difficulties such as cohesive failure of the acrylic leaving residue behind and also scaling the normal force due to lever mechanism used, we were not able to obtain meaningful data for contact area versus normal load. However, a screenshot of the high-speed video of the contact for the acrylic shown below illustrate the striking due to cohesive failure of the acrylic.

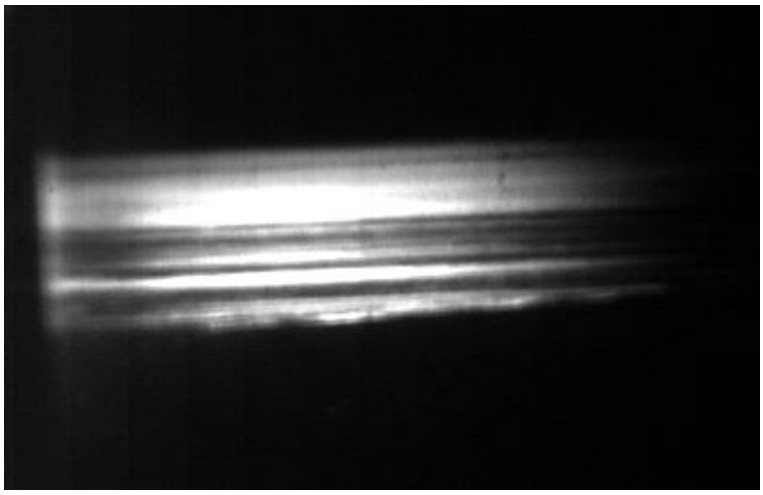

Figure 4-10. Contact area of the acrylic elastomer showing cohesive failure during sliding

Reference

[1] Persson, B.N.J., I.M. Sivebæk, V.N. Samoilov, K. Zhao, A.I. Volokitin, and Z. Zhang, *On the origin of Amonton's friction law.* Journal of physics: condensed matter, 2008. **20**(39): p. 395006.

[2] Dowson, D., *History of tribology*. 1979: Addison-Wesley Longman Limited.

[3] Bowden, F.P. and D. Tabor, *The friction and lubrication of solids*. Vol. 1. 2001: Oxford university press.

[4] Popova, E. and V.L. Popov, *The research works of Coulomb and Amontons and generalized laws of friction.* Friction, 2015. **3**(2): p. 183-190.

[5] Maegawa, S., F. Itoigawa, and T. Nakamura, *Effect of normal load on friction coefficient for sliding contact between rough rubber surface and rigid smooth plane.* Tribology International, 2015. **92**: p. 335-343.

[6] Smith, R.H., *Analyzing friction in the design of rubber products and their paired surfaces*. 2008: CRC press.

[7] Schallamach, A., *The load dependence of rubber friction.* Proceedings of the Physical Society. Section B, 1952. **65**(9): p. 657.

[8] Greenwood, J., H. Minshall, and D. Tabor. *Hysteresis losses in rolling and sliding friction*. in *Proceedings of the Royal Society of London A: Mathematical, Physical and Engineering Sciences*. 1961. The Royal Society.

[9] Grosch, K. *The relation between the friction and visco-elastic properties of rubber*. in *Proceedings of the Royal Society of London A: Mathematical, Physical and Engineering Sciences*. 1963. The Royal Society.

[10] Persson, B., *Sliding friction: physical principles and applications*. 2013: Springer Science & Business Media.

[11] Le Gal, A., X. Yang, and M. Klüppel, *Evaluation of sliding friction and contact mechanics of elastomers based on dynamic-mechanical analysis.* The Journal of chemical physics, 2005. **123**(1): p. 014704.

[12] Moore, D.F., *The friction and lubrication of elastomers*. Vol. 9. 1972: Pergamon.

[13] Barquins, M. and A. Roberts, *Rubber friction variation with rate and temperature: some new observations.* Journal of Physics D: Applied Physics, 1986. **19**(4): p. 547.

[14] Grosch, K., *The rolling resistance, wear and traction properties of tread compounds.* Rubber Chemistry and technology, 1996. **69**(3): p. 495-568.

[15] Dai, Z., S.N. Gorb, and U. Schwarz, *Roughness-dependent friction force of the tarsal claw system in the beetle Pachnoda marginata (Coleoptera, Scarabaeidae).* Journal of Experimental Biology, 2002. **205**(16): p. 2479-2488.

[16] Tambe, N.S. and B. Bhushan, *Scale dependence of micro/nano-friction and adhesion of MEMS/NEMS materials, coatings and lubricants.* Nanotechnology, 2004. **15**(11): p. 1561.

[17] Ford, I., *Roughness effect on friction for multi-asperity contact between surfaces.* Journal of Physics D: Applied Physics, 1993. **26**(12): p. 2219.

[18] Yamada, S. and J. Israelachvili, *Friction and adhesion hysteresis of fluorocarbon surfactant monolayer-coated surfaces measured with the surface forces apparatus.* The Journal of Physical Chemistry B, 1998. **102**(1): p. 234-244.

[19] Zappone, B., K.J. Rosenberg, and J. Israelachvili, *Role of nanometer roughness on the adhesion and friction of a rough polymer surface and a molecularly smooth mica surface.* Tribology Letters, 2007. **26**(3): p. 191.

[20] Yoshizawa, H., Y.L. Chen, and J. Israelachvili, *Fundamental mechanisms of interfacial friction. 1. Relation between adhesion and friction.* The Journal of Physical Chemistry, 1993. **97**(16): p. 4128-4140.

[21] Szoszkiewicz, R., B. Bhushan, B. Huey, A. Kulik, and G. Gremaud, *Correlations between adhesion hysteresis and friction at molecular scales.* The Journal of chemical physics, 2005. **122**(14): p. 144708.

[22] Chaudhury, M.K. and M.J. Owen, *Adhesion hysteresis and friction.* Langmuir, 1993. **9**(1): p. 29-31.

[23] Maeda, N., N. Chen, M. Tirrell, and J.N. Israelachvili, *Adhesion and friction mechanisms of polymer-on-polymer surfaces.* Science, 2002. **297**(5580): p. 379-382.

[24] Kummer, H.W., *Unified theory of rubber and tire friction*. 1966.

[25] James, D., *Measurement of friction between rubber-like polymers and steel.* Journal of Scientific Instruments, 1961. **38**(7): p. 294.

[26] Giles, C., B. Sabey, and K. Cardew. *Development and performance of the portable skid-resistance tester*. in *Symposium on Skid Resistance*. 1962. ASTM International.

[27] West, G. and J. Senior, *Frictional properties of polyethylene.* Wear, 1972. **19**(1): p. 37-52.

[28] Persson, B.N., *On the theory of rubber friction.* Surface Science, 1998. **401**(3): p. 445-454.

[29] Persson, B.N., *Sliding friction: physical principles and applications*. Vol. 1. 2000: Springer Science & Business Media.

[30] Schallamach, A., *How does rubber slide?* Wear, 1971. **17**(4): p. 301-312.

[31] Viswanathan, K., N.K. Sundaram, and S. Chandrasekar, *Stick-slip at soft adhesive interfaces mediated by slow frictional waves.* Soft matter, 2016. **12**(24): p. 5265-5275.

[32] Maegawa, S. and K. Nakano, *Mechanism of stick-slip associated with Schallamach waves.* Wear, 2010. **268**(7): p. 924-930.

[33] Maegawa, S., F. Itoigawa, and T. Nakamura, *Dynamics in sliding friction of soft adhesive elastomer: Schallamach waves as a stress-relaxation mechanism.* Tribology International, 2016. **96**: p. 23-30.

[34] Ludema, K. and D. Tabor, *The friction and visco-elastic properties of polymeric solids.* Wear, 1966. **9**(5): p. 329-348.

[35] Johnson, K.L. and K.L. Johnson, *Contact mechanics*. 1987: Cambridge university press.

[36] Greenwood, J. and J. Williamson. *Contact of nominally flat surfaces*. in *Proceedings of the Royal Society of London A: Mathematical, Physical and Engineering Sciences*. 1966. The Royal Society.

[37] Persson, B.N., *Theory of rubber friction and contact mechanics.* The Journal of Chemical Physics, 2001. **115**(8): p. 3840-3861.

[38] Yang, C. and B. Persson, *Contact mechanics: contact area and interfacial separation from small contact to full contact.* Journal of Physics: Condensed Matter, 2008. **20**(21): p. 215214.

[39] Mori, K., S. Kaneda, K. Kanae, H. Hirahara, Y. Oishi, and A. Iwabuchi, *Influence on friction force of adhesion force between vulcanizates and sliders.* Rubber chemistry and technology, 1994. **67**(5): p. 797-805.

[40] Smith, R., *A Load-Independent, Adhesion-Related Rubber Friction Force?* The Journal of Adhesion, 2011. **87**(11): p. 1112-1123.

[41] Greenwood, J. and D. Tabor, *The friction of hard sliders on lubricated rubber: the importance of deformation losses.* Proceedings of the Physical Society, 1958. **71**(6): p. 989.

[42] Tabor, D., *Friction—the present state of our understanding.* J. Lubr. Technol, 1981. **103**(2): p. 169-179.

[43] Gent, A. and J. Schultz, *Effect of wetting liquids on the strength of adhesion of viscoelastic material.* The Journal of Adhesion, 1972. **3**(4): p. 281-294.

[44] Andrews, E. and A. Kinloch. *Mechanics of adhesive failure. II*. in *Proceedings of the Royal Society of London A: Mathematical, Physical and Engineering Sciences*. 1973. The Royal Society.

[45] Ghatak, A., K. Vorvolakos, H. She, D.L. Malotky, and M.K. Chaudhury, *Interfacial rate processes in adhesion and friction*. 2000, ACS Publications.

[46] Homola, A.M., J.N. Israelachvili, P.M. McGuiggan, and M.L. Gee, *Fundamental experimental studies in tribology: the transition from "interfacial" friction of undamaged molecularly smooth surfaces to "normal" friction with wear.* Wear, 1990. **136**(1): p. 65-83.

[47] Grosch, K., *The relation between the friction and visco-elastic properties of rubber.* Proceedings of the Royal Society of London. Series A. Mathematical and Physical Sciences, 1963. **274**(1356): p. 21-39.

[48] Gent, A. and H. Kim, *Effect of contact time on tack.* Rubber chemistry and technology, 1990. **63**(4): p. 613-623.

[49] Ferry, J.D., *Viscoelastic properties of polymers*. 1980: John Wiley & Sons.

[50] Schallamach, A., *Friction and abrasion of rubber.* Rubber Chemistry and Technology, 1958. **31**(5): p. 982-1014.

[51] Vinogradov, G., A. Yel'kin, G. Bartenev, and S. Bubman, *Effect of normal pressure on temperature and rate dependences of elastomer friction in the glass transition region.* Wear, 1973. **23**(1): p. 33-38.

[52] Stribeck, R., *Kugellager fur beliebige Belastungen.* Zeitschrift des Vereines deutscher Ingenieure, 1901. **45**(3): p. 73-79.

[53] Hamrock, B.J., S.R. Schmid, and B.O. Jacobson, *Fundamentals of fluid film lubrication*. 2004: CRC press.

[54] Lee, C.-G., Y.-J. Hwang, Y.-M. Choi, J.-K. Lee, C. Choi, and J.-M. Oh, *A study on the tribological characteristics of graphite nano lubricants.* International Journal of Precision Engineering and Manufacturing, 2009. **10**(1): p. 85-90.

[55] Zeng, H., N. Maeda, N. Chen, M. Tirrell, and J. Israelachvili, *Adhesion and friction of polystyrene surfaces around T g.* Macromolecules, 2006. **39**(6): p. 2350-2363.

[56] Rubinstein, S.M., G. Cohen, and J. Fineberg, *Detachment fronts and the onset of dynamic friction.* Nature, 2004. **430**(7003): p. 1005-1009.

[57] Rubinstein, S., G. Cohen, and J. Fineberg, *Dynamics of precursors to frictional sliding.* Physical review letters, 2007. **98**(22): p. 226103.

[58] Maegawa, S., A. Suzuki, and K. Nakano, *Precursors of global slip in a longitudinal line contact under non-uniform normal loading.* Tribology Letters, 2010. **38**(3): p. 313-323.

[59] Maegawa, S., F. Itoigawa, and T. Nakamura, *A role of friction-induced torque in sliding friction of rubber materials.* Tribology International, 2016. **93**: p. 182-189.

5 Revisiting the Generalized Scaling Law for Adhesion: Role of Compliance and Extension to Progressive Failure

Ahmad R. Mojdehi[1], Douglas P. Holmes[2], David A. Dillard[1]

[1]Department of Biomedical Engineering and Mechanics, Virginia Tech, Blacksburg, VA 24061

[2]Department of Mechanical Engineering, Boston University, Boston, MA 02215

(Mojdehi, Ahmad R., Douglas P. Holmes, and David A. Dillard. " Revisiting the generalized scaling law for adhesion: role of compliance and extension to progressive failure." *Soft Matter*, (2017), DOI: 10.1039/c7sm01098b.)

Significant recent efforts have been devoted to understanding and mimicking adhesion mechanisms found in many organisms in nature, such as geckos and insects [1-5]. Adhesion failure of bio-inspired adhesive systems has recently been studied, showing that bond strength scales with the square root of the ratio of contact area to the total system compliance ($\sqrt{A/C}$), and its validity has been successfully demonstrated for a broad range of systems [6-11]. This approach is purportedly a simplification of Griffith's classic approach for a set of applicable scenarios involving unstable or catastrophic failure of rate-independent systems. This simplified model, however, appears to differ from the classic fracture mechanics approach, where bond strength should scale with the reciprocal square root of the derivative of the system compliance with respect to the bond area ($\sqrt{\partial A/\partial C}$). This paper will address this apparent discrepancy by examining the roles of both load train and specimen compliances. Fracture mechanics has been widely used in characterizing and analyzing failures in a plethora of applications for decades, including for the analysis of adhesive joints [12-16]. Therefore, a re-examination of the role of system compliance on the performance of adhesive systems and the apparent fundamental discrepancies between the above-mentioned scaling relationships is of significant theoretical and practical importance. This paper revisits the generalized scaling law based on the classical fracture mechanics approach and then explores limitations and applicability of the two scaling relationships.

The effect of adherend and adhesive compliances on the strength of adhesive systems has been widely studied for different applications including shear [17-20], fracture [21], peeling [22-25], pull-off adhesion tests, and Johnson–Kendall–Roberts (JKR) theory [26-29]. Although the proposed scaling law is expected to be applicable to various loading scenarios, in this work we choose to focus on the shear loading example to demonstrate the effect of system compliance on

the shear bond strength of adhesive joints. Without loss of generality, in this example application we will use an analysis consistent with the classic shear lag model introduced by Volkersen [17], which offers a simple framework where the geometry and mechanical properties of both the adhesive and adherends are predicted to significantly affect the shear stress distribution within adhesive lap joints, and thus their resulting strength as well. In general, total system compliance can be expressed as a combination of bond and load train compliances, where load train compliance consists of compliance of free regions (e.g. unbonded region) and machine compliance. The shear lag model offers a means to determine the bond region compliance contribution, which is especially important for joints with high adherend compliance to adhesive compliance ratios.

In the reported scaling relationship for the shear force capacity of elastomer sheet adhesion, the total experimentally-measured compliance of the system in shear loading was implemented in the scaling parameter ($\sqrt{\mathrm{A/C}}$) [6]. This relationship was later employed using theoretically predicted bond compliance by superposing contributions from multiple deformation modes, such as shear deformation, tensile elongation, and even bending within the elastomeric sheet, though the shear lag effect was neglected in the tensile compliance term, effectively assuming uniform shear stress distribution along the bond length [7]. Although not considered therein, the effect of load train compliance on the shear strength of elastomer adhesion was also found to be significant in a few other studies [8, 9]. Furthermore, the role of friction and failure mechanism on the shear adhesion strength of elastomeric strips was studied, and a transition in the failure mechanism, when the elastomer strip's length reaches twice the characteristic shear lag length was observed [30]. This transition was from catastrophic debonding for shorter lengths, where the $\sqrt{\mathrm{A/C}}$ scaling law appeared applicable, to a regime dominated by frictional sliding and progressive detachment for longer lengths, where it is not [30]. Recently, we studied the effect of compliance on the static and kinetic friction of extensible strips where the shear lag model was used to predict the change in friction force with compliance [31].

In this work, we aim to describe the shear force capacity of adhesive bonds in a generalized manner that accounts both catastrophic and progressive failure modes and the role of load train compliance in the resulting force capacity. The $\sqrt{\mathrm{A/C}}$ scaling parameter approach [6] was limited to catastrophic failure and did not explicitly address the role of load train compliance on specimen

failure. Figure 5-1 shows the measured shear force capacity versus $\sqrt{A/C}$ scaling parameter for specimens consisting of a given pressure sensitive adhesive (PSA) tape with different bond areas, number of backing layers, and load train compliances. The PSA tape was chosen for demonstration purposes, offering ease of testing and changing geometrical parameters (see Experiments section for more details), and because of the practical importance of PSAs for many applications. In the derivation of the reported $\sqrt{A/C}$ scaling parameter, the failure mechanism was assumed catastrophic and the critical strain energy release rate was assumed equal to the thermodynamic work of adhesion. However, it was mentioned that this scaling relationship can be applied to more general applications, accounting for various dissipative processes [6].

The mode of failure changed from catastrophic failure to progressive failure when the bond length became greater than a characteristic length scale, *i.e.* $L_c = 2L_{lag}$ (see Supporting Information section for more details). The load train compliance was increased by adding one or more (parallel) springs in series with the adhesive bond. The load train compliance for the case with no spring at the end corresponds to that of machine compliance, which is believed to be very stiff. As seen in Figure 5-1, the shear force capacity vs. $\sqrt{A/C}$ scaling parameter data deviates from a single linear scaling relationship when there is a change in either failure mode or load train compliance. The maximum shear force capacity of the adhesive system did not change when the bond length increased from L_c to higher values (see open markers in Figure 5-1). Furthermore, the slope of the force versus $\sqrt{A/C}$, which is a representative of the interfacial strain energy release rate, changed significantly with different load train compliances, though the bond areas were the same.

In general, increasing load train compliance (by attaching springs or increasing the free length of the tape) tends to increase the slope of the curve, whereas progressive failures results in divergence from the linear relationship, plateauing to the right (as shown by arrows in Figure 5-1). Moreover, we can separate the data into two regions where the bonds lengths are less or more than characteristic length scale (L_c), *i.e.* blue (upper left) and orange (lower right) regions in Figure 5-1, respectively. Therefore, special care needs to be taken when using experimentally measured compliance in $\sqrt{A/C}$ scaling relationship for shear force capacity of different adhesive systems, considering both the load train compliance (including free region compliance of the adhesive system and machine compliance) and the failure mechanisms. The characteristic shear lag length

scale could be of significant practical importance when designing adhesive systems based on the $\sqrt{A/C}$ scaling parameter in order to prevent overestimation of maximum bond strength as shown in Figure 5-1 (see the difference in force capacity between filled triangle markers and open triangle markers). Although the overestimation of bond strength is about a factor of four using the linear fit for catastrophic failure (filled triangles), this difference would have increased indefinitely if bond length was extended further (not possible within machine size limitation). It is worth noting that the $\sqrt{A/C}$ scaling parameter was originally developed to show how the adhesive force capacity of animals scales with their compliance, providing that quantifying and decomposing the body and gripping mechanism compliances is rather difficult, making it necessary to simplify the model in

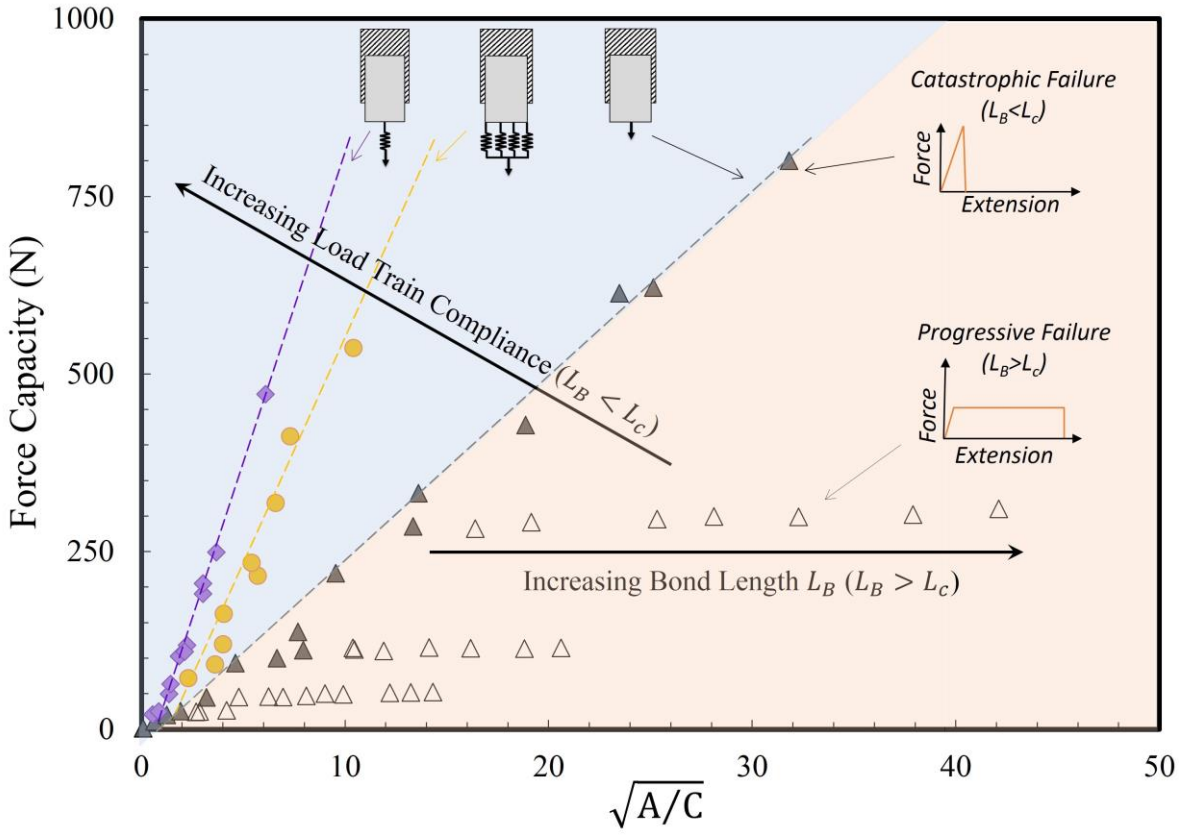

Figure 5-1. Measured shear force capacity versus experimentally determined $\sqrt{A/C}$ of PSA for different values of bond area, backing compliance, and load train compliance. Filled markers and open markers correspond to the $L_B < L_c$ and $L_B > L_c$, respectively. Load train compliance was varied by attaching zero (triangles), one (diamonds), and four (circles) springs at the free end. Dash lines are least square fit of the corresponding filled markers. The arrows show the effects of load train compliance and bond length on the shear force capacity. Blue (upper left) and orange (lower right) regions correspond to the $L_B < L_c$ and $L_B > L_c$, respectively.

order to understand the role of compliance on the animals' capability to adhere on different surfaces. However, the results presented in Figure 5-1 show that the distinctions between the load train compliance and bond compliance are of significant importance and, for systems involving synthetic adhesives, should be measured or quantified.

To address these discrepancies, we implement a classical fracture mechanics approach, considering that the total potential energy of the system (Π) is the sum of the stored elastic energy in the deformed system (U_E) and the energy required to create new surface area (U_S) in a displacement control condition [12]. The linear elastic assumption is generally applicable to viscoelastic materials as long as dissipation is confined to vicinity of the crack tip, which has been shown to be the case for several viscoelastic materials including PSA [6, 32, 33]. Moreover, to demonstrate the validity of this assumption, one can verify that the load-displacement response obtained from the experiment is in agreement with the assumed load-displacement in the linear elastic model [32], which is found to be true for the PSA we used in this study (see force-displacement response in Figure 5-2b and c). Furthermore, loading-unloading experiments were performed for a few specimens, showing that the permanent deformation was less than 10% of the total deformation for loading up to 70% of the failure load and believed to be negligible compared to the linear elastic deformation (see Supporting Information for loading-unloading curves) . The stored elastic energy of the system is $U_E = \mathrm{P}^2\mathrm{C}/2$ and the energy required to create new surface area is $U_S = \mathcal{G}\mathrm{A}$, where P is applied load, C is the system compliance, $\mathcal{G}$ is the strain energy release rate, and A is the bond area. We assume that upon reaching a critical force ($\mathrm{P_C}$) at which the interface separates, the strain energy release rate is equal to the critical strain energy release rate ($\mathcal{G}_\mathrm{C}$), which is an interfacial property related to the materials being bonded and the crack propagation speed. Furthermore, the widely used power-law model can be implemented to take into account the rate-dependent response of the critical strain energy release rate [34] such that $\mathcal{G}_\mathrm{C}=\mathcal{G}_0(v/v_r)^m$, where $\mathcal{G}_0$ is intrinsic strain energy release rate, v is crack propagation velocity, v_r is the reference velocity, and m is a constant related to the rate-dependent material response. The system is in equilibrium such that $\partial\Pi/\partial\mathrm{A} = \partial U_E/\partial\mathrm{A} + \partial U_S/\partial\mathrm{A} = 0$, resulting in the following equation:

$$\mathrm{P_C} = \sqrt{2\mathcal{G}_0}\sqrt{\left(\frac{v}{v_r}\right)^m \frac{\partial \mathrm{A}}{\partial \mathrm{C}}} \tag{5.1}$$

It is worth noting that in the scaling relationship derived above, we did not assume any specific failure mechanism, *e.g.* catastrophic or progressive, during the separation and a mode of fracture. The proposed scaling relationship shows that the maximum force capacity of an adhesive system is related to the intrinsic strain energy of the interface, crack propagation velocity, and reciprocal of the derivative of the compliance of the system with respect to the bond area, and is believed to be applicable to different fracture tests such as shear, peel, and pull-off tests as long as the response is linear elastic.

Now, we focus on the shear mode to demonstrate the application of shear lag model on this scaling relationship. Let us consider an adhesive system comprised of a backing and an adhesive layer bonded to a substrate subjected to a shear load as shown in the Figure 5-2a. The shear lag concept for a single lap adhesive joint [17] is used to derive a closed-form relationship for the compliance of the bonded region, considering the adhesive and backing layer and substrate. Figure 5-2a shows a differential element of the entire thickness and the corresponding stresses on the backing layer, adhesive, and substrate. The governing differential equation is obtained from the equilibrium condition of a differential element adhered to a rigid substrate,

$$\delta'' - \lambda^2 \delta = 0 \tag{5.2}$$

in which the prime denotes an ordinary derivative with respect to *x*, $\lambda = 1/L_{lag} = \sqrt{G/Eh_A h_B}$ is the inverse of a characteristic length obtained from the material properties and geometry of the system: h_A is the thickness of the adhesive layer, h_B is the thickness of the backing layer, E is the Young's modulus of the backing layer, and G is the shear modulus of the adhesive, as shown in Figure 5-2a.

Equation (5.2) has the following solution for the displacement $\delta(x)$ after enforcing $\delta'(x) = \mathrm{P}/Eh_B w$ and $\int_0^{L_B} Gw\delta(x)/h_A \, dx = \mathrm{P}$ boundary conditions, which correspond to the end load in the backing and force equilibrium condition, respectively.

$$\delta(x) = \frac{h_A \lambda \mathrm{P}}{wG} \frac{\mathrm{Cosh}(\lambda x)}{\mathrm{Sinh}(\lambda L_B)} \tag{5.3}$$

where w is the width of the adhesive and backing layers, P is the applied load, and L_B is the bond length.

The axial compliance of bonded region at $x = L_B$ can be obtained by differentiating displacement with respect to the applied load as $C_B = (h_A \lambda / wG)\ Coth(\lambda L_B)$. Moreover, the compliance of the free region is obtained from the compliance of a tensile member, neglecting the tensile stiffness of the adhesive, as $C_F = L_F / E h_B w$. The load train compliance can be defined as $C_L = C_F + C_M$, where C_M refers to the machine compliance.

Considering the bonded region, free region, and machine compliance as three springs connected to each other in series, we can find the total compliance of the system as $C = C_B + C_F + C_M$. Finally, we can differentiate the system compliance with respect to the bond area and calculate the scaling parameter as:

$$\frac{\partial \mathrm{A}}{\partial \mathrm{C}} = \frac{E h_B w^2 \mathrm{Sinh}^2(\lambda L_B)}{1 + \mathrm{Sinh}^2(\lambda L_B)} \tag{5.4}$$

To understand the shear stress distribution along the length of the adhesive, we implemented the digital image correlation (DIC) technique to calculate the variation in shear stress along the PSA tape. Figure 5-2b and c show the force-displacement response of 1-layer and 3-layer PSA tapes of the same length, and the corresponding displacement field contour at different loads. The displacement field was measured by tracking local displacements of the speckles, and then the shear strain field was calculated by dividing the displacement by the thickness of the adhesive layer. Subsequently, the shear stress was calculated using the linear constitutive relation between shear stress and shear strain. The non-uniform distribution of the axial displacement, which is proportional to the shear strain and shear stress, along the length of the tapes is apparent in the contour images shown in Figure 5-2b. Moreover, we see two different failure mechanisms for 1-layer and 3-layer tapes, namely progressive and catastrophic failures. In progressive failure, the debonding front propagates along the length of the tape in the negative x direction, whereas in catastrophic failure complete debonding occurs suddenly upon reaching the peak load. Good agreement is found, as shown in Figure 5-2d, between the experimental data and the shear lag fit

for shear stress distribution along the length of the tape (at the centerline). Both the experiments and shear lag model confirm the exponential decay of the shear stress from the loading point to the end. In addition, Figure 5-2d demonstrates the effect of backing layer stiffness on the shear stress distribution along the length of the adhesive, *i.e.* the variation of shear stress across the length of the adhesive is higher (about four times the average shear stress) for the soft backing (1-layer tape) compared to the stiff backing (3-layer tape) case (about an average shear stress).

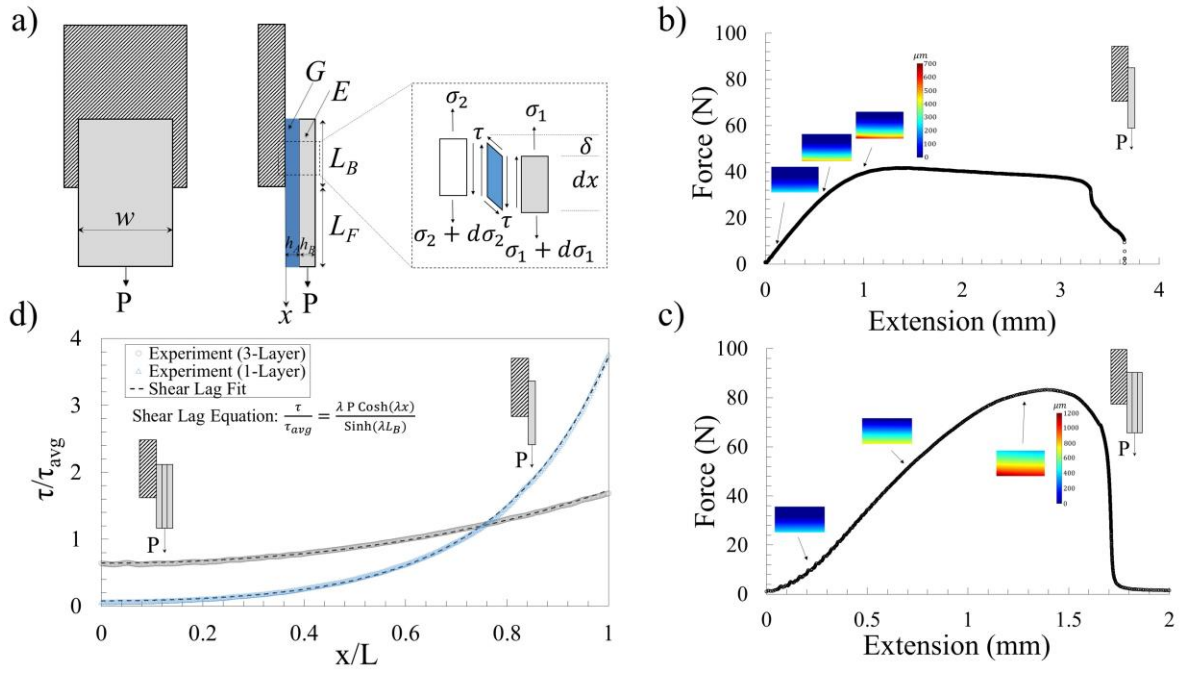

Figure 5-2. a) Schematic of adhesive system, the corresponding material properties and geometry for the adhesive and backing layers, and a differential element at the contact interface. Force versus extension for a single layer of PSA tape (b) and three layers of PSA tape (c), and sequences of displacement field at corresponding loading condition obtained from DIC. d) Normalized shear stress on adhesive layer along the length of the tape for 1- and 3-layers PSA tapes obtained from DIC (markers) and fitted using shear lag model (dash line). Samples geometry and material properties: L=10mm, G/h_A=8541 MPa/m, Eh_B=0.215 MPa.m

Since we have developed a closed-form relationship for the total system compliance based on the shear lag analysis, we can simply compare the scaling relationship based on $\sqrt{\mathrm{A}/\mathrm{C}}$ with the model presented in this paper that is based on $\sqrt{\partial \mathrm{A}/\partial \mathrm{C}}$ (assuming constant crack propagation rate, i.e. $v/v_r = 1$) to show conditions where these two scaling relationships deviate from each other (see supporting information for details of the conditions). There are two conditions where these two models deviate from each other significantly: 1) changing the load train compliance (by changing

either the free region or machine compliances), and 2) increasing the bond length to greater than twice the characteristic shear lag length (L_{lag}). Therefore, the characteristic bond length scale where we observed a transition from catastrophic to progressive failure in Figure 5-1 is found to be the characteristic shear lag length scale ($L_c = 2L_{lag}$). Based on the linear elastic fracture mechanics (LEFM) approach the strain energy release rate should not be a function of the load train compliance as once the specimen breaks, it is only the stored energy in the vicinity of the crack (near-field) that drives the failure [16], one may argue that the change in the load train compliance would effectively change the crack propagation velocity, and therefore the critical strain energy release rate for viscoelastic materials. Nevertheless, as shown in Figure 5-1, the strain energy release rate (the slope of the curve) increased by increasing the load train compliance (*i.e.* lower crack propagation rate), which is not consistent with a typical viscoelastic material response in rubbery region, showing the change in the slope is not from rate dependent material response. In other words, the change in the slope would be even more significant if the crack propagation velocity was not affected by the load train compliance. Gilman *et al.* [8] investigated the mechanics of gecko adhesion by performing a model shear experiment on fabric-backed elastomer with attached springs of variable compliance, showing that the load train compliance plays an important role on the maximum adhesive force of the system. However, this effect was justified by the $\sqrt{\mathrm{A/C}}$ scaling parameter, as the load train compliance would directly affect the total system compliance used in this scaling relationship. Moreover, King *et al.* [9] evaluated important geometric parameters affecting the adhesive force capacity showing the compliance of the adhesive far from the interface, *i.e.* free region's compliance, still influences maximum shear force capacity of adhesive systems, though not as significant as its effect on $\sqrt{\mathrm{A/C}}$ scaling parameter. It has been argued that this slight dependence of force capacity on free length is due to failure mechanism of the adhesives, as longer free length results in predominantly pure shear deformation while shorter free lengths can lead to deviation from a lap shear test to a peel test at larger loading angles [9].

Let us consider a very simple catastrophic failure case, where the shear stress distribution can be approximated as uniform, corresponding to a rigid backing on the adhesive layer. Therefore the bond compliance will be reduced to the adhesive layer compliance resulting from shear deformation of the adhesive layer ($\mathrm{C_B = h_A/GA}$). The system compliance is $\mathrm{C = C_B + C_L}$, where $\mathrm{C_L}$ is the load train compliance. Subsequently, $\partial \mathrm{C}/\partial \mathrm{A} = \mathrm{C_B/A} = \mathrm{h_A/GA^2}$ and therefore $\partial \mathrm{C}/\partial \mathrm{A}$

approaches to C/A if C_L is negligible compared to C_B. Consequently, the agreement shown with the $\sqrt{A/C}$ prediction for the force capacity of synthetic and animal adhesive pads [6] might be a bit fortuitous due to small variation in the load train compliance to bond compliance ratio (C_L/C_B), as log-log scales over several order of magnitudes were used to present the data making it difficult to distinguish the deviation (see Supporting Information for more details). Figure 5-3a and b exhibit the effect of load train compliance on schematic illustrations of force versus extension curves for the two scaling approaches. The force capacity, based on the $\sqrt{A/C}$ scaling parameter, decreases by increasing the load train compliance, as it assumes all the energy stored in the system, i.e. in the specimen and load train, contributes to the debonding process. However, based on the classic fracture mechanics approach, it is only the stored energy in the specimen in the vicinity of the crack that drives the debonding. For example, based on classic Griffith's approach for an infinite specimen with a crack, the change in specimen's compliance in the vicinity of the crack dictates the force capacity of the system regardless of the size of the specimen. Furthermore, changes in the two scaling parameters as a function of bond length and free length are illustrated in Figure 5-3c and d, respectively. Three regions defined in Figure 5-3c correspond to the uniform shear stress distribution and catastrophic failure regime (I), non-uniform shear stress distribution and catastrophic failure regime (II), and non-uniform shear stress distribution and progressive failure regime (III). Region I is where the two scaling parameters are identical as mentioned above for the case of catastrophic failure with uniform shear stress distribution. The two scaling approaches significantly deviate from each other about $L_B = 2L_{lag}$ where the failure mode changes from catastrophic to progressive failure and also with increase in the free length. In order to prevent any confusion when using experimentally measured $\sqrt{A/C}$ scaling parameter, the load train compliance should be separated from the bond compliance. Overall, the role of load train compliance (either free length or machine compliance) on the crack propagation velocity, which seems to be the main contribution of the load train on the adhesive shear force capacity, has been ignored in the gecko-inspired adhesion literature.

In addition, the transition in failure mode from catastrophic to progressive failure is mainly due to the exponential decay in the shear stress along the length of the adhesive that is predicted by the shear lag model. In other words, the portion of adhesive located far from the loading point (for the bond length longer than $2L_{lag}$) effectively does not sense the shear stress, resulting in a bond

length-independent maximum shear force capacity, and also progressive failure for long tapes. For this case, we observed a progressive failure where a debonding front propagates along the length of the adhesive up to a point where the bond length approaches $2L_{lag}$, whereupon complete debonding occurs. The transition from catastrophic to progressive failure at $2L_{lag}$ bond length is consistent with the experimentally observed transition length scale for the elastomeric strips [30]. However, the mentioned transition length scale can be obtained from the shear lag model where

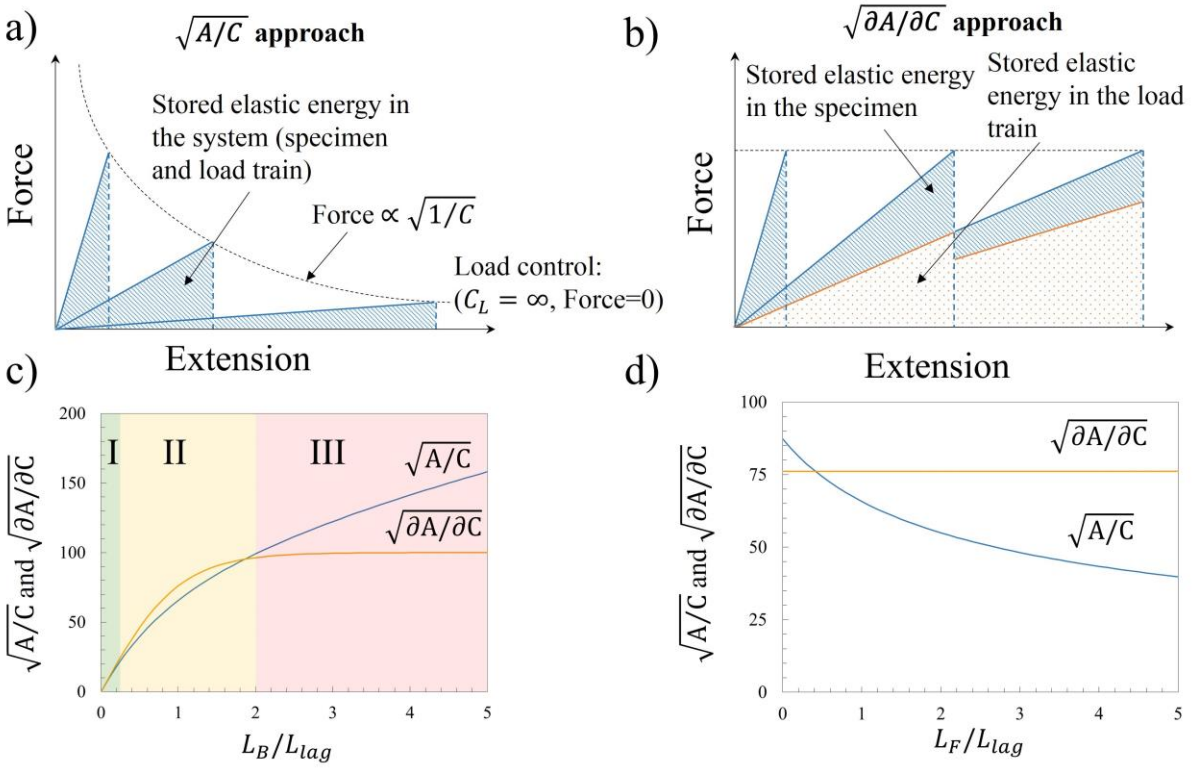

Figure 5-3. Schematic illustrations of force versus extension based on a) $\sqrt{\mathrm{A/C}}$ approach and b) $\sqrt{\partial \mathrm{A}/\partial \mathrm{C}}$ approach for different load train compliances; Comparison of the two scaling parameters, obtained from the closed-form solution, c) with changes in the bond length and d) free length. Three regions defined in (c) correspond to the uniform shear stress distribution and catastrophic failure regime (I), non-uniform shear stress distribution and catastrophic failure regime (II), and non-uniform shear stress distribution and progressive failure regime (III). The two scaling parameters are identical in regime (I), slightly different in regime II, and substantially different in regime III. The failure mode changes from catastrophic to progressive around $L_B = 2L_{lag}$ (border of regime II and III). The $\sqrt{\partial \mathrm{A}/\partial \mathrm{C}}$ scaling parameter is independent of free length/load train compliance (d).

there is a change in the slope of $\sqrt{\partial \mathrm{A}/\partial \mathrm{C}}$ versus L_B/L_{lag} plot (see Figure 5-3d and supporting information for more details).

Now we use our proposed scaling relationship shown in Equation (5.1) together with the closed-form relationship derived for $\partial \mathrm{A}/\partial \mathrm{C}$ shown in Equation (5.4) to show how the shear force capacity changes with different conditions such as catastrophic and progressive failures, variation in the load train compliance, and rate of crack propagation. Figure 5-4a shows the same shear force capacity data plotted on Figure 5-1, but as a function of the theoretical $\sqrt{\partial \mathrm{A}/\partial \mathrm{C}}$. There is a slight difference between the data obtained from different load train compliance, *i.e.* those with more compliant load train have lower shear force capacity compared to the ones with less compliant load train. However, the data for different failure mechanisms, *i.e.* catastrophic (filled markers) and progressive failure (open markers), do not show divergence from the linear curve as shown in Figure 5-4a. Although, as discussed before, the load train compliance should not directly affect the critical strain energy release rate of the interface, it can influence the crack propagation velocity such that adhesives with more compliant load train will experience lower crack propagation velocity and vice versa. Assuming a linear relationship between the displacement and load train compliance results in $v/v_r = C_r/C_L$, where subscript r refers to a reference configuration (crack propagation velocity is assumed to scale with $v = (C_r/C_L)v_r$ to maintain the rate of change in force capacity of specimen nominally constant for linear elastic response). In order to find the constant m in Equation (5.1), we performed shear tests at different displacement rates for a single bond area and plotted the critical strain energy release rate versus displacement rate on a log-log scale, as shown in Figure 5-4b. The slope of this curve corresponds to m and is found to be 0.42 for the type of PSA used in this experiment. In addition, the rate dependent response of $\mathcal{G}_c$ was independently measured in 90 degree peel tests at different displacement rates and the results were consistent (m=0.4) with that of shear test (see Supporting Information for the peel test results). Finally, when we use the revisited generalized scaling relationship considering the effects of both rate and non-uniform shear stress distribution, all the data for various conditions and geometries collapse onto a single linear curve, as shown in Figure 5-4c. Therefore, no matter which failure mechanism, load train compliance of the adhesive system, the revisited generalized scaling law proposed in this work can be used to predict the shear force capacity of the adhesive systems. It is worth noting that in our analysis we assumed linear elastic deformation in both fracture mechanics

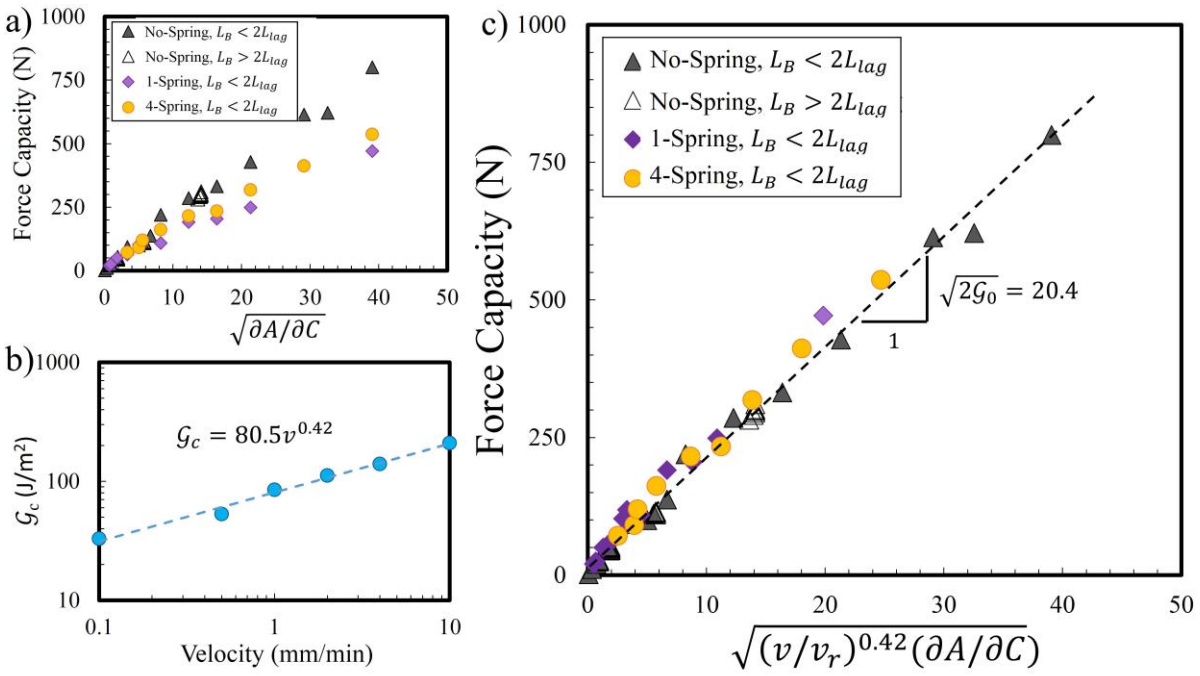

Figure 5-4. a) Measured shear force capacity versus theoretical $\sqrt{\partial A/\partial C}$ of PSA for different values of bond area, system compliance, and load train compliance. Filled markers and open markers correspond to the $L_B/L_{lag} < 2$ and $L_B/L_{lag} > 2$, respectively. Load train compliance was varied by attaching zero (triangles), one (diamonds), and four (circles) springs at the free end. b) Critical strain energy release rate versus crack propagation velocity of PSA in log-log scale (markers) and the corresponding power-law fit (dash line). Constant m is obtained from the slope and found to be 0.42 c) Measured shear force capacity versus revisited generalized scaling parameter $\sqrt{(v/v_r)^m(\partial A/\partial C)}$ for the same data in (a) and the corresponding least square fit (dash line). Reference velocity (v_r) corresponds to the case without any spring at the free end at 10 mm/min.

approach and shear lag model, making this scaling relationship only applicable when the deformation in the adhesive and backing is linearly elastic, and there is no other forms of dissipation such as plastic deformation and frictional sliding. Based on these assumptions, we would expect the force-displacement curve to linearly increase and then suddenly drop (for the catastrophic failure) or plateau (for the progressive failure) after initiation of the debonding. Moreover, observing any divergence from initial linear relationship before the peak force could suggest deviation from the assumptions made for this model. Although the proposed scaling relationship has limitations for complex systems such as multi-material interfaces and complex geometry, where a closed form solution of $\partial A/\partial C$ is not available, the scaling parameter could possibly be experimentally obtained by measuring the compliance and crack propagation length

for the progressive failure case as has been done in the classic fracture mechanics studies for a long time both experimentally and numerically [35, 36], and measuring the compliances of multiple bond areas and calculate the $\sqrt{\partial A/\partial C}$ from the slope of the compliance versus bond area curve, for the case of catastrophic failure. The developed scaling relationship is believed to be applicable to other adhesive systems such as time to fail in shear dead load tests of PSAs, effect of adhesive and thickness on the bond strength, and patterned interfaces using the principle of superposition to predict the shear force capacity of bio-inspired adhesives, which need to be evaluated in a separate study and is beyond the scope of this work.

In conclusion, the generalized scaling relationship developed based on the $\sqrt{A/C}$ is revisited using the classical fracture mechanics approach and the shear lag model. A closed-form relationship for the system compliance has been derived based on the concept of shear lag model, and experimentally confirmed using DIC technique. We found two dominant failure mechanisms, *i.e.* catastrophic and progressive, that depend on the relative length of the bond with respect to a characteristic length scale obtained from the shear lag concept. The proposed model has been compared with the one reported in the literature for scaling the adhesion of elastomers, and the conditions where two models deviate from each other are discussed. The originally reported scaling relationship based on the $\sqrt{A/C}$ approach does not distinguish the load train compliance from the experimentally measured system compliance, which appears to differ with the classical fracture mechanics approach. Although the load train compliance (free region and machine compliances) is found to affect the force capacity of the adhesive system, we believe the apparent load train compliance effect enters indirectly through the viscoelastic nature of the materials tested, rather than directly because of the load train compliance, Again the stored elastic energy in the load train cannot continue to drive failure once the specimen breaks and it is only local energy that can feed debonding, based on the concepts of fracture mechanics. A power-law model is implemented to take into account the rate dependent response of the critical strain energy release rate of the interface. We showed that our proposed model works for both catastrophic and progressive failure mechanisms, and also different load train compliances, or crack propagation rates. The scaling relationship proposed in this study could help to better understand the role of system compliance and geometry on the performance of adhesive systems subjected to shear loading, providing a fundamental basis for optimizing and efficiently designing adhesive systems.

Experiments

Lap Shear Test: The shear force capacity of the PSA (Duck HP260 packaging tape, ShurTech Brands LLC., Avon, OH) bonded to a poly(methyl methacrylate) (PMMA) substrate in lap shear configuration (see Figure 5-2) was measured at a displacement rate of 10 mm/min. using an Instron 5800 tensile test machine. PSA strips of different lengths (ranging from 2 mm to 180 mm) and widths (ranging from 2 mm to 50 mm) were attached to the PMMA by applying a nominally uniform pressure along the length and making sure that the adhesives made complete contact with the substrate. The substrate was cleaned with 91% isopropyl alcohol before each test. The compliance of the backing layer was effectively changed by attaching multiple layers of PSA on the top of each other [37]. A maximum of three layers of the same packaging PSA tape were used while, in order to reach much lower backing compliance, up to two layers of aluminum tape (3M 2542 Vibration Damping Tape, Minneapolis, MN) were used as backing layer on top of other tapes. The force and displacement were recorded throughout the experiment and the maximum force was used for the shear force capacity of each specimen.

Digital Image Correlation (DIC): Speckle patterns were applied to the PSA backing using black spray paint. The displacements of the speckles were recorded throughout the experiment using a DSLR camera (Nikon D7000). Images of the sample before and after deformation were given as inputs to an open-source Matlab DIC software [38] and the DIC analysis was performed according to the user manual to obtain the displacement field and calculate the effective shear strain and stress distributions along the length of the PSA.

Acknowledgements

The authors would like to thank the Provost's Office and College of Engineering for partial support of ARM, the Biomedical Engineering and Mechanics (BEAM) Department for use of equipment, and the Macromolecules and Interfaces Institute at Virginia Tech for fostering interdisciplinary research in polymer and adhesion science. DPH acknowledges funding from the NSF CAREER CMMI-1454153.

Supporting Information

Before comparing the scaling parameter developed by Bartlett *et al.* [6] with our proposed scaling parameter, it would be beneficial to go over the assumptions that are made leading to $\sqrt{\mathrm{A/C}}$ scaling

parameter. First, it is assumed that the system is in equilibrium such that $\partial\Pi/\partial A = 0$, where Π is the total energy of the system and A is bond area. Second, it is assumed that upon reaching a critical force the interface will separate in an unstable manner in a single step such that $\partial^2\Pi/\partial A^2 < 0$. Finally, the system is assumed to conserve energy leading to a catastrophic failure where any change is larger than the system size. Owing to the third assumption, the derivative of system energy is reduced to the algebraic expression leading to $\sqrt{A/C}$ instead of $\sqrt{\partial A/\partial C}$.

Now that we have a closed-form solution for the system compliance, we can compare two scaling parameters (assuming constant crack propagation velocity) to show in what conditions these two scaling relationships deviate from each other. Here are the expressions for the two scaling parameters:

$$\frac{A}{C} = \frac{wL_B}{\frac{h_A\lambda}{wG}Coth(\lambda L_B) + \frac{L_F}{E\,h_B w} + C_M} \tag{S5.1}$$

$$\frac{\partial A}{\partial C} = \frac{Eh_B w^2 Sinh^2(\lambda L_B)}{1 + Sinh^2(\lambda L_B)} \tag{S5.2}$$

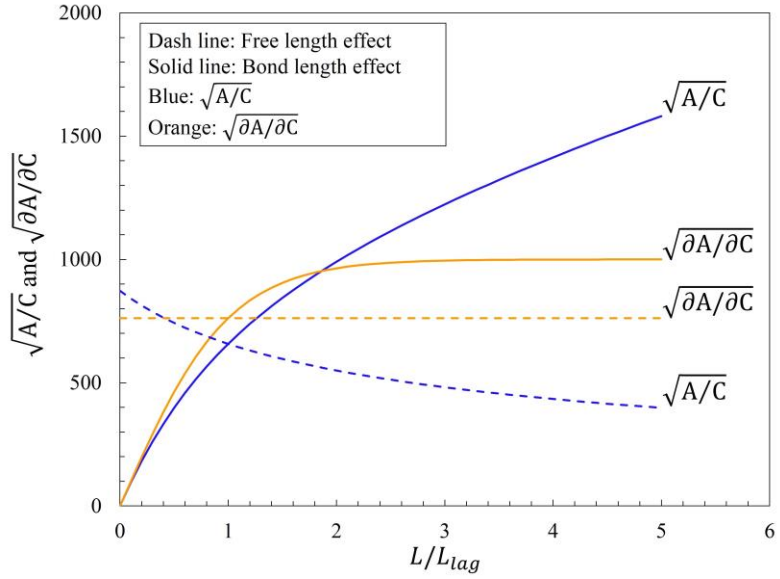

Figure 5-5. Changes in $\sqrt{A/C}$ and $\sqrt{\partial A/\partial C}$ as a function of normalized length. Dash line refers to free length effect. The solid line corresponds to the bond length effect. Blue and orange colors refer to $\sqrt{A/C}$ and $\sqrt{\partial A/\partial C}$, respectively.

First, we can find that $\sqrt{\mathrm{A}/\mathrm{C}}$ is a function of free length (L_F) and machine compliance (C_M) whereas $\sqrt{\partial\mathrm{A}/\partial\mathrm{C}}$ is not. As seen in Figure 5-1, $\sqrt{\mathrm{A}/\mathrm{C}}$ decreases as the ratio of free length over shear lag characteristic length (L_F/L_{lag}) increases, which is due to the added compliance from the free length. On the other hand, $\sqrt{\partial\mathrm{A}/\partial\mathrm{C}}$ does not change as the free length or machine compliance increases. Therefore, we would expect a higher slope of maximum shear force capacity versus $\sqrt{\mathrm{A}/\mathrm{C}}$ for the samples with higher load train compliance (longer free length or softer testing machine), while the slope is not expected to change when the force capacity is plotted as a function of $\sqrt{\partial\mathrm{A}/\partial\mathrm{C}}$. Moreover, Figure 5-1 depicts the change in $\sqrt{\mathrm{A}/\mathrm{C}}$ and $\sqrt{\partial\mathrm{A}/\partial\mathrm{C}}$ as a function of the ratio of bond length over shear lag characteristic length (L_B/L_{lag}) while the L_F and C_M are kept constant. It is clear that around the bond length twice the characteristic length, we see a deviation

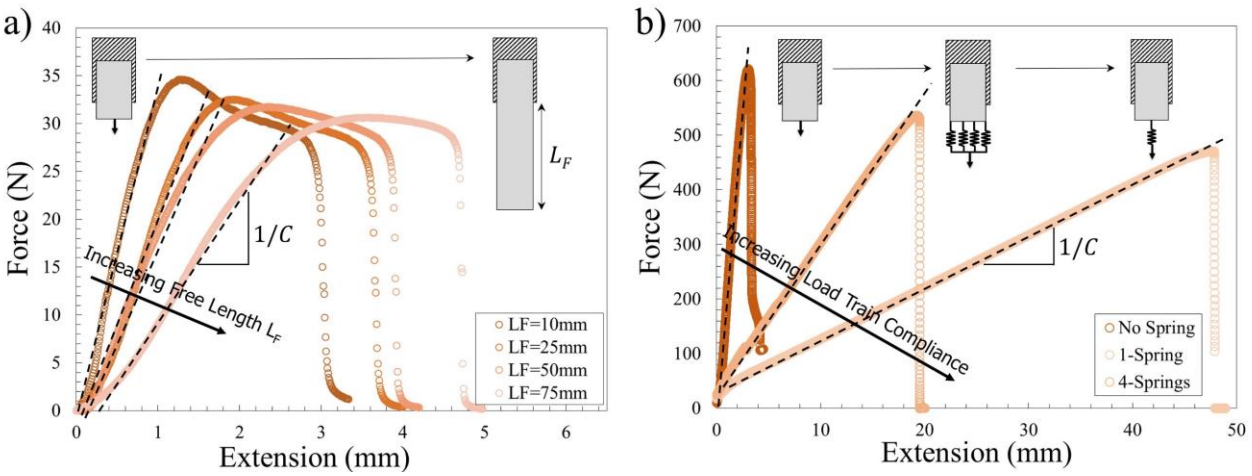

Figure 5-6. Force versus extension curves of PSA for a) different values of free length L_F and b) different load train compliances

between $\sqrt{\mathrm{A}/\mathrm{C}}$ and $\sqrt{\partial\mathrm{A}/\partial\mathrm{C}}$ approaches. Interestingly, it is close to the length scale in which the transition from catastrophic to progressive failures occurs. Overall, there are two conditions at which we would expect the two models deviate from each other: (I) By increasing the load train compliance (by increasing the free length or machine compliance), (II) by transition from catastrophic failure to progressive failure.

Figure 5-6 exhibits the force versus displacement curves for the PSA tapes with the same bond area, but different free lengths. The total system compliance increases significantly by increasing the free length, while there is a slight change in the maximum force of the PSA tapes. The change

in the maximum force is due to the viscoelastic response of the PSA, as by changing the free length the displacement rate changes, giving rise to the rate dependent response of the PSA.

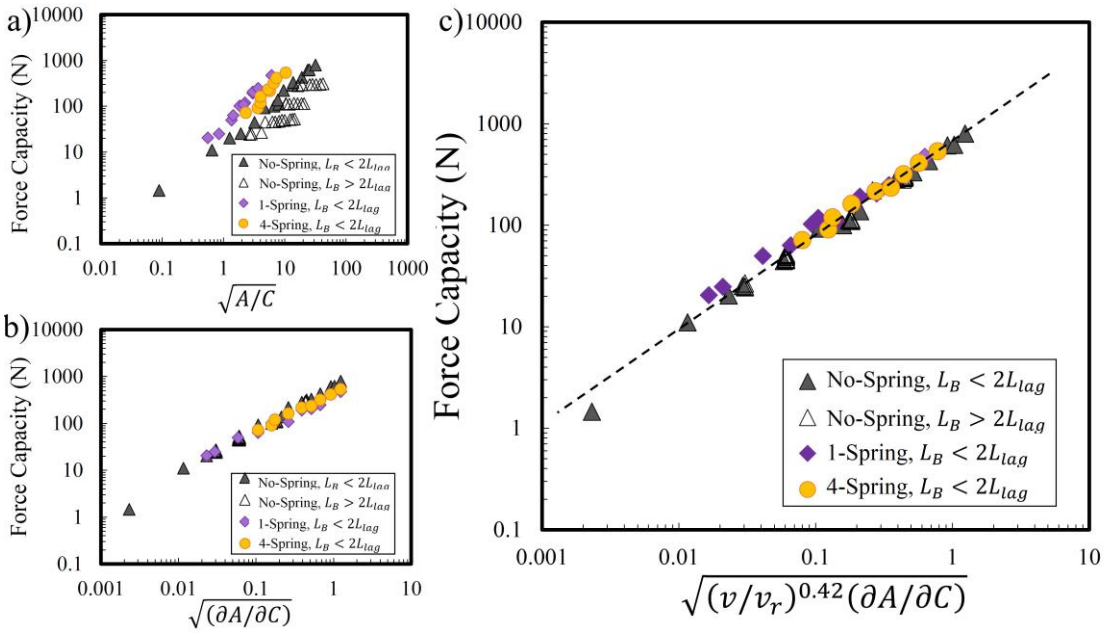

Figure 5-7. Measured shear force capacity versus: a) experimental $\sqrt{A/C}$ scaling parameter b) theoretical $\sqrt{\partial A/\partial C}$ scaling parameter without considering rate effect c) theoretical scaling parameter including rate effect in log-log scale.

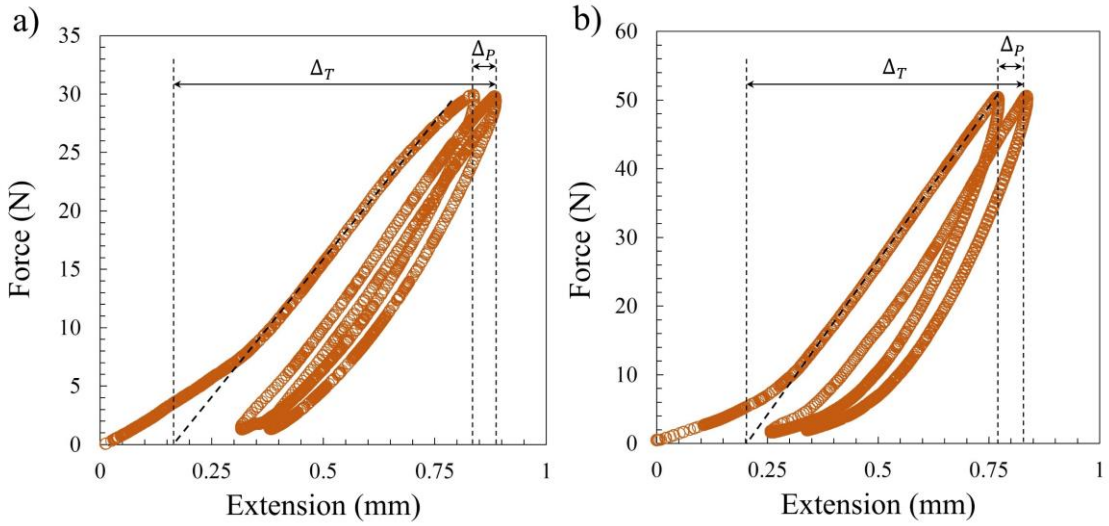

Figure 5-8. Loading-unloading curve for a1-layer of PSA tape b) 3-layers of PSA tape and the corresponding permanent (Δ_P) and total deformations (Δ_T)

Figure 5-7 shows the data in Figure 5-1a, Figure 5-4a, and Figure 5-4c in the paper on the log-log scale to demonstrate how many orders of magnitude shear force capacity were tested. Furthermore, as seen in Figure 5-7, when a log-log scale is used the data appeared to be less scattered compared to the linear scale. Furthermore, there is no distinct difference for the data with different load train compliance shown in Figure 5-7b, showing that using the data in log-log scale may not illustrate the detailed differences between data points.

Figure 5-8 exhibits the loading-unloading results for the PSA, showing that the permanent deformation was less than 10% of the total deformation ($\Delta_P/\Delta_T = 7\%$ for 1-layer and 9.5% for 3-layers of PSA tapes) for loading up to 70% of the failure load and believed to be negligible compared to the linear elastic deformation. This also support the linear elastic assumption made in derivation of the scaling parameter based on the fracture mechanics approach.

Furthermore, the rate-dependent response of strain energy release rate was obtained by performing 90 degree peel tests at different peeling velocities to independently calculate the power m in equation (1) in the paper. Figure 5-9 demonstrates the results for $\mathcal{G}_c$ versus peel rate, which is consistent with that of shear test (m=0.42 in shear versus m=0.4 in 90 degree peel test).

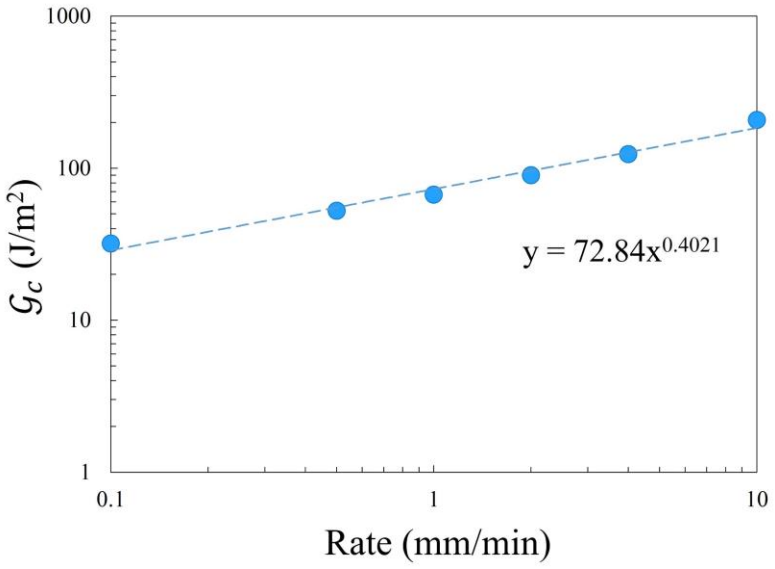

Figure 5-9. Critical strain energy release rate versus crack propagation velocity of PSA in log-log scale (markers) and the corresponding power-law fit (dash line) obtained from 90 degree peel test. Constant m is obtained from the slope and found to be 0.4, consistent with that of shear test.

References

[1] Autumn, K., et al., *Adhesive force of a single gecko foot-hair.* Nature, 2000. **405**(6787): p. 681-685.

[2] Russell, A.P., *Integrative functional morphology of the gekkotan adhesive system (Reptilia: Gekkota).* Integrative and Comparative Biology, 2002. **42**(6): p. 1154-1163.

[3] Niederegger, S. and S.N. Gorb, *Friction and adhesion in the tarsal and metatarsal scopulae of spiders.* Journal of Comparative Physiology A, 2006. **192**(11): p. 1223-1232.

[4] Gorb, S., Y. Jiao, and M. Scherge, *Ultrastructural architecture and mechanical properties of attachment pads in Tettigonia viridissima (Orthoptera Tettigoniidae).* Journal of Comparative Physiology A, 2000. **186**(9): p. 821-831.

[5] Majidi, C., et al., *High friction from a stiff polymer using microfiber arrays.* Physical review letters, 2006. **97**(7): p. 076103.

[6] Bartlett, M.D., et al., *Looking Beyond Fibrillar Features to Scale Gecko-Like Adhesion.* Advanced Materials, 2012. **24**(8): p. 1078-1083.

[7] Bartlett, M.D., A.B. Croll, and A.J. Crosby, *Designing Bio-Inspired Adhesives for Shear Loading: From Simple Structures to Complex Patterns.* Advanced Functional Materials, 2012. **22**(23): p. 4985-4992.

[8] Gilman, C.A., et al., *Geckos as springs: Mechanics explain across-species scaling of adhesion.* PloS one, 2015. **10**(9): p. e0134604.

[9] King, D.R. and A.J. Crosby, *Optimizing adhesive design by understanding compliance.* ACS applied materials & interfaces, 2015. **7**(50): p. 27771-27781.

[10] King, D.R., et al., *Creating Gecko-Like Adhesives for "Real World" Surfaces.* Advanced Materials, 2014. **26**(25): p. 4345-4351.

[11] Bartlett, M.D. and A.J. Crosby, *High capacity, easy release adhesives from renewable materials.* Advanced Materials, 2014. **26**(21): p. 3405-3409.

[12] Griffith, A.A., *The phenomena of rupture and flow in solids.* Philosophical transactions of the royal society of london. Series A, containing papers of a mathematical or physical character, 1921. **221**: p. 163-198.

[13] Dillard, D.A., *Advances in structural adhesive bonding*. 2010: Elsevier.

[14] Brussat, T., S. Chiu, and S. Mostovoy, *Fracture mechanics for structural adhesive bonds*. 1977, DTIC Document.

[15] Chaves, F.J., et al., *Fracture mechanics tests in adhesively bonded joints: a literature review*. The Journal of Adhesion, 2014. **90**(12): p. 955-992.

[16] Williams, J.G., *Fracture mechanics of polymers*. 1984: Horwood.

[17] Volkersen, O., *Die Nietkraft Verteilung in zugbeanspruchten Nietverbindungen mit konstanten Laschenquerschnitten.* Luftfahrtforschung, 1938. **15**: p. 41-47.

[18] Hart-Smith, L., *Adhesive-bonded double-lap joints*. 1973: National Aeronautics and Space Administration.

[19] Kendall, K., *Crack propagation in lap shear joints.* Journal of Physics D: Applied Physics, 1975. **8**(5): p. 512.

[20] Lai, Y.-H., M.D. Rakestraw, and D.A. Dillard, *The cracked lap shear specimen revisited—a closed form solution.* International Journal of Solids and Structures, 1996. **33**(12): p. 1725-1743.

[21] Anderson, G.P., S.J. Bennett, and K.L. DeVries, *Analysis and Testing of Adhesive Bonds*. 1977, New York: Academic Press.

[22] Kendall, K., *Thin-film peeling-the elastic term.* Journal of Physics D: Applied Physics, 1975. **8**(13): p. 1449.

[23] Kaelble, D., *Theory and analysis of peel adhesion: bond stresses and distributions.* Transactions of The Society of Rheology (1957-1977), 1960. **4**(1): p. 45-73.

[24] Begley, M.R., et al., *Peeling of a tape with large deformations and frictional sliding.* Journal of the Mechanics and Physics of Solids, 2013. **61**(5): p. 1265-1279.

[25] Collino, R.R., et al., *Detachment of compliant films adhered to stiff substrates via van der Waals interactions: role of frictional sliding during peeling.* Journal of The Royal Society Interface, 2014. **11**(97): p. 20140453.

[26] Kim, S., et al., *Effect of backing layer thickness on adhesion of single-level elastomer fiber arrays.* Applied Physics Letters, 2007. **91**(16): p. 161905.

[27] Shull, K.R., D. Ahn, and C.L. Mowery, *Finite-size corrections to the JKR technique for measuring adhesion: soft spherical caps adhering to flat, rigid surfaces.* Langmuir, 1997. **13**(6): p. 1799-1804.

[28] Johnson, K., K. Kendall, and A. Roberts. *Surface energy and the contact of elastic solids*. in *Proceedings of the Royal Society of London A: Mathematical, Physical and Engineering Sciences*. 1971. The Royal Society.

[29] Bartlett, M.D. and A.J. Crosby, *Scaling normal adhesion force capacity with a generalized parameter.* Langmuir, 2013. **29**(35): p. 11022-11027.

[30] Ponce, S., J. Bico, and B. Roman, *Effect of friction on the peeling test at zero-degrees.* Soft matter, 2015. **11**(48): p. 9281-9290.

[31] Mojdehi, A.R., D.P. Holmes, and D.A. Dillard, *Friction of Extensible Strips: an Extended Shear Lag Model with Experimental Evaluation.* International Journal of Solids and Structures, 2017.

[32] Shull, K.R., et al., *Axisymmetric adhesion tests of soft materials.* Macromolecular Chemistry and Physics, 1998. **199**(4): p. 489-511.

[33] Creton, C. and H. Lakrout, *Micromechanics of flat-probe adhesion tests of soft viscoelastic polymer films.* Journal of Polymer Science Part B: Polymer Physics, 2000. **38**(7): p. 965-979.

[34] Chaudhury, M.K., *Rate-dependent fracture at adhesive interface.* The Journal of Physical Chemistry B, 1999. **103**(31): p. 6562-6566.

[35] Broek, D., *Elementary engineering fracture mechanics*. 2012: Springer Science & Business Media.

[36] Rybicki, E.F. and M.F. Kanninen, *A finite element calculation of stress intensity factors by a modified crack closure integral.* Engineering Fracture Mechanics, 1977. **9**(4): p. 931-938.

[37] Yang, H., et al., *Multi-layer in-situ for evaluation of dynamic mechanical properties of pressure sensitive adhesives.* International journal of adhesion and adhesives, 2007. **27**(7): p. 536-546.

[38] Jones, E., et al., *In situ measurements of strains in composite battery electrodes during electrochemical cycling.* Experimental Mechanics, 2014. **54**(6): p. 971-985.

6 Conclusions

In this dissertation, four different studies related to the interaction between granular media and elastic beams, friction of elastomeric materials and extensible strips, and scaling law for adhesion are performed. In the following, summary of conclusions and potential future directions for each chapter are presented:

Chapter II: Buckling of elastic beams embedded in granular media

The buckling response of elastic slender beams embedded in granular media is investigated using both experiment and theory. The buckling load was obtained as a function of penetration ratios for beams with different bending rigidities, lengths, and boundary conditions, and in granular media with different grain sizes. The Ritz energy approach is implemented to predict the buckling load based on the concept of a beam on an elastic foundation with linearly increasing stiffness with respect to the depth, measured from horizontal force-displacement response of the medium. The Clamped-Pinned (C-P) boundary condition (BC) was found to be more significantly affected by the surrounding granular media compared to the Clamped-Clamped (C-C) boundary condition, which is thought to emerge from different mode shapes and deformation profiles along the length of the beam the two BCs. Moreover, buckling loads of C–P and C–C BCs converge at a characteristic penetration ratio (the ratio of the grains' height over beam's length), where the stiffness of granular support is considerably higher than the rigidity of the beam, resulting in confinement of the lower portion of the beam that prevents the beam from sensing its embedded end boundary condition. We find a scaling law relationship between the characteristic penetration ratio and the nondimensional stiffness parameter, allowing characterization of three distinct regions where the interaction of the beam and surrounding medium is different depending on the ratio of the granular support effective stiffness over beam's effective stiffness. The buckling loads for the beams with different geometries, penetration ratios, and BCs collapse onto a single curve, when the proposed nondimensional buckling load and penetration ratio are used. The reduced buckling load parameter is proposed to describe the structure's stability when partially embedded in a medium with a variable stiffness, whereas the characteristic penetration ratio dictates different beam-grain interaction regimes, ultimately influencing the effect of the boundary condition at the embedded end of the beam.

Key contributions in this chapter include:

- A theoretical model, based on the concept of a beam on an elastic foundation with linearly increasing stiffness with respect to the depth, is developed and experimentally validated for buckling of elastic beams embedded in granular media.
- Several nondimensional parameters are developed, resulting in collapsing the buckling load data for different penetration ratios and beam geometries.
- A scaling law is proposed for characteristic penetration ratios and nondimensional stiffness parameters associated to the effective stiffness of the granular media and beams.
- Different interaction regions depending on the ratio of the granular support effective stiffness over beam's effective stiffness are demonstrated.
- The effect of boundary conditions and a characteristic penetration ratio on the embedded end of the beams are illustrated.

Although the purpose of this study was to fundamentally investigate the effect of surrounding media on elastic beams, the same approach may be used for different media such as elastomeric medium, wet granular media, hydrogel medium, etc. that are potential more similar to the real applications. In addition, studying the effects of grain's size and shapes, and also container size, where the interaction between the medium and the sides of the container play an important role, may help to better understand the response of different media. Furthermore, nonlinear buckling analysis taking into account for large deformation of the *elastica* would be interesting as potential future works.

Chapter III: Friction of extensible strips: An extended shear lag model with experimental evaluation

The changes in static and kinetic friction of extensible strips with respect to effective axial compliance are investigated. A steel sled was pulled across a glass substrate, while the strip was only bonded to the leading edge of the sled, allowing for two frictional interfaces: 1) between the sled and strip, and 2) between the strip and substrate. We found that by increasing the effective axial compliance, the static friction force peak decreased dramatically, whereas the kinetic friction force increased significantly. For sufficiently compliant strips, there was no observable static peak, while the increase in kinetic friction force was maintained even after slippage of the entire strips. The local displacements of several points along the length of the strip were analyzed using image processing and development of local slippage zone was observed, revealing three regions along

the length of the strip, namely no-slip, transition, and slip zones. Furthermore, a new extension of the classical shear lag model is proposed to predict the effect of axial compliance on the friction force of extensible strips. The three regions are defined along the length of the strip based on the transition displacement (from static to kinetic friction) of a control case corresponding to an axially rigid strip. Good agreement was found between the extended shear lag model and the experiments. A possible mechanism for the permanent increase in the kinetic friction is discussed to be the stick-slip behavior on the bottom interface (between the strip and substrate), giving rise to the oscillatory slippage on the top interface (between the sled and strip), thereby resulting in an additional frictional interface playing a role even after slippage of the entire strip occurs. This study could give more insights for design and optimization of systems where static and kinetic friction play an important role. The practical implications of this work potentially span a wide range of applications such as tires, shoes, brake systems, wearable sensors, and stretchable electronics, where the system compliance and therefore static and kinetic friction forces can be tuned depending on the applications and significance of each friction force.

Key contributions in this chapter include:

- The effect of axial compliance on the static and kinetic friction response of extensible strips is experimentally investigated, showing significant changes in frictional response of extensible strips with different axial compliances.
- A theoretical model, based on extension of the shear lag model, to predict the effect of axial compliance on the frictional response of extensible strips is developed.
- A simple image analysis is implemented to capture the localized motion along the length of the strips.
- Static friction was observed to decrease by increasing the axial compliance whereas the kinetic friction increased by increasing the compliance.
- A permanent increase in the kinetic friction for sufficiently soft extensible strips was observed and possible mechanisms for the permanent increase are explored.

Although we tried to study the mechanisms of the changes in the static and kinetic friction forces with the compliance, this effect is still not well understood. For example, the reason for the permanent increase in the kinetic friction with increasing the compliance is not completely justified, so further experiments are needed to support the hypothesis. One could perform the

friction test using the extensible strip and a pulley as the substrate, in order to remove the secondary interface on the top of strip and reduce the complications associated to it. The strip can be partially wrapped around the pulley with a weight hanging on one side, to perform the friction test without the top sled that was necessary to apply normal force in the flat substrate. If no increase in the kinetic friction is observed in this case, the hypothesis that the additional interface on the top leads to the increase in the kinetic friction can be proved. Furthermore, the same theoretical approach could be implemented to Pressure Sensitive Adhesives (PSA) to predict the force-displacement response where there is plastic yielding in the backing or adhesive layer.

Chapter IV: The effect of normal force on kinetic coefficient of friction of elastomeric materials

The effect of normal force on kinetic coefficient of friction (COF) of two elastomeric materials, namely silicone and acrylic-based elastomers, on a macroscopically smooth substrate is investigated using an instrumented pendulum setup. Although the response of silicone elastomer was consistent with that of adhesion friction in the literature, *i.e.* increase in COF by decreasing the normal force, the acrylic response was in opposite direction, *i.e.* a decrease in COF by decreasing the normal force. In order to further explore the origin of acrylic response anomalies, friction tests were performed at lower velocity, and also with graphite powder present on the interface. We found that the acrylic response anomaly at very low normal forces likely originated from a rate-dependent response of surface properties, giving rise to a hysteretic friction contribution even on a macroscopically smooth substrate. To further support the hypothesis, drop tests were performed to measure the surface hysteresis of the elastomers. The surface hysteresis of the acrylic was found to be more dominant for smaller spherical balls, *i.e.* lower normal forces, compared to the bigger ones, i.e. higher normal forces, which was consistent with the friction test results. This study could lead to greater understanding of dynamic frictional response of elastomeric materials, taking into account the role of normal force, dynamic mechanical analysis data, and surface properties in design and optimization of materials with applications where the friction is important.

Here is the list of key contributions in this chapter:

- Two different elastomers, i.e. silicone and acrylic-based elastomers, with different frictional perceptions in the lab (using the traditional sled test method) and field conditions are examined and the underlying causes for the differences are explored.

- A custom-built instrumented pendulum test setup is developed to measure the kinetic COF at high speed, close to the field conditions.
- A decrease in the COF of acrylic elastomer at high speeds is observed by decreasing the normal force for the acrylic whereas the COF of silicone increased by decreasing the normal force.
- The response of acrylic at high speeds and low normal forces found to be unusual compared to the adhesion friction response of elastomeric materials reported in the literature.
- A drop test was performed to characterize the surface hysteresis of the elastomers and a correlation was observed between results obtained from the drop tests and COF of acrylic at high speed and low normal forces, resulting in a better understanding of the origin of acrylic friction response.

This study opened several avenues about how different properties could affect the frictional response of elastomeric materials. For example, one could perform systematic experiments by tuning the acrylic storage modulus, e.g. by changing the cure time or UV exposure, to see the effect of storage modulus on the frictional response. This would help to justify the hypothesis that the low storage modulus of the acrylic gives rise to conforming on the surface micro-asperities and therefore hysteresis friction on a macroscopically smooth surface. Furthermore, tuning the glass transition temperature (α-transition), and if possible, β and γ-transitions of the acrylic may be helpful to understand the role of segmental or local molecular motions on the adhesion and cohesion hysteresis and hysteresis contribution to the friction.

Chapter V: Revisiting the generalized scaling law for adhesion: role of compliance and extension to progressive failure

In this chapter, we revisited the generalized scaling law developed for adhesion based on the square root of ratio of bond area to compliance ($\sqrt{A/C}$), using the classical fracture mechanics approach. The proposed scaling law depends on the rate of change of bond area with compliance, rather than the ratio of area to compliance. The shear lag model is used to derive a closed-form relationship for the system compliance and also experimentally confirmed using Digital image correlation (DIC) technique. The conditions where two models deviate from each other are discussed, namely with changes in load train compliance and mode of failure from catastrophic to progressive failure.

In particular, we found three regions by comparing the $\sqrt{A/C}$ and $\sqrt{\partial A/\partial C}$ scaling parameters obtained from closed-form relationship based on the shear lag model. First, small values of scaling parameters, corresponding to the rigid backed adhesives with uniform shear stress distribution along the length and catastrophic failure, where the two scaling parameters are identical. Second, intermediate values of scaling parameters, corresponding to the non-uniform shear stress distribution along the length and catastrophic failure, where the two models slightly deviate from each other. Third, large values of scaling parameters, associated to the non-uniform shear stress distribution along the length and progressive failure, resulting in significant deviation between the two models. Based on the classical fracture mechanics approach, load train compliance should not affect the force capacity of adhesive systems, as the stored elastic energy in the load train cannot continue to drive failure once the specimen breaks. Although the load train compliance is found to affect the force capacity of the PSA used in this study, we believe the apparent load train compliance effect enters indirectly through the viscoelastic nature of the materials tested. A power-law model is used to take into account the rate dependent response of the critical strain energy release rate of the interface, resulting in collapse of all the data for different load train compliances and failure modes onto a single linear curve. Furthermore, we found the transition in failure mode from catastrophic to progressive failure occurs at a characteristic length scale equal to twice the shear lag length scale. The revisited scaling relationship proposed in this study could give greater insights to the role of system compliance and failure modes on the performance of adhesive systems.

Here is the list of key contributions in this chapter:

- A generalized scaling law for bond strength of adhesive joints, based on classic fracture mechanics approach, that depends on the rate of change of debond area with compliance rather than the ratio of bond area to compliance reported in the literature, is developed.
- A power law model is implemented for the strain energy release rate, to take into account rate-dependent material response at the interface.
- A closed-form solution of the bond compliance is derived based on the concept of shear lag model.
- The effect of load train compliance on the bond strength of adhesive joints is evaluated. Based on the classical fracture mechanics approach for rate-independent materials, the load

train compliance should not affect the force capacity of the adhesive system, whereas when the area to compliance ratio is used as the scaling parameter, it directly influences the bond strength, making it necessary to distinguish compliance contributions.

- Digital image correlation (DIC) technique is implemented to measure the displacement fields along the length of adhesive and the obtained shear stress is compared with that calculated from the shear lag model.
- The conditions where the proposed scaling law deviates from the reported scaling law is elaborated and demonstrated, showing significant deviation between the two models when the bond length increases to greater than twice the characteristic shear lag length scale.

Since we used PSA tapes to demonstrate the validity of our proposed scaling law, one could also examine adhesion of elastomeric strips to a substrate using the proposed scaling relationship to evaluate the applicability of the model to different type of materials. Furthermore, the extension of shear lag model developed in Chapter III could be used to the adhesive systems with plastic yielding or elastomers with frictional dissipation to further expand the applicability of the proposed scaling law. It would also be interesting to apply both scaling relationships to normal adhesion tests (*e.g.* JKR adhesion test), to investigate the role of load train compliance on the pull-off adhesion force, as the pull-off adhesion force differs for about factor of two between the load control and displacement control experiments, even though the linear elastic fracture mechanics is used. Investigating the effect of nonlinear force-displacement response, for the case of JKR adhesion, compared to the linear force-displacement response, for the case shear loading, would be of great importance as future works.